

Ranier Menote Lemes Silva

Angular Scale of Baryonic Acoustic Oscillations from
SDSS Data

Brasil

Agosto, 2021

Ranier Menote Lemes Silva

Angular Scale of Baryonic Acoustic Oscillations from SDSS Data

Dissertação apresentada ao Programa de Pós-Graduação em Física da Universidade Federal do Espírito Santo, como requisito para obtenção do grau de mestre em Física.

Universidade Federal do Espírito Santo – UFES

Centro de Ciências Exatas – CCE

Programa de Pós-Graduação em Física – PPGFis

Supervisor: Valerio Marra

Brasil

Agosto, 2021

Ficha catalográfica disponibilizada pelo Sistema Integrado de Bibliotecas - SIBI/UFES e elaborada pelo autor

S586a Silva, Ranier Menote Lemes, 1997-
Angular scale of baryonic acoustic oscillations from SDSS data / Ranier Menote Lemes Silva. - 2021.
111 f. : il.

Orientador: Valerio Marra.
Dissertação (Mestrado em Física) - Universidade Federal do Espírito Santo, Centro de Ciências Exatas.

1. Oscilação Acústica Bariônica. 2. Cosmologia. 3. SDSS. 4. BOSS. 5. eBOSS. I. Marra, Valerio. II. Universidade Federal do Espírito Santo. Centro de Ciências Exatas. III. Título.

CDU: 53



UNIVERSIDADE FEDERAL DO ESPÍRITO SANTO

CENTRO DE CIÊNCIAS EXATAS

PROGRAMA DE PÓS-GRADUAÇÃO EM FÍSICA

ATA DA SESSÃO PÚBLICA DE DEFESA DE DISSERTAÇÃO DO MESTRADO DO ALUNO RANIER MENOTE LEMES SILVA.

Às 14h00 do dia 26 do mês de agosto do ano de 2021, estavam reunidos por videoconferência, <https://us02web.zoom.us/j/83055420538?pwd=SDAxRmtmWFIVSDEzY1NwMEszZExZUT09> a Banca Examinadora, composta pelos Professores Dr. Valerio Marra (Orientador/PPGFis), Dr. Armando Bartolome Bernui Leo (Observatório Nacional), Dr. Oliver Fabio Piattella (PPGFis/UFES) e Dr. Davi Cabral Rodrigues (PPGFis/UFES), para a sessão, com acesso público externo também por videoconferência, da ducentésima vigésima defesa de dissertação de mestrado do aluno Ranier Menote Lemes Silva, com o tema: “Angular Scale of Baryonic Acoustic Oscillations from SDSS Data”. Presentes os membros da banca e o examinando, o presidente deu início à sessão, passando à palavra ao aluno. Após exposição de 50 minutos por parte do examinando, o senhor presidente retomou a palavra e a cedeu aos Membros da banca, um a um, para procederem à arguição, as quais foram respondidas pelo aluno. Em seguida, o senhor presidente afastou da videoconferência todos os demais presentes para que a banca pudesse deliberar. Ao final das deliberações o presidente da sessão convocou o mestrando e os interessados acessando-os via online; com a palavra, o presidente da banca leu a decisão que resultou a APROVAÇÃO do examinando; por fim, o presidente da sessão alertou que o aprovado somente terá direito ao título de mestre após a entrega da versão final de sua dissertação, em papel e meio digital, à Secretaria do Programa e da homologação do resultado da defesa pelo Colegiado Acadêmico do PPGFis. O Senhor Presidente, então, deu por encerrada a sessão, e eu, José Carlos Coutinho da Cruz, Secretário do Programa de Pós-Graduação em Física, lavrei a presente ata, que é assinada pelos membros da Comissão Examinadora. Vitória-ES, 26 de agosto de 2021.

Prof. Dr. Armando Bartolome Bernui Leo
(Observatório Nacional)

Prof. Dr. Valerio Marra
(Orientador- PPGFis/UFES)

Prof. Dr. Oliver Fabio Piattella
(PPGFis/UFES)

Prof. Dr. Davi Cabral Rodrigues
(PPGFis/UFES)



UNIVERSIDADE FEDERAL DO ESPÍRITO SANTO

PROTOCOLO DE ASSINATURA



O documento acima foi assinado digitalmente com senha eletrônica através do Protocolo Web, conforme Portaria UFES nº 1.269 de 30/08/2018, por
VALERIO MARRA - SIAPE 2179379
Departamento de Física - DF/CCE
Em 26/08/2021 às 16:17

Para verificar as assinaturas e visualizar o documento original acesse o link:
<https://api.lepisma.ufes.br/arquivos-assinados/256939?tipoArquivo=O>



UNIVERSIDADE FEDERAL DO ESPÍRITO SANTO

PROTOCOLO DE ASSINATURA



O documento acima foi assinado digitalmente com senha eletrônica através do Protocolo Web, conforme Portaria UFES nº 1.269 de 30/08/2018, por
OLIVER FABIO PIATTELLA - SIAPE 2847692
Departamento de Física - DF/CCE
Em 26/08/2021 às 16:25

Para verificar as assinaturas e visualizar o documento original acesse o link:
<https://api.lepisma.ufes.br/arquivos-assinados/256970?tipoArquivo=O>



UNIVERSIDADE FEDERAL DO ESPÍRITO SANTO

PROTOCOLO DE ASSINATURA



O documento acima foi assinado digitalmente com senha eletrônica através do Protocolo Web, conforme Portaria UFES nº 1.269 de 30/08/2018, por
DAVI CABRAL RODRIGUES - SIAPE 1816732
Departamento de Física - DF/CCE
Em 26/08/2021 às 17:14

Para verificar as assinaturas e visualizar o documento original acesse o link:
<https://api.lepisma.ufes.br/arquivos-assinados/257039?tipoArquivo=O>

AGRADECIMENTOS

Primeiramente, gostaria de agradecer ao meus pais pelo todo apoio que sempre me deram desde de minha infância quando já manifestava meus interesses por ciência.

Deixo meus agradecimentos ao Dr. Valerio Marra que me orientou durante o mestrado, me proporcionando bastante experiência e sabedoria na prática de uma pesquisa científica.

Também fico especialmente grato a todo o companherismo e apoio emocional que a Tábata Luiza me ofereceu durante toda essa jornada.

Aos meus amigos consagrados de longa data Felipe, Vitor, João, Pedro, Vava, Caio, Lettieri, Igor, Paulo, Lud, Lorena, Mari, Vitor Machado e Miguel que me fizeram companhia online durante toda essa pandemia, além de boas discursões de física e computação. Também gostaria de agradecer a alguns colegas que me ajudaram em algumas situações a respeito deste trabalho como David Camarena, Renan Oliveira e Tassia Ferreira.

Fico grato aos professores Dr. Oliver Piattella, Dr. Davi Rodrigues, Martin Makler e Júlio Fabris que contribuíram para o enriquecimento da minha formação durante a pós graduação e aos Drs. Mariana Penna e Sandro Vitenti por me incentivarem desde o início a seguir essa área de cosmologia observacional que eu descobrir ser muito interessante.

Também deixo aqui o reconhecimento ao CNPq pelo financiamento dessa pesquisa.

ABSTRACT

Most data analyses assume a cosmological model and, although these methods work well, it is important to verify their consistencies in a model-independent way. This discussion between model dependent and independent analyses has been intensified over the last years, with the increasing tension between the parameters deduced from early and late universe observable. The strongest tension in cosmology today regards the determination of the Hubble constant, the present-day expansion rate of the universe [1, 2, 3]. Determinations from the cosmic microwave background and Cepheids-calibrated supernovae Ia show a disagreement at about 4 sigma level. It is then important to measure the cosmic expansion through alternative techniques such as galaxy clustering. As predicted by the Λ CDM model, it must exist a preferable scale imprinted in the distribution of galaxies (called *Sound Horizon*). These *Baryonic Acoustic Oscillations* (BAO) can be measured by the spatial correlation function, but that assumes a cosmological model to calculate the distances between the galaxies. An alternative is to measure the angular correlation function without assuming a cosmological model, as pioneered by [4, 5, 6] which analyzed the data from Sloan Digital Sky Survey (SDSS) collaboration. The results from the angular correlation function analysis showed tension with respect to the one from the spatial correlation function.

Here, we analyze the final data releases from the BOSS and eBOSS surveys in order to investigate this tension. While we use an approach similar to [6], we improve on the methodology and develop a new analysis pipeline so as to provide an independent analysis. We confirm, in part, the tension between the angular and spatial correlation function analyses. Finally, we use the measurements of the BAO scale in order to constrain the standard model parameters.

Keywords: BAO, Cosmology, SDSS, BOSS, eBOSS.

RESUMO

A maioria das análises de dados assume um modelo cosmológico e, embora esses métodos funcionem bem, é importante verificar suas consistências de forma independente da cosmologia. Essa discussão entre análises dependentes e independentes de modelos tem se intensificado nos últimos anos, com a crescente tensão entre os parâmetros deduzidos do universo observável inicial e tardio. A tensão mais forte na cosmologia hoje diz respeito à determinação da constante de Hubble, a taxa de expansão atual do universo [1, 2, 3]. Os resultados a partir da radiação cósmica de micro-ondas e das supernovas Ia, calibradas pelas Cefeidas, mostram uma discordância da ordem de 4 sigma. Então, é importante medir a expansão cósmica por meio de técnicas alternativas, como o agrupamento de galáxias. Conforme previsto pelo modelo Λ CDM, deve existir uma escala preferencial impressa na distribuição das galáxias (chamada *Sound Horizon*). Essas *Oscilações Acústicas Bariônicas* (BAO) podem ser medidas pela função de correlação espacial, porém isso assume um modelo cosmológico para calcular as distâncias entre as galáxias. Uma alternativa é medir a função de correlação angular sem assumir um modelo cosmológico, como feito por [4, 5, 6] que analisou os dados da colaboração do Sloan Digital Sky Survey (SDSS). Os resultados da análise da função de correlação angular mostraram tensão em relação à da função de correlação espacial.

Aqui, analisamos os dados finais das observações do BOSS e eBOSS para investigar essa tensão. Embora usemos uma abordagem semelhante a [6], melhoramos a metodologia e desenvolvemos um novo pipeline de análise para fornecer uma análise independente. Confirmamos, em parte, a tensão entre as análises das funções de correlação angular e espacial. Finalmente, usamos as medidas da escala BAO para restringir os parâmetros do modelo padrão.

Palavras-chave: BAO, SDSS, BOSS, eBOSS

LIST OF FIGURES

Figure 1 – On the top, there is a Hubble diagram of distance versus velocity for secondary distance indicators calibrated by Cepheids. On the bottom, the value of H_0 like a function of distance [7].	22
Figure 2 – It shows the fit of theoretical blackbody spectrum over the data measured by instruments on COBE. Here the points are hidden in the theoretical blackbody curve, all of which have uncertainties smaller than the thickness of the curve [8]	29
Figure 3 – This figure [3] shows the last direct and indirect measurements of H_0 with 68% confidence level. The region with color cyan defines the last value of H_0 given by SH0ES Team (R20) while the red region is the last value given by the Planck 2018 (PL18).	36
Figure 4 – The left image shows the marginalized posterior distribution in the σ_8 and Ω_m . The right image the constraints on the structure growth parameter S_8 for different probe combinations over last years [9].	37
Figure 5 – Evolution of the radial mass profile a long of the comoving radius of an initially single overdensity located at the origin for CDM, baryons (called gas), photons, and neutrinos. the relativistic species were divided by a constant factor to be the same scale as other species [10]	54
Figure 6 – LRG’s redshift distribution of DR12 and DR16 for two regions (North and South) of the sky (the bin used to built this histogram is $\delta z = 0.01$).	59
Figure 7 – Representation of angular separation between galaxies into the shell	60
Figure 8 – Equatorial coordinate system and representation of angular position of two objects over celestial sphere.	61
Figure 9 – Example of estimating ACF with and without w_{FKP}	64
Figure 10 – Here is shown the redshift distribution of a general Mock Catalog. The Mock-random catalog in the figure is 20 times larger than Mock-real. Note that the shape of Mocks catalog is preserved in the simulation.	67
Figure 11 – Representation of shells with different width of redshift	68
Figure 12 – The angular correlation function measured for two shells with the same radius ($z_{eff} = 0.43$) but with different width (δz). Even with more galaxies, it is evident the attenuation of the peak for the thicker shell because of the radial projections.	69
Figure 13 – Simulations of α correction [11]	72

Figure 14 – Some examples of ACF (black dots) plots with their respectively best fit (blue line) found out by a global optimization method. As said before, the error bars shown here comes from diagonal of covariance matrix . The graphics of complete analysis are in the appendix B	74
Figure 15 – The values are constrained over the regions (marginalized posterior distribution) with 68% and 95% confidence levels. It was used the open-source code EMCEE [12] to explore the parametric space (MCMC) and the codes available by GetDist to plot the distributions above [13]. See the appendix B for all analysis.	75
Figure 16 – A typical Covariance (left) and Correlation (right) Matrices deduced from 1000 Mocks Catalogs (This in particular refers to shell $z_{eff} = 0.51$ and $\delta z = 0.01$).	76
Figure 17 – The image shows the estimation of correlation time of parameter $r_d h$ for the best fits with redshift $z = 0.43, 0.55, 0.61, 0.63$. The dashed line defines the limit (when crossed it) from what a reasonable estimate of autocorrelation time is obtained . See the appendix B.	77
Figure 18 – These examples show the typical displacement by what the peak undergoes. The red dots are the θ_{FIT} and the blue dots are the peaks corrected by the factor α (deduced from the fit represented by the black line), that is θ_{BAO} . We see that the peak goes to smaller angle values as increase the width (δz) of the shell. Note also after the correction the peaks tend to form a straight line, around the θ_{BAO} value (as we expect, because the final value can not depend of the width of the shell).	78
Figure 19 – α correction deduced directly from the data	79
Figure 20 – Peaks displacements of the effective redshift $z_{eff} = 0.53, 0.57, 0.63$ measured.	80
Figure 21 – On the left image it is shown the angular scale predicted by the parameters of the best fit Planck 2018 [1] together with the measurements of this work. On the right, we normalize the same graphic with the predicted curve.	81
Figure 22 – Here was added the measurements of angular BAO scale from previous works [4], [14], [5], [6].	81
Figure 23 – The first image (left) shows the distribution proportional to the posterior that we have obtained from MCMC analysis to the parameters $r_d h$ and Ω_m , and their respective expected values. The second image (right) is shown the same distribution together with the distributions from Planck 2018.	82

Figure 24 – Both images above show the distribution in parametric using SH0ES prior on M_b . In the right side the image compare it with the distribution from Planck 2018 results.	84
Figure 25 – This image shows the distribution in parametric using flat prior on \hat{M}_b .	84
Figure 26 – Convergence test for each MCMC analysis, following the algorithm available by EMCEE A	85
Figure 27 – In the left image it is shown the distribution in parametric as a result of analysis in Planck 2018 and this work using just BAO data (grey distribution), BAO plus supernovae data with flat priors (red distribution) and with SH0ES prior (blue distribution). In the right image it is shown the same distributions except that comes from BAO data only (it is like a zoom to see better the small difference between the distribution that comes from flat and SH0ES prior).	85
Figure 28 – This image shows the curve of angular scales given by 4.2 and using the best fit of the above analysis.	86
Figure 29 – Best fits from global optimization used as initial point on MCMC. . .	100
Figure 30 – Distribution on parametric space built with MCMC to all best redshift shells.	105
Figure 31 – Plot of autocorrelation time to all best MCMC (shown in the figure 30).	106
Figure 32 – Displacement of apparent angular BAO scale by radial projections. . .	107

LIST OF TABLES

Table 1 – Results for six parameters of Λ CDM model reported by the analysis of data from Planck 2018 (P18) CMB power spectrum [1]. Note, some parameters are measured in terms of $H_0 = 100h$	35
Table 2 – The result of θ_{FIT} for the best width.	78
Table 3 – Table that includes the θ_{BAO} results. Note the uncertainties increase by the factor α as well.	79
Table 4 – Table that summarize the results of analysis.	86

LIST OF ABBREVIATIONS AND ACRONYMS

BAO	Baryonic Acoustic Oscillations
CMB	Cosmic Microwave Background
DE	Dark Energy
DM	Dark Matter
FLRW	Friedmann-Lemaître-Roberson-Walker
PDF	Probability Distribution Function
SNe Ia	Type Ia Supernovae
SR	Special Relativity
GR	General Relativity
ACF	Angular Correlation Function
SCF	Spatial Correlation Function
MCMC	Markov chain Monte Carlo
SDSS	Sloan Digital Sky Survey

CONTENTS

	INTRODUCTION	14
1	THEORETICAL OVERVIEW	15
1.1	Special Relativity	15
1.2	Theory of General Relativity	16
1.2.1	Curved Spacetime	16
1.2.2	Gravitation	19
1.3	Background of Cosmology	20
1.3.1	Cosmological Principles	20
1.3.2	Expansion of the Universe	21
1.3.3	Cosmological Distances	23
1.3.4	Friedmann Equations	26
1.3.5	CMB	29
1.3.6	Horizon Problem	30
1.3.7	Flatness Problem	31
1.4	Inflation	31
1.4.1	Inflaton	33
1.4.2	Origin of Perturbations	34
1.5	Λ CDM	34
1.5.1	Model Parameters	34
1.5.2	Hubble's Tension	35
1.5.3	Growth of Structures Tension	36
2	PERTURBATIONS ON COSMOLOGY	38
2.1	Gauge Freedom	38
2.1.1	Decomposition of Perturbations	38
2.1.2	Gauges Examples	40
2.2	Perturbations in Einstein's Field Equations	42
2.2.1	Scalar Perturbations in Field Equations	43
2.3	Boltzmann Equations	44
2.3.1	Radiation	45
2.3.2	Photons	46
2.3.3	Neutrinos	47
2.3.4	Baryons	48
2.3.5	Cold Dark Matter	49
2.4	Baryonic Acoustic Oscillations	49

2.4.1	Temperature Fluctuations	50
2.4.2	Baryons Tight Coupling	51
2.4.3	Baryons After Decoupling	52
2.5	Stochastic Aspects on Cosmology	55
2.5.1	Power Spectrum and Spatial Correlation	55
2.5.2	Probabilistic Intuition of Spatial Correlation Function	57
3	DATA ANALYSIS	58
3.1	Data Description	58
3.2	Angular Correlation Function	59
3.2.1	Estimator for Angular Correlation Function	61
3.3	Counting Pairs of Galaxies	63
3.3.1	Weights	63
3.3.2	DD, RR and DR	64
3.4	Mocks and Covariance Estimation	66
3.5	The BAO Signal	67
3.5.1	Radial Projection and Angular Bins	68
3.5.2	Detecting the Signal	70
3.5.3	Correction of the θ_{FIT}	70
4	RESULTS	74
4.1	Detecting the θ_{FIT}	74
4.2	Best θ_{BAO}	77
4.3	Constraints on Cosmological Parameters	81
5	CONCLUSIONS	87
	BIBLIOGRAPHY	88
	APPENDIX A – STATISTICAL TOOLS	92
A.1	Fundamental Concepts	92
A.1.1	Random Variables	92
A.2	Bayes’ Theorem	94
A.3	MCMC	95
A.3.1	The Metropolis-Hastings algorithm	96
A.3.2	Convergence Test	97
	APPENDIX B – GRAPHICS	99

INTRODUCTION

The advance of observational astronomy has allowed the verification of predictions made by General Relativity (GR), our modern theory of gravity [15, 16]. As consequence, General Relativity provides the essential ideas about the spacetime that are necessary to explain the wealth of astronomic observations that have been collected over the last ninety years, in particular the accelerated expansion of the universe. General Relativity is the basis of the phenomenological successful Standard Cosmological Model, called Λ CDM [1]. However, during the past few years, this model has shown problems such as the disagreement between early and late universe constraints on the expansion rate of the universe today, the Hubble constant [3]. In cosmology, the growth of structures is studied by considering the evolution of the perturbations on the metric and of the energy-momentum of the components of the universe. One of the predictions is that in the universe after decoupling, ordinary matter started to form structures from a distribution that favored a specific spatial scale, called Sound Horizon (r_s). This scale imprints a characteristic signature, the *Baryonic Acoustic Oscillations* (BAO), over the distribution of galaxies (even today) and it can be observed statistically. This standard ruler can be used to probe the cosmic expansion. This promising observable has been used as another approach to investigate the origin of these tensions and to verify if new physics could solve the disagreement between the early and late universe [6, 5, 4, 11, 17, 18]. This work aims at measuring the BAO scale from the latest data releases from the BOSS and eBOSS galaxy surveys. Our goal is to provide updated constraints on the angular scale of the sound horizon as a function of redshift.

This work is divided into chapters. Chapter 1 introduces the basis of General Relativity, as well as the most successful cosmological model, Λ CDM. In Chapter 2, we will discuss in more depth the theoretical results of Λ CDM, especially about the early universe, when the ordinary matter was coupled with photons. It is shown how the idea of the existence of a preferable scale in the formation of galaxies arises from the theory. In Chapter 3 we present our methodology, introducing the method to estimate the angular correlation of galaxies from catalogs without assuming a cosmological model, besides the bias that this method could have and how to deal with it. Chapter 4 presents our preliminary results of data analysis, and in the final Chapter 5 we give our conclusions, summarizing the main results, their implications and plans for future work.

1 THEORETICAL OVERVIEW

There are many cosmological models of modified gravity (modification of some assumptions on GR) trying to describe the enormous quantity of data available currently. However, the most successful model is based on GR and it is called the Standard Model of Cosmology. This chapter will review the theory of GR (which is fundamental for modern cosmology), experimental results, and limitations of the Standard Model of cosmology. Before an overview of GR, it is necessary to do a brief introduction about its roots, the Special Relativity.

1.1 Special Relativity

Special Relativity (SR) introduces the idea about space and time be part of the same entity, which is called spacetime, a four-dimensional space which dimensions are one of time and three of space. With this theory, it was found out that space and time are not absolute, as in Newton's theory, but they relate to each other. The spacetime, in special relativity, is called Minkowski space and it has a tool to measure distances between points, the metric tensor. A general distance between two points in this space is written as

$$ds^2 = g_{\mu\nu} dx^\mu dx^\nu \quad (1.1)$$

where dx^μ represents the component μ of a differential vector and repeated indexes means sum. The metric of Minkowski is defined as

$$g_{\mu\nu} = \begin{pmatrix} -1 & 0 & 0 & 0 \\ 0 & 1 & 0 & 0 \\ 0 & 0 & 1 & 0 \\ 0 & 0 & 0 & 1 \end{pmatrix} \quad (1.2)$$

Special relativity works with the principle that all inertial observers are equivalent. This means, that all physics that occurs in one frame need happens in another frame with the same relations of causality. The transformation that links from an inertial frame to another is (it says that one has constant relative velocity βc in the x direction)

$$\Lambda_{\nu}^{\mu} = \begin{pmatrix} \gamma & -\gamma\beta & 0 & 0 \\ -\gamma\beta & \gamma & 0 & 0 \\ 0 & 0 & 1 & 0 \\ 0 & 0 & 0 & 1 \end{pmatrix} \quad (1.3)$$

where $\gamma = \frac{1}{\sqrt{1-\beta^2}}$. This tensor is called Lorentz transformation.

It is important to note that ds^2 is invariant about Lorentz transformations. Any vector in the spacetime (four-vector) can build an invariant by Lorentz transformations, just contracting it with the metric tensor like in (1.1). This establishes a useful way to interchange between the inertial frames. The geometric structure of special relativity is called flat, as it can be observed by looking for metric. The evident extension of the theory is to consider some geometric structure where $g_{\mu\nu}$ is a more general tensor field.

1.2 Theory of General Relativity

As we have said, the laws of physics do not change under inertial frames (no accelerated frames, that is, no inertial force is observed). With this definition, one fact in classical mechanics calls attention, the equality between inertial mass and gravitational charge. Note, as these two properties are equals, then the free fall of different masses is the same, and then a free-falling observer must not detect any inertial forces on their around. The conclusion is that, at least for a region of the spacetime small enough, the laws of mechanics in the free-falling observers work as it is an inertial frame. We can go further and say that this is valued not just for mechanics but for all physics laws. That equivalence between free-falling frames and inertial frames (on which special relativity laws work) makes Einstein ask himself about the nature of gravity. Assuming that this equivalence is true, as a principle, then the status of force does not make sense to gravity anymore, it needs to be another phenomenon that is not a classical force as described by Newton's theory. From this principle, together with the similarities between the equations about motion in a general frame to equations of *Riemann Geometry*, arise the concept that the spacetime can be curved, and this phenomenon is observed as being gravitational effects.

1.2.1 Curved Spacetime

Considering a curved spacetime, then an inertial frame can follow a nonstraight trajectory on it. This modification over the trajectory of test particles is associated with gravity, which influences all them in the same way (equivalence between inertial mass and charge mass). In other words, the curvature of spacetime produces the effect that we observe as gravity.

All General Relativity is based on one important principle, the *Equivalence Principle*. It says that in small enough regions of spacetime, the laws of physics reduce to those of special relativity. [19]. Assuming this principle, then at each point of the spacetime there is a tangent space that is flat. In this tangent space, special relativity works and it is the first approximation in that region of curved spacetime. The gravity is noted when we look for the neighborhood of two points in spacetime, with two different tangent spaces (two different inertial frames in curved spacetime). For example, to describe the trajectory of a particle in curved spacetime it is necessary to know how the tensors in each tangent space, which the trajectory passes through, change. In other words, it is necessary to know how to connect vectors defined in different points in curved spacetime. This role is done by a geometrical object called Connection, in GR it is known as *Christoffel Symbols*, given by

$$\Gamma_{\mu\nu}^{\lambda} = \frac{1}{2}g^{\lambda\sigma} (\partial_{\mu}g_{\nu\sigma} + \partial_{\nu}g_{\sigma\mu} - \partial_{\sigma}g_{\mu\nu}) \quad (1.4)$$

This connection between tangent spaces allows us to define the derivative of vectors over the curved spacetime, called *Covariant Derivative* of a vector V^{ν}

$$\nabla_{\mu}V^{\nu} = \partial_{\mu}V^{\nu} + \Gamma_{\mu\sigma}^{\nu}V^{\sigma} \quad (1.5)$$

The covariant derivative measure the instantaneous change of a tensor in comparison to what the tensor would be if it were transported along the spacetime keeping it constant. This idea of transport tensors keeping their constants is called *Parallel Transport*. Then, if there is a path parametrized by $x^{\mu}(\lambda)$, the change along this path of a tensor, for example, V^{μ} , is

$$\frac{D}{d\lambda}V^{\mu} = \frac{dx^{\nu}}{d\lambda}\nabla_{\nu}V^{\mu} \quad (1.6)$$

By definition, the tensor is Parallel transported if the covariant derivative along this path is null. Then, the path thought what the tensor can run without change satisfies the equation

$$\frac{dV^{\mu}}{d\lambda} + \Gamma_{\sigma\rho}^{\mu}\frac{dx^{\sigma}}{d\lambda}V^{\rho} = 0 \quad (1.7)$$

This definition is important when considering that this tensor transported can be a vector proportional to the tangent vector to the path $x^{\mu}(\lambda)$, that is the vector $\frac{dx^{\mu}}{d\lambda}$. The equation (1.7) gives

$$\frac{d^2 x^\mu}{d\lambda^2} + \Gamma_{\sigma\rho}^\mu \frac{dx^\sigma}{d\lambda} \frac{dx^\rho}{d\lambda} = 0 \quad (1.8)$$

which is known as *Geodesic Equation*. This describes the trajectory of particles in spacetime, in particular if all components of connection is null ($\Gamma_{\sigma\rho}^\mu = 0$) then it set trajectory as $\frac{d^2 x^\mu}{d\lambda^2} = 0$.

In GR the metric is said compatible, which means that its covariant derivative is always null, consequently the metric is always parallel transported. The process of parallel transport allows us to investigate the curvature of the surface. In a flat space, a vector that is parallel transported by a loop path will not change. If this process changes the tensor transported, this means that exists some curvature in the region enclosed by the loop. In a curved spacetime, if a vector (or tensor in general) is parallel transported from point A to B by different paths, then the resulting vector (or tensor) will not be the same. the operator that calculates this displacement in the transported vector by two paths (in an infinitesimal distance) is

$$[\nabla_\mu, \nabla_\nu]V^\rho = \nabla_\mu \nabla_\nu V^\rho - \nabla_\nu \nabla_\mu V^\rho = R_{\sigma\mu\nu}^\rho V^\sigma - T_{\mu\nu}^\lambda \nabla_\lambda V^\rho \quad (1.9)$$

Then, the tensors $R_{\sigma\mu\nu}^\rho$ and $T_{\mu\nu}^\lambda$ are the source of the displacement and hence a source of curvature. The first tensor is called *Riemann Tensor* and the second is the *Torsion Tensor*. In GR the Torsion tensor is null because the Christoffel Symbols are symmetric about the last two indices (compatible metric). Then, the tensor that carries the curvature feature is the Riemann Tensor, which is related to the second derivative of the metric

$$R_{\sigma\mu\nu}^\rho = \partial_\mu \Gamma_{\nu\sigma}^\rho - \partial_\nu \Gamma_{\mu\sigma}^\rho + \Gamma_{\mu\lambda}^\rho \Gamma_{\nu\sigma}^\lambda - \Gamma_{\nu\lambda}^\rho \Gamma_{\mu\sigma}^\lambda \quad (1.10)$$

It is also useful to define the *Ricci Tensor* as the contraction of Riemann Tensor

$$R_{\mu\nu} = R_{\mu\lambda\nu}^\lambda \quad (1.11)$$

and a scalar built from it

$$R = R^\mu{}_\mu \quad (1.12)$$

called as *Ricci scalar*.

Another important feature of GR is about *General Covariance* of equations [19]. The geometry of the GR is building over the concept of manifolds (hyperspaces over what we define tensor fields) to describe the spacetime where tensors live in. This description naturally leads to writing tensor equations that are covariant about some kind of transformations (means that the equations remain their form in any coordinate system). This property of theory says that it is invariant about diffeomorphism (coordinate transformations)

1.2.2 Gravitation

One of the most fundamentals ways to build a mechanic theory is using Lagrangian formalism. The Lagrangian is a scalar function that can depend on generalized coordinates and their derivatives. In General Relativity, the metric field carries information about geometry, which rules the dynamics of the system. From classical theory fields, we inserts the dependency of metric on the Lagrangian. it's necessary to explore the possibles scalars that can be built by the contractions of metric and its derivatives. One important property of metric tensors is useful now. It allows us to rewrite any product of metric tensor and its derivatives until second order in terms of Riemann tensor [19]. This means that any tried of form scalars from the metric will yields in the Ricci scalar (contraction of Riemann tensor). The most simple action to the GR, following these principles know as *Einstein-Hilbert Action*

$$S_H = \int \sqrt{-g} R d^4x \quad (1.13)$$

Where g is the determinant of metric, correcting the volume element in curved spacetime. Including the second term in the total action, says S_M , represents the action of the energy and matter (what is the source and influenced by curvature) present in the spacetime. Then, the total action looks like

$$S = \frac{1}{16\pi G} S_H + S_M[g_{\mu\nu}, \psi] \quad (1.14)$$

Following the principle of least action (note that matter action depends on metric and a generic matter field ψ).

$$\frac{1}{\sqrt{-g}} \frac{\delta S}{\delta g^{\mu\nu}} = \frac{1}{16\pi G} \left(R_{\mu\nu} - \frac{1}{2} R g_{\mu\nu} \right) + \frac{1}{\sqrt{-g}} \frac{\delta S_M}{\delta g^{\mu\nu}} = 0 \quad (1.15)$$

rewrite the last term as $-\frac{1}{2} T_{\mu\nu}$, and defining this as *Energy-Momentum Tensor* of matter, then the fundamental tensor equation of GR is

$$R_{\mu\nu} - \frac{1}{2}Rg_{\mu\nu} = 8\pi GT_{\mu\nu} \quad (1.16)$$

This is called *Einstein's Field Equations*. Each component of the tensorial equation relates the geometry (metric and its derivatives) with the matter (source of energy and momentum). The fact the matter can create curvature and be influenced by it is captured by the nonlinear feature of this system of differential equations (there are products of metric and its derivatives, further this is coupled with energy-momentum tensor).

1.3 Background of Cosmology

To study the whole universe as a unique system, it is necessary to assume some theory of gravitation. In this section, we will discuss some observations that are used as bases for creating the cosmological models that try to describe the universe (here we will assume the General Relativity as gravitation theory, that is, it is not considered modifications of Einstein's Field Equations)

1.3.1 Cosmological Principles

One assumption of the standard model is called *Cosmological Principle*. it says that, in large enough scales, the universe is isotropic and homogeneous [20] [21]. this means that the features of the universe, variables, and parameters that describe its evolution, appear the same looking from anywhere of the universe (which is an extension of the Copernicus principle [22]).

Isotropy means that the features of the universe are the same looking for any direction, a example of this is the Cosmic Microwave Background (CMB), which has the temperature measured approximately the same in any direction, at small scales. Homogeneity comes from the idea that our spot on the spacetime is not in a privileged place in the universe, for instance, the measure of energy density here must be the same in another place (it is important to highlight that to assume isotropy in any point then the homogeneity already is satisfied). It is important to note that it assumes some scale large enough where this is true, in small scales this is not true (just think about our solar system or our own galaxy). When it is said "same features of the universe", it is not exactly the same, but realizations from the same statistics behave. This means that observations in different locations will not necessarily equal, just a particular outcome from the same statistics. That idea is very important to understand and interpret data, which can be collected from several places in the universe, and make statistics with these realizations (assuming each of them an independent sample).

1.3.2 Expansion of the Universe

Until the beginning of the development of General Relativity, most popular cosmological models described a static universe. A static universe do not deal with divergences as a contracting universe could arise (energy density increase as universe contract). The universe would be in equilibrium inserting a constant in the Einstein's Equations to create a repulsive interaction against the attraction of matter in the universe (without this the gravitation just will cause a collapse at all, since the solution would be non static). That constant, defined by Einstein, was called *Cosmological Constant*, and the Lagrangian is modified like

$$S = S_M[g_{\mu\nu}, \psi] + \frac{1}{16\pi G} \int d^4x \sqrt{-g} (R - 2\Lambda) \quad (1.17)$$

This Action establishes the following Field Equations

$$R_{\mu\nu} - \frac{1}{2}Rg_{\mu\nu} + \Lambda g_{\mu\nu} = 8\pi GT_{\mu\nu} \quad (1.18)$$

with Λ being a constant. However, the universe is not static, and the first evidence comes from Hubble's observations in 1929 [23], when the majority of extra-galactic nebulae (as he called galaxies around the Milky Way) going away from us was observed. Assuming the cosmological principles, this behavior must be the same looking from all observers in the universe (large scales), this might mean, the universe is expanding. This analysis introduces Hubble's parameter (locally there are a linear relation between the velocity and distance of galaxies, see Fig. 1) which is one of the parameters that rule the expansion of the universe and has been the aim of much current research [1][2]. Despite the Λ have been introduced in the equations to explain the static universe, its repulsive property can create a universe in expansion as observed. This new term in the equations can be seen as part of the left side equation (geometry aspect of the universe) or the right side of the equation (energy density). For example, this constant can be interpreted by the Quantum Field Theory as the energy density of quantum vacuum (which is not really empty), once the energy density from the vacuum is proportional to the metric, at FLRW spacetime. However, the theoretical predictions and the measurement is in a large mismatch [24].

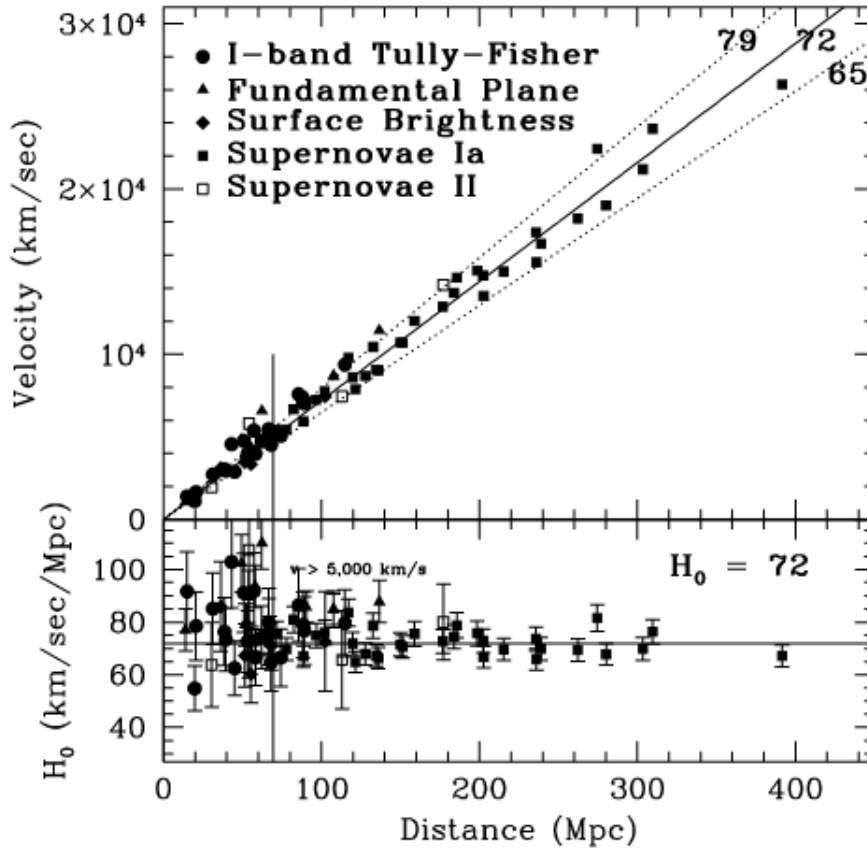


Figure 1 – On the top, there is a Hubble diagram of distance versus velocity for secondary distance indicators calibrated by Cepheids. On the bottom, the value of H_0 like a function of distance [7].

To define the background metric it is necessary to obtain all field equations. This spacetime needs to satisfy the conditions of the cosmological principle and expanding universe. Because of this, we can divide the spacetime into $S = T \times \Sigma$, where T is a one-dimensional space representing the time and Σ is the expanding 3-dimensional space. Writing the spatial metric as γ_{ij} this means

$$ds^2 = -dt^2 + a^2(t)\gamma_{ij}(u)du^i du^j \quad (1.19)$$

where was used the frame where du^i represents the spatial axes and the metric is free from cross terms between time and space (for example $dtdu^i$). Note that we are using here the notation $c = 1$ for the speed of light at vacuum. A fundamental introduction is the function of time, $a(t)$, in the spatial part, which allows the scale of spatial axes to change with time (a spatial grid change with expansion or contraction of the universe). This frame is called *Comoving Observer*. In this frame, the comoving distances do not

change by expansion or contraction of the universe. For example, galaxies move away from each other due to the expansion of the universe but at the same time, the spatial axes expand as well. As the spatial space has symmetries on translations and rotations (homogeneous and isotropic) this means that it is a *Maximally Symmetric Space* [19], then

$$\begin{aligned} R_{ijkl} &= k(\gamma_{ik}\gamma_{jl} - \gamma_{il}\gamma_{jk}) \\ R_{ij} &= 2k\gamma_{ij} \end{aligned} \quad (1.20)$$

where $k = \frac{R}{n(n-1)}$ (for n equals to spatial dimension). Rewriting the metric in spherical coordinates it becomes

$$ds^2 = -dt^2 + a^2(t) \left(\frac{dr^2}{1 - kr^2} + r^2 (d\theta^2 + \sin^2 \theta d\phi^2) \right) \quad (1.21)$$

In this metric the function dimensionless $a(t)$ is called scale factor and can be assumed different spatial geometries for each value of the constant k , called *Spatial Curvature Constant*. It can be positive, null and negative, which mean a universe spatially closed (Spherical), flat (Euclidean) or open (Hyperbolic), respectively. Finally, this metric is called as Friedmann–Lemaître–Robertson–Walker (FLRW) metric.

1.3.3 Cosmological Distances

Once obtained the metric of the spacetime we can calculate distances. Thinking about a far galaxy that emits light in our direction, we can use that to calculate the distance. As the light has the property $ds^2 = g_{\mu\nu}dx^\mu dx^\nu = 0$, we can say that a radial path satisfy

$$\frac{dt}{a} = \pm \frac{dr}{\sqrt{1 - kr^2}} \quad (1.22)$$

where each signal represents the past or future light cone, as we are considering the light incoming (emitted by a far galaxy) we consider the minus signal. The left side of the equation is a function of time, while the right side is a function of radius r (they are independent variables). This means that expression does not change, so

$$\frac{dt_0}{a(t_0)} = \frac{dt_g}{a(t_g)} \quad (1.23)$$

where we relate the interval of time (and the factor scale) of our frame with the frame centered in the observed galaxy. The interval of time can be the period of the light emitted, which is related to its frequency, energy ($E = h\nu$), and length wave. then

$$\frac{a(t_g)}{a(t_0)} = \frac{\nu_0}{\nu_g} = \frac{\lambda_g}{\lambda_0} = \frac{\lambda_g}{\lambda_g + \Delta\lambda} \quad (1.24)$$

where $\Delta\lambda$ indicates the variation that the length suffers a long of its path because of the dynamics of the universe (in that case because of expansion). Then, defining the redshift as $z = \frac{\Delta\lambda}{\lambda_g}$ we can use it to parametrize the expansion of the universe

$$a(z) = \frac{a_0}{1+z} \quad (1.25)$$

where a_0 indicates the current scale factor and a the scale factor of an instant before. An important definition of distance is called *Comoving Distance*. It is defined as

$$\chi_r = \int_0^r \frac{dr'}{\sqrt{1-kr'^2}} = \int_{t_0}^t \frac{dt'}{a(t')} \quad (1.26)$$

this is the radial distance in comoving coordinates, and not depends of the time. The physical distance (also called *Proper Distance*) is defined by

$$D(t, r) = a(t)\chi_r \quad (1.27)$$

If we calculate the comoving distance since from beginning of the universe (denoted by $t_0 = 0$) we define the *Conformal Time*

$$\eta = \int_0^t \frac{dt'}{a(t')} \quad (1.28)$$

This distance (remember we are using $c = 1$) is particularly important to study the causal relations in the universe, as the $\eta(t)$ is the maximal distance that the photon could run from the beginning of the universe until the time t . Then regions separated by distances larger than η never would have communicated with each other. Because of that, η is also called *Comoving Horizon*. The equation (1.26) has different solutions for different values of K . if we define the function

$$S_k(x) = \begin{cases} \sinh(x), & k < 0 \\ x, & k = 0 \\ \sin(x) & k > 0 \end{cases} \quad (1.29)$$

we can write the radius coordinate as

$$r = \frac{1}{H_0 a_0 \sqrt{|\Omega_k|}} S_k \left(H_0 a_0 \sqrt{|\Omega_k|} \chi \right) = \frac{1}{H_0 a_0 \sqrt{|\Omega_k|}} S_k \left(\sqrt{|\Omega_k|} \int_0^z \frac{dz'}{E(z')} \right) \quad (1.30)$$

where we use the left side of equation (1.22) and define the Hubble parameter $H(t) = \frac{\dot{a}}{a}$, the curvature density parameter $\Omega_{k0} = -k/(H_0 a_0)^2$ (it will be explained later) and the function $E(z) = \frac{H(z)}{H_0}$. Based on these definitions, in the observations it more useful to use definitions related directly to variables that we can measure, like luminosity and angles.

• Luminosity Distance

In flat spacetime, we can say that the luminosity of a known source decays with physical distance squared. This is not necessarily true for a general curved spacetime. In that way, we define an effective distance such that this inverse squared law remains valid, that is

$$F = \frac{L_s}{4\pi D_L^2} \quad (1.31)$$

where F is the flux of energy observed and the L_s is the absolute luminosity of the source. Then, considering the expansion of the universe that changes the energy of the photons can be shown that the effective distance is defined by

$$D_L = \frac{(1+z)}{H_0 a_0 \sqrt{|\Omega_k|}} S_k \left(\sqrt{|\Omega_k|} \int_0^z \frac{dz'}{E(z')} \right) \quad (1.32)$$

• Diameter Angular Distance

The Diameter Angular distance, as the name suggests, is related to the apparent angular opening associated with the physical size of the target. Then, the definition is straightforward

$$D_A = \frac{x}{\delta\theta} \quad (1.33)$$

where x is the physical size of the object observed and $\delta\theta$ is its angular opening. Adjusting the coordinates, the distance can be written as $x = a(t_1) r_1 \delta\theta$. This means that

$$D_A = \frac{(1+z)^{-1}}{H_0 \sqrt{|\Omega_k|}} S_k \left(\sqrt{|\Omega_k|} \int_0^z \frac{dz'}{E(z')} \right) \quad (1.34)$$

Considering the numbers of photons is conserved and they travel through null geodesics, the distances above are related by

$$D_L = (1 + z)^2 D_A \quad (1.35)$$

These definitions of distances depend of the functional form $E(z)$. This can be calculated if assume a model to describe the dynamics of the universe, that is, assume what kinds of material exist in the universe, what are the field equations (some theories propose modifications on the field equations of GR). In the next section, we will see the field equations derived from GR and it will provide a way to calculate these distances.

1.3.4 Friedmann Equations

Once obtained the metric allowed by a homogeneous and isotropic universe we can investigate the field equation if we know the Energy-Momentum tensor of the components that fill the universe. Assuming the cosmological principle, the components of the universe are homogeneous and isotropic and then the energy-momentum tensor is like

$$T_{\mu\nu} = \begin{bmatrix} -\rho g_{00} & 0 \\ 0 & p g_{ij} \end{bmatrix}$$

$$T_{\mu\nu} = (\rho + p)U_\mu U_\nu + p g_{\mu\nu} \quad (1.36)$$

where $U_\mu = (1, 0, 0, 0)$ and $\rho(t)$ the energy density, $p(t)$ the pressure (isotropic). Then, in general, we describe it as a perfect fluid. Note that $\rho = \sum_x \rho_x$ and $p = \sum_x p_x$ such that the x indicates the energy component of the universe (non-relativistic matter, radiation, dark energy). Using the maximally symmetric metric it is possible to calculate Christoffel's symbols and hence the Riemann tensors. Then, the only independent field equations from Einstein's equations (with a cosmological constant) are

$$\begin{aligned} \left(\frac{\dot{a}}{a}\right)^2 &= \frac{8\pi G}{3}\rho - \frac{k}{a^2} + \frac{\Lambda}{3} \\ 3\frac{\ddot{a}}{a} &= -4\pi G(3p + \rho) + \Lambda \end{aligned} \quad (1.37)$$

These equations are known as *Friedmann's Equations*. The second equation can be combined with the first and the system can be rewritten as

$$\begin{aligned} H^2 &= \frac{8\pi G}{3}\rho - \frac{k}{a^2} \\ \dot{\rho} + 3(\rho + p)H(t) &= 0 \end{aligned} \quad (1.38)$$

where $H(t) = \frac{\dot{a}}{a}$ and dot notation indicates derivative in time coordinate. This last equation also could have come from the conservation of energy-momentum tensor ($\nabla_\mu T^{\mu\nu} = 0$). Note that it was defined the energy of density to the dark energy $\rho_\Lambda = \frac{\Lambda}{8\pi G}$, which was included in the total energy density $\rho = \rho_m + \rho_r + \rho_\Lambda$ (matter, radiation and dark energy). Given an equation of state ($p \equiv p(\rho)$) then it is possible to solve the last equation in terms of factor scale. To solve analytically, we suppose the various main scenarios where the universe is full of a unique material component. The most relevant equation of state are those that can be written as $\rho_x = w_x p_x$, where w_x is, in principle, a constant. This type of equation has a solution 1.38 given by

$$\rho_x = \rho_{x0}(a/a_0)^{-3(1+w_x)} \quad (1.39)$$

where a_0 is the scale factor of the present universe.

- **Radiation** ($w_x = 1/3$): From statistical physics, the radiation (photon's gas) owns equation of state given by $p = \frac{1}{3}\rho$ (this means that non-relativistic matter, which also has $w_r = 1/3$, own the same solution). From (1.39), that $\rho_r \propto a^{-4}$. With this and the first one of the Friedmann's Equations (in a flat universe, $k = 0$) the $a(t) \propto t^{1/2}$ and $\ddot{a} \propto t^{-3/2}$ (this means, a universe that expand decelerated).
- **Non-relativistic Matter** ($w_x = 0$): From statistical physics, the non-relativistic matter (dust or dark matter) has a velocity very smaller compared by it rest energy, and so it owns equation of state given by $p = 0$ (this means that non-relativistic matter, which also has $w_m = 0$, own the same solution). From (1.39), $\rho_m \propto a^{-3}$ and the solution for scale factor is $a(t) \propto t^{2/3}$ with $\ddot{a} \propto t^{-4/3}$ (this means, a universe that expand decelerated).
- **Dark Energy** ($w_x = -1$): As mentioned before, the dark energy can be associated with the energy of vacuum (once its contribution to energy-momentum tensor is proportional to the metric) or considered as a fluid with a strange equation of state $p = -\rho$ ($w_\Lambda = -1$). $\rho_\Lambda = \text{constant}$ and the solution for scale factor is $a(t) \propto \exp\{\sqrt{\Lambda/3}t\}$ with $\ddot{a} \propto \exp\{\sqrt{\Lambda/3}t\}$ (universe that expand accelerated, called *De Sitter Universe*).

Although the universe is filled with all these elements at the same time, due to their functional form, we can separate the universe into distinct ages. The radiation age is defined as the time where $\rho_r \gg \rho_x$ for all others sub-index x . This means that in this age, the dynamic was driven by the energy density of radiation, because of a^{-4} dependency what makes it grows up, as the universe decrease ($a \rightarrow 0$), faster than any other energy density of the universe. This first age is called the *radiation-dominated Universe*. In the same

way that radiation grows up faster than others when we go to the past, it also decreases faster as the universe expands (goes to the future). Then, at some time another component of the universe should drive its dynamics. So, the next age is called *matter-dominated Universe* (matter has density is proportional to a^{-3}). A important time of the history of the universe is the instant when this transition occurs, marked by a_{eq} ($\rho_r(a_{eq}) = \rho_m(a_{eq})$). Again, at some moment, the density of the matter and radiation are so small that another component starts to dominate the universe. This age is called by *Dark Energy dominated universe*, which is the present age of the universe (the expansion is accelerated, because of the domination of dark energy).

In experiments, just difference of energies are measured, that is, there are always a energy reference over what the measures are based. Wondering about that, it's common to define the *Critical Energy Density*, which is the total energy such that the universe be flat ($k = 0$). Then, from the first equation of (1.38) we define the critical energy density as $\rho_{cr} = \frac{3H^2}{8\pi G}$ (this parameter is not constant). Now, the energy density can be provided in relation to the critical density at present time, then we define

$$\Omega_x(a) = \frac{\rho_x}{\rho_{cr,0}} \quad (1.40)$$

Note that we can rewrite the curvature term in this form too, defining $\Omega_k = -\frac{k}{(H_0 a)^2}$. With these definitions, the first equation (1.38) gives the important relation

$$\sum_x \Omega_x(a) = \left(\frac{H}{H_0}\right)^2 \quad (1.41)$$

This time including the curvature term in the sum. It was already shown that $\rho_x = \rho_{x0}(a/a_0)^{-3(1+w_x)}$, then, it allows us to rewrite the 1.42 as

$$\Omega_x(a) = \frac{\rho_{x0}}{\rho_{cr,0}}(a/a_0)^{-3(1+w_x)} = \Omega_{x0} \left(\frac{a}{a_0}\right)^{-3(1+w_x)} \quad (1.42)$$

For the curvature term, $\Omega_k = \Omega_{k0}(a/a_0)^{-2}$. finally the relation

$$E(a)^2 = \frac{H^2}{H_0^2} = \Omega_{m0}(a/a_0)^{-3} + \Omega_{r0}(a/a_0)^{-4} + \Omega_{K0}(a/a_0)^{-2} + \Omega_\Lambda \quad (1.43)$$

Note that set a important constraint on normalized energy densities today, that is $\Omega_{m0} + \Omega_{r0} + \Omega_{K0} + \Omega_\Lambda = 1$. If the present normalized energy densities are known (Ω_{x0}), then the above expression can be used in the equations (1.32) and (1.34).

1.3.5 CMB

One of the main discoveries that come from observing the sky is the existence of an isotropic background of radiation distributed by the universe, what is called *Cosmic Microwave Background* (CMB). Not just that, but its spectrum of energy is very close to the ideal black body spectrum [2](#). In other words, there is a relation between the temperature and the energy density of this radiation given by Stephan-Boltzmann law ($\rho_\gamma \propto T_\gamma^4$). As the energy density decays as $\rho_\gamma \propto a^{-4}$ then

$$T_\gamma = T_{\gamma 0} \left(\frac{a_0}{a} \right) \quad (1.44)$$

where $T_{\gamma 0} = 2.728 \pm 0.004$ is the temperature of this radiation in the present instant, measured by the *COsmic Background Explorer* (COBE) satellite [\[8\]](#). With this, is not complicated to measure the $\rho_{\gamma 0}$ using the Bose-Einstein distribution. That isotropy suggests that the early universe was in thermal equilibrium, which established the same average temperature to regions causally disconnected today.

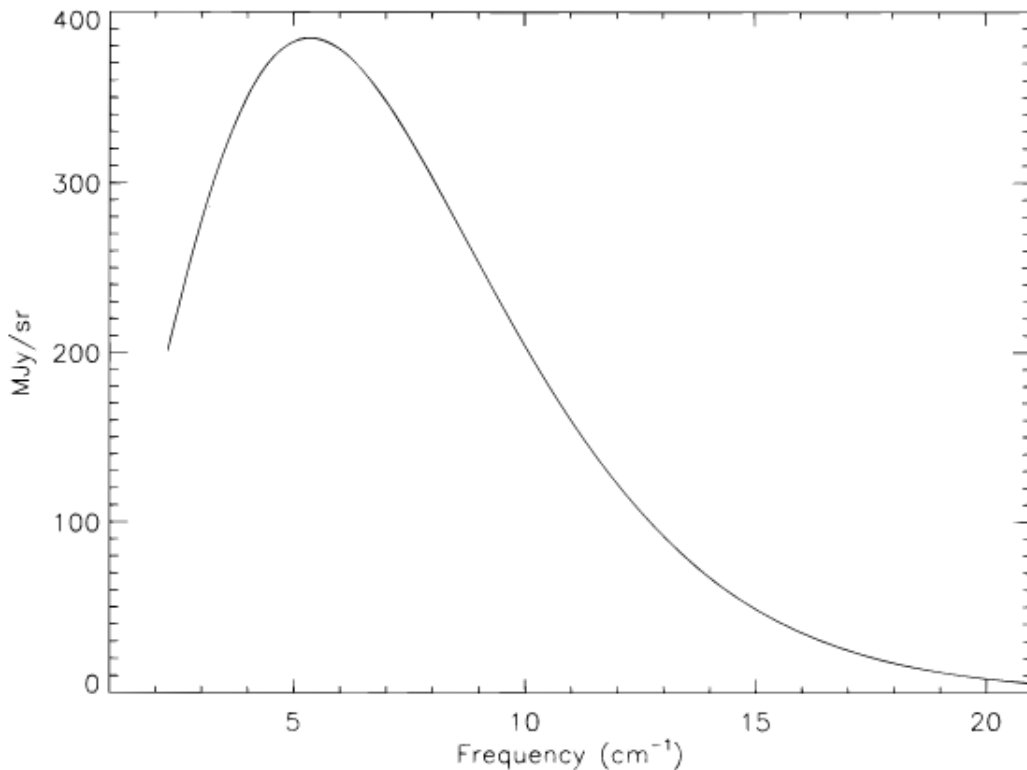


Figure 2 – It shows the fit of theoretical blackbody spectrum over the data measured by instruments on COBE. Here the points are hidden in the theoretical blackbody curve, all of which have uncertainties smaller than the thickness of the curve [\[8\]](#)

1.3.6 Horizon Problem

Consider a universe dominated by radiation and matter, this means that the physical comoving horizon is given by

$$D_\eta(a) = a \int_0^a \frac{da'}{H(a')a'^2} \quad (1.45)$$

Using the expression (1.43) we have

$$D_\eta(a) = \frac{2a}{H_0 a_0 \Omega_{m0}} \left(\sqrt{\Omega_{m0} a + \Omega_{r0}} - \sqrt{\Omega_{r0}} \right) \quad (1.46)$$

The angular diameter distance has a similar expression

$$D_A(a) = \frac{2a}{H_0 a_0 \Omega_{m0}} \left(\sqrt{\Omega_{r0} + \Omega_{m0}} - \sqrt{\Omega_{m0} a + \Omega_{r0}} \right) \quad (1.47)$$

Recall the definition 1.34, we have that two spots in the sky are in casual contact if it is separated with an angle no larger than

$$\theta(a) = \frac{D_\eta}{D_A} \quad (1.48)$$

As we will see, in the early universe the photons interact with ordinary matter (electrons and protons, essentially) so much because its mean free path is smaller than the universe scale size. In other words, in this time the photons could be in thermal equilibrium. At some instant, called *Recombination*, its free mean path is larger than the universe's scales, and then, the photons can travel freely by the universe in expansion. Them, denoting this moment of the last scattering by the redshift $z_l \approx 1.1 / \times 10^3$ [1] and $\Omega_{r0} \ll \Omega_{m0}$

$$\theta(a_l) \approx 1.6^\circ \quad (1.49)$$

where we use $a_l/a_0 = (1 + z_l)^{-1} \approx 10^{-3}$. Note that we ignore the Dark Energy, but this will not change so much the conclusion (besides this component starts to dominate the universe just recently). This result is clearly a problem, once scales so much larger than 1.6° are observed with the same mean temperature in the sky (they were in thermal equilibrium in some way). This mismatch is called *Horizon Problem*

1.3.7 Flatness Problem

As we said, the spatial curvature of the universe is contained in the scalar constant K . Recent measurement shown with 68% of confidence that $|\Omega_{k0}| = 0.0007 \pm 0.0019$ [1]. Looking with more attention to the equation (1.43), the solution for $K = 0$ is unstable. To be clear, redefine the densities normalizing them with respect the critical density in any time $\Omega_x \equiv \frac{\rho_x}{\rho_{cr}}$, them

$$|\Omega(t)^{-1} - 1|\rho a^2 = \frac{3k}{8\pi G} \quad (1.50)$$

now, Ω refers just to material components of the universe. Note that in radiation age $\rho a^2 \propto t^{-1}$, and in matter age $\rho a^2 \propto t^{-2/3}$. Assuming that k is different from zero, to remain the right side of equation (1.50) constant the term $|\Omega^{-1} - 1|$ needs to increase. Then we have that any initial deviation from $\Omega \neq 1$, o equivalent $k \neq 0$, would create a large curvature today. This fine-tuning, that is, this adjust of an initial curvature very small is called *Flatness Problem*. So the problem remains in asking what happens in the initial universe to this condition ($k = 0$) to keep the truth.

1.4 Inflation

Inflation is a theory about the very early universe, which arises from attempts to solve the Horizon and Flatness problems. In the Horizon problem, the universe is actually, isotropic and homogeneous in scales larger than we can calculate, so the experiments suggest that the comoving horizon is larger than we expect. In the flatness problem, we hope a fine-tuning of Ω_k to very small values, which suggests that something could happen before the radiation age decreasing the value of it so much. Note that, the solution for this problem can be reached if we assume a phase of fast expansion in the very early universe before the radiation age, as it will be shown.

- **Solution for Horizon Problem**

Consider an exponential expansion of the universe

$$a(t) = a_f e^{-H_I(t_f - t)} \quad (1.51)$$

Where t_f denotes the time when the inflation ended and t some period during that. H_I is the Hubble constant in this period, which is constant. Using this functional form, we see that now

$$D_{\eta_I} \approx \frac{a(t_i)}{a(t_f)} \frac{(e^N - 1)}{H_I} \quad (1.52)$$

$$D_A \approx \frac{a(t_i)}{H_0} \quad (1.53)$$

where $N = H_I(t_f - t_i)$, and t_i denote the beginning of this phase of expansion. In order this solve the problem is necessary $D_{\eta_I} > D_A$, then as $\frac{D_{\eta_I}}{D_A} \approx \frac{H_0}{a_f H_I} e^N$

$$e^N > \frac{a_f H_I}{H_0} \quad (1.54)$$

Then, exist a value N to solve this problem.

- **Solution for Flatness Problem**

In the final of inflation, the value of the Ω_k is

$$|\Omega_{k_f}| = \frac{|k|}{a_f^2 H_I^2} = \frac{|k|}{a_i^2 H_I^2} e^{-2N} \quad (1.55)$$

then $\frac{\Omega_{k_f}}{\Omega_{k_i}} = e^{-2N}$. this means

$$|\Omega_{k_0}| = \frac{|K|}{H_0^2} = |\Omega_{k_i}| \left(\frac{a_f H_I}{H_0} \right)^2 e^{-2N} \quad (1.56)$$

The condition $|\Omega_{k_0}| < 1$ gives

$$e^N > \frac{a_f H_I}{H_0} \quad (1.57)$$

Assuming that $|\Omega_{k_i}|$ is of order 1, that is, the same solution for the Horizon problem.

Then, we have seen that an exponential expansion in the very early universe can explain these problems. The great problem is to build a dynamical model that creates these kinematics features on the expansion, that is, a model that allows an exponential expansion by a finite period, and connects it with the radiation-dominated universe smoothly.

1.4.1 Inflaton

There are many theories of inflation that try to describe the early universe. One of the most simple is considered a single uniform scalar field in the universe, called *Inflaton*, which is responsible to drive the expansion in this phase. It has a very simple Lagrangian as well, just with a kinematic term and a potential $V(\phi)$

$$L = \frac{1}{2}g^{\mu\nu}\partial_\mu\phi\partial_\nu\phi + V(\phi) \quad (1.58)$$

The Energy-Momentum tensor of this scalar field is

$$T_\nu^\mu = g^{\mu\alpha}\partial_\alpha\phi\partial_\nu\phi - \delta_\nu^\mu \left(\frac{1}{2}g^{\alpha\beta}\partial_\alpha\phi\partial_\beta\phi + V(\phi) \right) \quad (1.59)$$

where the prime denotes the derivative with respect to ϕ . The Friedmann Equations for this field is

$$H^2 = \frac{8\pi G}{3} \left(\frac{1}{2}\dot{\phi}^2 + V(\phi) \right) \quad (1.60)$$

$$\frac{\ddot{a}}{a} = -\frac{8\pi G}{3} (\dot{\phi}^2 - V(\phi)) \quad (1.61)$$

To describe an exponentially accelerated universe it is necessary that H be approximately constant, which means

$$\frac{|\dot{H}|}{H^2} = \left| \frac{\ddot{a}}{aH^2} - 1 \right| \ll 1 \quad (1.62)$$

using the field equations this gives the condition

$$V(\phi) \gg \dot{\phi}^2 \quad (1.63)$$

This condition is called *Slow-Roll Condition*. Note, from (1.59), that condition simulate the equation of state of cosmological constant $P_\phi \approx -\rho_\phi \approx -V(\phi) \approx \text{constant}$. Then, following this strategy, this theory can describe a stage of exponential expansion that ends in a finite time, and connect to the expansion history that we already know.

1.4.2 Origin of Perturbations

Despite the inflation have been created to solve a set of problems, it also might have been brought the explanation for the origin of inhomogeneity in the universe, which is necessary to structure formations as we see today. Inflation is an age that connects the quantum to the classical phase of the universe (here the word "classical" means classical scales, where quantum effects are not relevant anymore). The limitations in determining, with exact precision, the energy and time in each region of the quantum scalar field have important consequences. This means that the period of inflation could be not finished at the same time to all regions of the field, and so created inhomogeneities (regions with more and less energy) propagated to classical scales at the end of the inflation. As we will see in the next chapter, these perturbations, which impact the total metric and energy-momentum of the universe, are essential to explain the large structures that we see in the universe today.

The inflation theories provide a rich discussion about the initial conditions of the universe, moreover, there are many scenarios and different models of inflation. A deeper discussion about that can be found in [25] and [26], once the inflation is out of the scope of this work.

1.5 Λ CDM

As said before, many cosmological models try to explain all the observations that we have shown in the last sections. Although the existence of so many models (including those who consider modifications on Einstein's Equations), the most successful model is based on GR, including in the Field Equations the cosmological constant, describing the dynamics of the universe driven by a supposed existence of *Dark Energy* (DE), and *Cold Dark Matter* (CDM), a non-relativistic matter that interacts just by gravitation with the equation of state given by $p = 0$. This model is called by Λ CDM. In the last section, it was shown the FLRW metric, but just this metric does not allow us to describe the evolution of inhomogeneities, which must have produced the large structures (galaxies and agglomeration of it) that are observed. Then, the metric considered in the Λ CDM model is like $g_{\mu\nu} = \bar{g}_{\mu\nu} + \delta g_{\mu\nu}$, where $\bar{g}_{\mu\nu}$ is the flat FLRW metric ($K = 0$) and $\delta g_{\mu\nu}$ is a fluctuation around the background (FLRW). The evolution of the universe with this metric is more explored in the next chapter 2.

1.5.1 Model Parameters

The Λ CDM model has six independent parameters, from which it is possible to calculate the other cosmological parameters that appear in the model. The best values for them are given in the Table 1

Parameter	Value \pm Constraint (68% limit)
$\Omega_b h^2$	0.02242 ± 0.00014
$\Omega_c h^2$	0.11933 ± 0.00091
100θ	1.04101 ± 0.00029
τ	0.0561 ± 0.0071
$\ln(10^{10} A_s)$	3.047 ± 0.014
n_s	0.9665 ± 0.0038

Table 1 – Results for six parameters of Λ CDM model reported by the analysis of data from Planck 2018 (P18) CMB power spectrum [1]. Note, some parameters are measured in terms of $H_0 = 100h$.

Ω_c and Ω_b are the present energy density (normalized by the critical density) for CDM and ordinary matter (often called baryons). θ is the angular scale of the sound horizon at the last scattering surface. τ is the optical depth in the epoch of reionization. A_s and n_s are the amplitude and tilt, respectively, of fluctuations predicted by inflation. From these parameters, it infers that the present universe is dominated by Dark Energy, with density energy about $\Omega_\Lambda \approx 0.6889 \pm 0.0056$, causing the accelerated expansion.

1.5.2 Hubble’s Tension

Although the great success of the Λ CDM model, it has showing inconsistencies between independent measurements over the last years. The main tension is about the value of H_0 measured by cosmological model-independent methods (or almost independent) and by methods that assume the Λ CDM as the base model. For instance, the recent work R20 [2] uses the calibration of the Cepheid distance ladder to infer the actual Hubble’s parameter ($H_0 \approx 73.22 \pm 1.82 \text{ Kms}^{-1} \text{ Mpc}^{-1}$), without assuming a cosmological model. This result is clearly in a mismatch with the result from P18, which infers $H_0 \approx 67.66 \pm 0.42$ (which assumes the Λ CDM model in general analysis). The general panorama of the situation is shown in Fig. 3. Almost one decade that this tension persists and many attempts to solve this problem emerged. There are issues about the systematic errors on ladder distance calibration used in the determination of H_0 , as well as issues concerning to the use of Λ CDM in the analysis of data. However, the results of R20 and P18 come from a series of improvements over the years, pointing to an increase in the mismatch. Other attempts to investigate that problem involves alternative models, for example models with DE interacting [27], dynamic equation of state for DE [28] or modified gravity [29] [30] [31]. A full review of this tension can be found in the work [3].

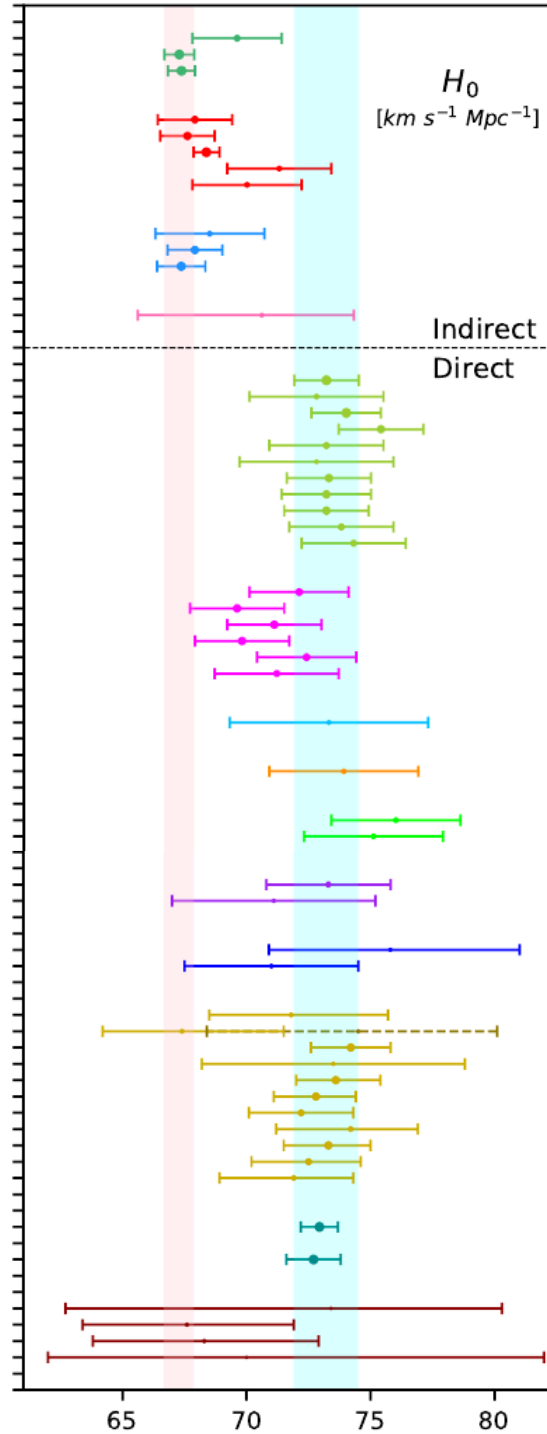


Figure 3 – This figure [3] shows the last direct and indirect measurements of H_0 with 68% confidence level. The region with color cyan defines the last value of H_0 given by SH0ES Team (R20) while the red region is the last value given by the Planck 2018 (PL18).

1.5.3 Growth of Structures Tension

As said before, the modern description of the universe is through a metric composed by a homogeneous and isotropic part (background) plus small perturbations. The first

order of perturbation in cosmology (which will be shown in the next chapter) is well known and to obtain more information about the evolution and formation of structures it is necessary going beyond, the nonlinear regimes (second order or larger). An important parameter is the variance of perturbation in scales where the nonlinear contributions are relevant (scales about $r = 8h^{-1}Mpc$). This parameter measures the rate of growth of structures in the Universe and is labeled by σ_8 . A considerable tension between the value of σ_8 has been revealed in the last years (see Fig. 4).

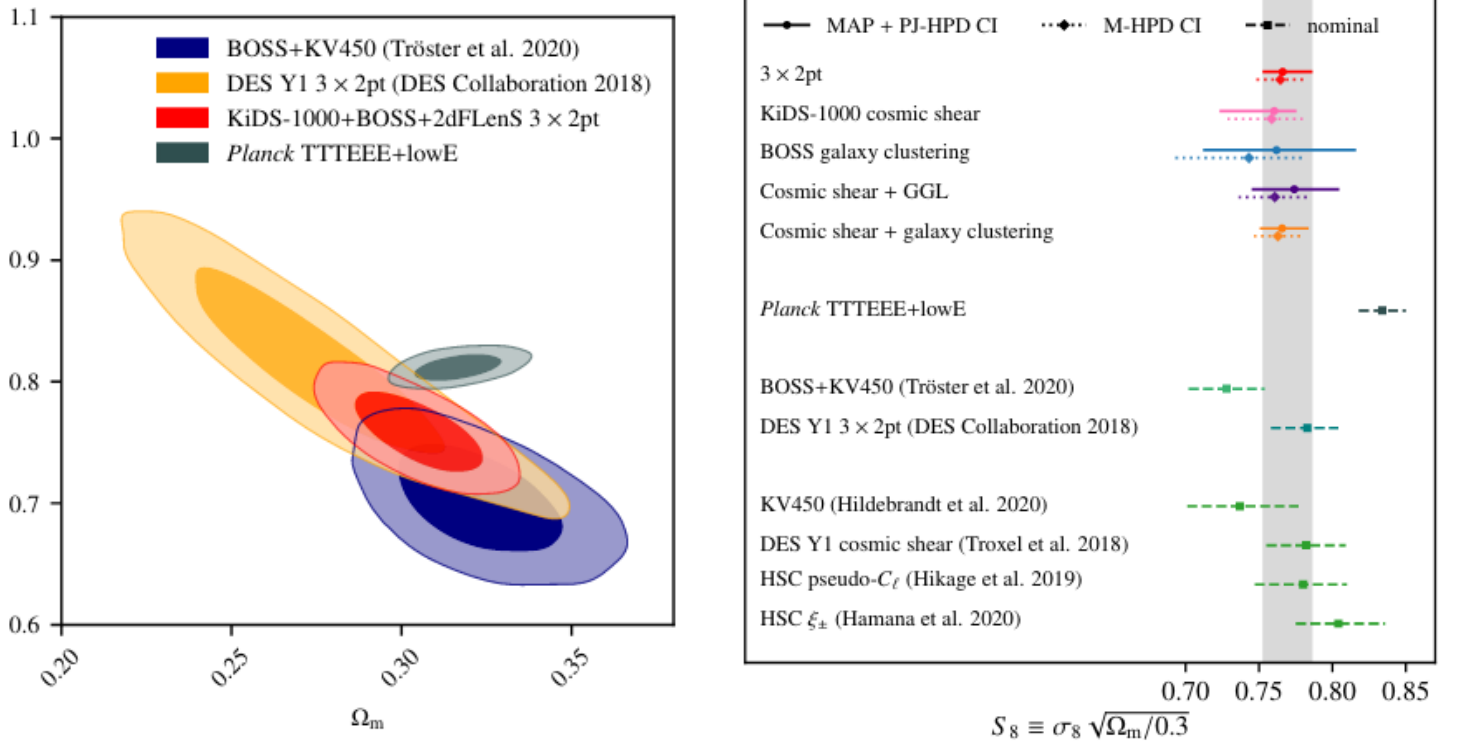


Figure 4 – The left image shows the marginalized posterior distribution in the σ_8 and Ω_m . The right image the constraints on the structure growth parameter S_8 for different probe combinations over last years [9].

It is common use the parameter $S_8 \equiv \sigma_8 \sqrt{\Omega_m/0.3}$ (there are some degeneracy between σ_8 and Ω_m) to quantify this tension. The last results of PL18, with weak lensing measurements, is about $S_8 = 0.834 \pm 0.016$ (assuming Λ CDM model) while the combination results between BOSS and KV450 $S_8 = 0.728 \pm 0.026$ [32]. The left plot 4 of posterior distributions of Ω_m and σ_8 can show this tensions as well. This tension could arise from systematic errors, but other solutions are being investigated and showing an interesting aspect of this tension. It has been found smaller values for σ_8 when considering the same model solutions proposed to alleviate the H_0 tension. In other words, the consistent solutions for this tension (solutions that try to solve more than one problem) involve, for example, Interacting DE, Decaying DM [33] [34] and Modified Gravity Models.

2 PERTURBATIONS ON COSMOLOGY

In the last chapter, it was introduced the main experimental results of the Λ CDM model. Here, we will see how is done the treatment of perturbation in cosmology. The cosmological principle says that the universe is homogeneous and isotropic at large scales, but if we want to understand the evolution of the universe we can not limit ourselves for that. Looking to the sky, we can see large structures like galaxies and clusters which could not be formed in a universe perfectly homogeneous and isotropic. So, wondering about that, we say that the metric of the universe is close to Friedmann-Robertson-Walker, but it is disturbed by very small perturbations (which create the inhomogeneity and anisotropy).

$$g_{\mu\nu} = a(\eta)^2(\eta_{\mu\nu} + h_{\mu\nu}) \quad (2.1)$$

where $a(\eta)$ is the scale factor described by the conformal time and $|\eta_{\mu\nu}| \gg |h_{\mu\nu}|$, that means, the FRW metric works as a background evolution of the universe, and over that there are superpositions of some smaller functions that disturb the background metric. The goal here is to explore the evolution of the universe and its perturbations until the first order (linear order).

2.1 Gauge Freedom

In general relativity there is what we call general symmetry, that is, the physics laws are valid in all reference frames (connected by general coordinate transformations). As we are writing the metric in the form given by the equation (2.1), it breaks down partially this symmetry, such that there is a set of frames where that formula is allowed. These frames are connected by the transformations like

$$\tilde{x}^\mu = x^\mu + \xi^\mu(x) \quad (2.2)$$

where $\xi^\mu(x)$ is a function of the spacetime that satisfy the conditions $|\partial\xi| \sim |\xi| \ll |\eta_{\mu\nu}|$. Then, the frames (Gauges) that we can choose to write the metric in the form of (2.1) are connected by the vector $\xi^\mu(x)$. This freedom of choice to describe the metric is called *Gauge Freedom*.

2.1.1 Decomposition of Perturbations

The metric perturbations can be decomposed into three contributions, scalars, vectors, and tensors. The full metric is written as

$$g_{\mu\nu} = a^2(\eta) \begin{bmatrix} -[1 + 2\psi(\eta, \vec{x})] & w_i(\eta, \vec{x}) \\ w_i(\eta, \vec{x}) & \delta_{ij}[1 + 2\phi(\eta, \vec{x})] + H_{ij}(\eta, \vec{x}) \end{bmatrix} \quad (2.3)$$

Actually, we can split it more and extract from this a complete set of functions (scalars, vectors, tensors) that really evolve independently at first order in the perturbations. Then we decompose the perturbations as

$$w_i = \partial_i w + S_i \quad (2.4)$$

$$H_{ij} = 2 \left(\partial_i \partial_j - \frac{1}{3} \delta_{ij} \nabla^2 \right) \mu + \partial_i A_j + \partial_j A_i + H_{ij}^T \quad (2.5)$$

Where the perturbations w_i and H_{ij} were exchanged by two scalar functions w, μ two 3-vector functions S_i, A_i (with constraint $\partial_i S^i = \partial_i A^i = 0$) and one tensor field H_{ij}^T (with constraint $\partial^j H_{ij}^T = 0$). Note that the number of freedom degrees is the same, it is just a decomposition of perturbations fields.

$$g_{\mu\nu} \begin{cases} \text{Four scalar functions} & \psi, \phi, w, \mu \\ \text{Two divergenceless 3-vectors} & S_i, A_i \\ \text{Transverse and Traceless spatial tensor of rank 2} & H_{ij}^T \end{cases} \quad (2.6)$$

As said before, that decomposition is useful at the first order of perturbation because scalars, vectors, and tensors perturbations evolve independently, so we can separate the equations for each kind of perturbation and study their contributions to the evolution of the universe separately (more discussion about it in [35]).

The gauge freedom allows us to choose a particular gauge where the calculations can be more convenient, and connect the results with expressions that are invariant by gauge transformations. In order to do that, it is important to know how the perturbations from different gauges relate to each other. The metric changes over this gauge transformation, at first order, like

$$g_{\mu\nu}(x) = \frac{\partial \tilde{x}^\alpha}{\partial x^\mu} \frac{\partial \tilde{x}^\beta}{\partial x^\nu} \tilde{g}_{\alpha\beta}(\tilde{x}) \approx \tilde{g}_{\mu\nu}(x) + \partial_\sigma g_{\mu\nu}(x) \xi^\sigma + \partial_\mu \xi^\sigma g_{\sigma\nu}(x) + \partial_\nu \xi^\sigma g_{\sigma\mu}(x) \quad (2.7)$$

Where the tilde represents another gauge coordinate. Then, with the above equation, we can know how the perturbations on the metric change over gauge transformations. For instance, the scalar perturbations transform like

$$\tilde{\psi} = \psi - H\alpha - \alpha' \quad (2.8)$$

$$\tilde{\phi} = \phi - H\alpha - \frac{1}{3}\nabla^2\beta \quad (2.9)$$

$$\tilde{w} = w - \beta' + \alpha \quad (2.10)$$

$$\tilde{\mu} = \mu - \beta \quad (2.11)$$

where the vector ξ^μ was rewritten like

$$\xi^0 = \alpha \quad (2.12)$$

$$\xi^l = \partial_l\beta + \omega_l \quad (2.13)$$

with α and β are scalar functions and ω_l a divergences vector ($\partial^l\omega_l = 0$). For vector and tensor perturbations the transformations are

$$\tilde{S}_i = S_i - \omega'_i \quad (2.14)$$

$$\tilde{A}_i = A_i - \omega_i \quad (2.15)$$

$$\tilde{H}_{ij}^T = H_{ij}^T \quad (2.16)$$

From these expressions we can define invariant perturbations, that is perturbations that do not change with the gauge transformation. Two useful scalar invariant perturbations are

$$\Psi \equiv \psi + \frac{1}{a} [(w - \mu')a]' \quad (2.17)$$

$$\Phi \equiv \phi + H(w - \mu') - \frac{1}{3}\nabla^2\mu \quad (2.18)$$

The above perturbations are called *Bardeen's potentials*. These invariant scalar perturbations are useful to analyze the formation of large structures in the universe because they connect the results of different gauges.

2.1.2 Gauges Examples

As the gauge freedom remains on the choice of ξ^μ , we can use this to decrease the number of perturbations and simplify our calculations. The most common gauges on cosmology are

- **Synchronous Gauge:**

This is a gauge where we choose ξ^μ such that $\tilde{\psi} = 0$ and $\tilde{w}_i = 0$. In another words, starting from a general gauge with coordinates x , the vector $\xi(x)$ for this transformations is defined by

$$\psi - H\alpha - \alpha' = 0 \quad (2.19)$$

$$w - \beta' + \alpha = 0 \quad (2.20)$$

$$S_i - \omega'_i = 0 \quad (2.21)$$

Since we can solve these equations to α , β , and ω_i , it means this gauge is well defined. In that gauge, the metric assumes the form

$$\tilde{g}_{\mu\nu} = a^2 \begin{bmatrix} -1 & 0 \\ 0 & \delta_{ij}(1 + 2\tilde{\phi}) + \tilde{H}_{ij} \end{bmatrix} \quad (2.22)$$

In this gauge the invariant perturbations that we have seen can be written as:

$$\tilde{\Psi} = \frac{1}{a}(\tilde{\mu}'a)' \quad (2.23)$$

$$\tilde{\Phi} = \tilde{\phi} - H\tilde{\mu}' - \frac{1}{3}\nabla^2\tilde{\mu} \quad (2.24)$$

- **Newtonian Gauge:**

This is the gauge when $\tilde{w} = 0$, $\tilde{\mu} = 0$ and $\partial_i\tilde{A}_j + \partial_j\tilde{A}_i = 0$. This is allowed by the α , β and ω that solve the system below:

$$w - \beta' + \alpha = 0 \quad (2.25)$$

$$\mu - \beta = 0 \quad (2.26)$$

$$A_i - \omega_i = 0 \quad (2.27)$$

As this system can be solved, the metric written with this gauge assumes the expression

$$\tilde{g}_{\mu\nu} = a^2 \begin{bmatrix} -(1 + 2\tilde{\psi}) & \tilde{S}_i \\ \tilde{S}_i & \delta_{ij}(1 + 2\tilde{\phi}) + \tilde{H}_{ij}^T \end{bmatrix} \quad (2.28)$$

In that frame the invariant perturbations assumes a simple form:

$$\tilde{\Psi} = \tilde{\psi} \quad (2.29)$$

$$\tilde{\Phi} = \tilde{\phi} \quad (2.30)$$

That is, the scalar potentials of the metric on the Newtonian gauge are invariant perturbations.

2.2 Perturbations in Einstein's Field Equations

The evolution of the universe is given by the Field's Equations with the metric perturbed and the complete energy momentum-tensor defined by

$$T_{\mu\nu} = \rho u_\mu u_\nu + q_\mu u_\nu + q_\nu u_\mu + (P + \pi)\theta_{\mu\nu} + \pi_{\mu\nu} \quad (2.31)$$

where u_μ is the four-velocity of fluid that fills the universe (with $g_{\mu\nu}u^\mu u^\nu = -1$), $\theta_{\mu\nu} \equiv g_{\mu\nu} + u_\mu u_\nu$ (called projector on the hypersurface orthogonal to the four-velocity), q_μ is the *Heat Transfer* contribution ($q_\mu u^\mu = 0$) and $\pi_{\mu\nu}$ is the part traceless of *Anisotropic Stress* (satisfy $\pi_{\mu\nu}u^\nu = 0$), while the π is the trace from anisotropic stress called *Bulk Viscosity*. Consider all terms of the energy-momentum is necessary since the universe is not homogeneous and isotropic. At first order, the Field's Equations is just that

$$\delta G_\nu^\mu = 8\pi G \delta T_\nu^\mu \quad (2.32)$$

Once using the perturbation theory and decomposition of the perturbation in the metric, we can calculate the connection and curvature tensor (besides Ricci's tensor and scalar) at first order in perturbation. The first order of Einstein's tensor becomes

$$2a^2 \delta G_0^0 = 4H h_{k0,k} - 6H^2 h_{00} - 2H h'_{kk} + \nabla^2 h_{kk} - h_{kl,kl} \quad (2.33)$$

$$2a^2 \delta G_i^0 = 2H h_{00,i} + \nabla^2 h_{0i} - h_{k0,ki} + h'_{kk,i} - h'_{ki,k} \quad (2.34)$$

$$\begin{aligned} 2a^2 \delta G_j^i &= (h_{00} - h_{kk})_{,ij} + (h_{ki,j} + h_{kj,i})_{,k} + \left(\frac{d^2}{d\eta^2} - \nabla^2 \right) h_{ij} - \left(\frac{d}{d\eta} + 2H \right) (h_{0i,j} - h_{0j,i}) \\ &+ \left[2H^2 h_{00} + \nabla^2 (h_{kk} - h_{00}) + 2 \left(\frac{d}{d\eta} + 2H \right) h_{k0,k} - 4 \frac{a''}{a} h_{00} - 2H (h'_{00} + h'_{kk}) - h_{kl,kl} - h''_{kk} \right] \delta_j^i \end{aligned} \quad (2.35)$$

Where we are using the notation $\partial_\mu (\dots) \equiv (\dots)_{,\mu}$. The Energy-momentum tensor at first order is given by

$$T_0^0 = -\bar{\rho}(1 + \delta) \quad (2.36)$$

$$T_i^0 = (\bar{\rho} + \bar{P})v_i + \frac{q_i}{a} \quad (2.37)$$

$$T_0^i = (\bar{\rho} + \bar{P})(h_{0i} - v_i) - \frac{q_i}{a} \quad (2.38)$$

$$T_j^i = (\bar{P} + \delta P + \pi) \delta_j^i + \pi_j^i \quad (2.39)$$

where the $\delta \equiv \frac{\delta\rho}{\bar{\rho}}$ (*density contrast*) and $\delta u_i \equiv av_i$. Here we have used the normalization of four-velocity, which gives $\delta u_0 = \frac{h_{00}a}{2}$ and $v_i = h_{i0} + a\delta u^i$. As we are interested in the first order of perturbation, we can separate the scalar, vector and tensor perturbations (as said in the last section). So, now the scalar perturbations will be the focus of this section, once it is the most important contribution to large structure formation.

2.2.1 Scalar Perturbations in Field Equations

Now, to obtain any advance, it is useful to choose a gauge to write down the Field's Equations. We focus here on the Newtonian Gauge. As we are interested just in scalar perturbations, and each kind of perturbations evolve separately, then we use the metric in the form:

$$g_{\mu\nu} = a^2 \begin{bmatrix} -(1 + 2\psi) & 0 \\ 0 & \delta_{ij}(1 + 2\phi) \end{bmatrix} \quad (2.40)$$

Using this gauge, the equations (2.35) and (2.36) until (2.39), the disturbed field equations (2.32) turns out

$$3H\Phi' - 3H^2\Psi - \nabla^2\Phi = 4\pi Ga^2\delta\rho \quad (2.41)$$

$$\partial_i(\Phi' - H\Psi) = 4\pi Ga^2(\rho + P)v_i \quad (2.42)$$

$$\Phi'' + 2H\Phi' - H\Psi' - (2H' + H^2)\Psi - \frac{1}{3}\nabla^2(\Phi + \Psi) = -4\pi Ga^2\delta P \quad (2.43)$$

$$\left(\partial^i\partial_j - \frac{1}{3}\delta_j^i\nabla^2 \right) (\Psi + \Phi) = 8\pi Ga^2\pi_j^i \quad (2.44)$$

Where the last equation can be find out calculating the part traceless of δG_j^i . Besides that $\delta\rho = \sum_l \delta\rho_l$ is the total perturbation of energy density, such that the subindex runs over the constitutes of the universe (Cold dark matter, Baryon, Photons and Neutrinos), then using the density contrast $\delta_l = \frac{\rho_l - \bar{\rho}_l}{\bar{\rho}_l} = \frac{\delta\rho_l}{\bar{\rho}_l}$ it get $\delta\rho = \bar{\rho}_c\delta_c + \bar{\rho}_b\delta_b + \bar{\rho}_\gamma\delta_\gamma + \bar{\rho}_\nu\delta_\nu$. Note also that $(\rho + P)v_i = \sum_l(\rho_l + P_l)(v_l)_i$.

To eliminate the spatial derivatives, we can write the perturbations as a sum of Fourier modes, that is, $F(\eta, \vec{x}) = \int d^3 \frac{\vec{k}}{(2\pi)^3} F(\eta, \vec{k}) e^{i\vec{k}\cdot\vec{x}}$ (where $F(\eta, \vec{x})$ and $F(\eta, \vec{k})$ do not have the same functional form, that is, we are using this to refer about the spatial function and Fourier modes by abuse of notation).

$$3H\Phi' - 3H^2\Psi + k^2\Phi = 4\pi G a^2 (\rho_c \delta_c + \rho_b \delta_b + \rho_\gamma \delta_\gamma + \rho_\nu \delta_\nu) \quad (2.45)$$

$$k(H\Psi - \Phi') = 4\pi G a^2 \left(\rho_c V_c + \rho_b V_b + \frac{4}{3}(\rho_\gamma V_\gamma + \rho_\nu V_\nu) \right) \quad (2.46)$$

$$\Phi'' + 2H\Phi' - H\Psi' - (2H' + H^2)\Psi + \frac{1}{3}k^2(\Phi + \Psi) = -4\pi G a^2 \delta P \quad (2.47)$$

$$k^2(\Psi + \Phi) = 12\pi G a^2 \hat{k}^i \hat{k}_j \pi_i^j \quad (2.48)$$

Where we have defined for each constitute of energy-momentum the perturbation $V_l = \frac{k^j (v_l)_j}{k}$ and used the equation of state for each of them ($w_c = w_b = 0$ and $w_\gamma = w_\nu = \frac{1}{3}$). Since there is no second-order or higher term then the equations describe the evolution of each k-mode independently, which means there is no coupling between different k-modes (for example if there is a term like $\Phi^2(x)$ then in the Fourier transformation would appear $\Phi(k_1)\Phi(k_2)$, creating coupling between different modes).

2.3 Boltzmann Equations

Einstein's equations from the last section are not enough to describe the evolution of scalar perturbations yet (there are many perturbations for the number of independent equations). Studying the thermal history of the universe, we know that not just gravity is important to the behavior of the species distributions but also the non-gravitational interactions between them. Then, we can deal with the Boltzmann equations relativistic to obtain other equations that couple the energy-momentum perturbation with metric perturbations. With that in mind, a distribution function in the phase-space is associated to each fluid in the universe. Writing the distribution as $f = f(x^\mu, P^\mu)$ and using a λ as affine parameter ($P^\mu = \frac{dx^\mu}{d\lambda}$) the Boltzmann equation says

$$\frac{df}{d\lambda} = C[f] \quad (2.49)$$

$$(2.50)$$

that means, the variation (along a path parametrized by λ) of particles into a volume in the phase-space comes from what is called *Collisional* term ($C[f]$), which contains information about interactions of particles like creation, annihilation, energy and momentum exchange between particles. Note that the energy, P^0 is constrained by

mass-shell relation $g_{\mu\nu}P^\mu P^\nu = -m^2$, then the distribution can be write with dependency just in (x^μ, \vec{p}) . Besides that, as we want to include the perturbations in the equations we split the distribution function as

$$f(\eta, \vec{x}, \vec{p}) = \bar{f}(\eta, p) + \delta f(\eta, \vec{x}, \vec{p}) \quad (2.51)$$

where \bar{f} is the background contribution, while δf is the perturbation on that. Note that the background depends just on η and modulus of momentum p , consistent with homogeneity and isotropy. Using $P^0 = \frac{d\eta}{d\lambda}$ the Boltzmann equation until first order turns out

$$\frac{df}{d\eta} = \frac{\partial f}{\partial \eta} + \frac{\partial f}{\partial x^i} \frac{P^i}{P^0} + \frac{\partial f}{\partial p} \frac{dp}{d\eta} = \frac{1}{P^0} C[f] \quad (2.52)$$

To insert the metric perturbations, we use a gauge where $h_{0i} = 0$ (which is true for scalar perturbations in Newtonian and Synchronous Gauges for example) to calculate the $\frac{dp}{d\eta}$, then the first order of equation gives

$$\delta f' + \frac{ikp\mu}{E} \delta f - Hp \frac{\partial}{\partial p} (\delta f) + \left(ikE\mu \frac{h_{00}}{2} - \frac{p}{2} h'_{ij} \hat{p}^i \hat{p}^j \right) \frac{\partial \bar{f}}{\partial p} = \frac{a}{E} C[f] \quad (2.53)$$

where the fourier transformation already was applied with $\mu \equiv \hat{k} \cdot \hat{p}$ and the definitions $E \equiv a^2(1 - h_{00})(P^0)^2$ and $p^2 = a^2(\delta_{ij} + h_{ij})P^i P^j$. Choosing the Newtonian gauge again, the Boltzmann equation for scalar perturbations at first order becomes

$$\delta f' + \frac{ikp\mu}{E} \delta f - Hp \frac{\partial}{\partial p} (\delta f) - (p\Phi' + ikE\mu\Psi) \frac{\partial \bar{f}}{\partial p} = \frac{a}{E} C[f] \quad (2.54)$$

This equation applies to each fluid that fills the universe. In the next sections, we will see how are the equations of scalar perturbations for Photons and Baryons, which are the most relevant to understand the Baryonic Acoustics Oscillations (BAO).

2.3.1 Radiation

In the early universe, the interactions between particles are so important as gravity, and then, it's necessary to calculate the right side of the equation (2.54). At the very early universe (radiation-dominated universe) the mean temperature is high enough for the neutrinos to behaves like radiation. However, even in the early universe neutrinos are very weak interact particles, and that interaction rate decrease with temperature, thus their collision term is negligible. We separate here the Boltzmann equations for photons and neutrinos.

2.3.2 Photons

The main interaction that involves the photons is the Thomson scattering

$$e^-(\vec{q}) + \gamma(\vec{p}) \longrightarrow e^-(\vec{q}') + \gamma(\vec{p}') \quad (2.55)$$

where the intensity of the photon's momentum does not change. Here we neglect the interaction with protons because its cross-section decays with the mass of particle squared, and as proton's mass is about $m_p \approx 10^3 m_e$ this interaction is irrelevant here. Denoting the perturbation on distribution function as $\delta f \equiv F$, the collision term is given at first order by

$$C[F(\vec{p})] = \int \int \int \frac{d^3 \vec{q} d^3 \vec{q}' d^3 \vec{p}'}{(2\pi)^5 2^3 E_e(q) E_e(q') E_e(p)} \delta^3(\vec{p} + \vec{q} - \vec{p}' - \vec{q}') \delta(p + E_e(q) - p' - E_e(q')) \Delta f \quad (2.56)$$

It include the energy and momentum conservation, and the balance between the concentration of each particle in the reaction given by the term $\Delta f \equiv \bar{f}_e(q') F_\gamma(\vec{p}') + \bar{f}_\gamma(p') F_e(\vec{q}') - \bar{f}_e(q) F_\gamma(\vec{p}) - \bar{f}_\gamma(p) F_e(\vec{q})$. The $|M|^2$ is related with the amplitude of probability for this interaction occur (symmetrically in relation to direction of interaction). It can be shown that

$$C[F(\vec{p})] = \frac{p\tau'}{a} \left(F_\gamma(\vec{p}) + \frac{\partial \bar{f}_\gamma}{\partial p} \vec{v}_b \cdot \vec{p} \right) + \frac{pn_e}{32\pi^2 m_e^2} \int d^2 \hat{p}' |M(\hat{p}, \hat{p}')|^2 F_\gamma(\vec{p}') \quad (2.57)$$

where $\tau(\eta) = \int_\eta^{\eta_0} d\eta' n_e \sigma_T a$, is called *Optical Depth*, which measure how much strong is the interaction. Consider now the distribution of photon gas (Bose-Einstein distribution), which is the background distribution. This background distribution of momentum of photons is parametrized by the temperature. Then, the perturbation on the distribution can be understood as a perturbation on the temperature field (using Boltzmann's constant $K_b \equiv 1$).

$$f(\eta, \vec{x}, \vec{p}) = \frac{1}{e^{\frac{p}{T}} - 1} \quad (2.58)$$

The temperature field is written as $T = \bar{T}(\eta) + \delta T(\eta, \vec{x}, \vec{p})$, where $\frac{|\delta T|}{\bar{T}} \ll 1$. Expanding this distribution at first order, we have

$$f = \bar{f} - p \frac{\partial \bar{f}}{\partial p} \frac{\delta T}{\bar{T}} \quad (2.59)$$

then, $\delta f \equiv F = -p \frac{\partial \bar{f}}{\partial p} \frac{\delta T}{T}$. If we multiply by p and integrate the equation (2.54) over momentum modulus

$$\Theta' + i\mu k \left(\Theta - \frac{h_{00}}{2} \right) + \frac{h'_{ij} \hat{p}^i \hat{p}^j}{2} = \frac{a}{4\rho_\gamma} \int \frac{dpp^2}{2\pi^2} C[F_\gamma(\vec{p})] \quad (2.60)$$

where we use the definition $\Theta(\eta, \vec{k}, \hat{p}) \equiv \frac{1}{4\rho_\gamma} \int \frac{dpp^3}{2\pi^2} F_\gamma$. The Θ is related to the perturbation on the intensity of the temperature field. Although that, to have a complete description of the perturbations on photons gas it is necessary to consider the perturbation on the photon's polarization states, which can be introduced in the equation by Stokes parameters. Here we will focus only on the fluctuations on the temperature field Θ . the equation above can be written as

$$\Theta' + i\mu k(\Theta + \Psi) + \Phi' = -\tau' \left(\Theta_0 - \Theta - i\mu V_b - \frac{1}{2} P_2(\mu) \Theta_2 \right) \quad (2.61)$$

where it was used the Newtonian Gauge and the expansion $\Theta_n = \frac{1}{(-i)^n} \int_{-1}^1 \frac{d\mu}{2} P_n(\mu) \Theta(\mu)$ with P_n being a *Legendre Polynomial* of n-th degree. If consider the perturbations on polarization states, it couple with this equation inserting new terms like $\Theta_{P2} + \Theta_{P0}$ (Θ_{Pn} is the n-th coefficient of Legendre expansion for polarization perturbations), as shown in [35]. The equation above can be expanded in Legendre Polynomials (multipole expansion) using the definition of Θ_n and the orthogonal relation $\int_{-1}^1 P_m(\mu) P_n(\mu) d\mu = \frac{2}{2n+1} \delta_{mn}$, then

$$\Theta'_0 + k\Theta_1 = -\Phi' \quad (\text{Monopole } n = 0) \quad (2.62)$$

$$3\Theta'_1 + k(2\Theta_2 - \Theta_0) = k\Psi + \tau'(3\Theta - V_b) \quad (\text{Dipole } n = 1) \quad (2.63)$$

$$10\Theta'_2 + 2k(3\Theta_3 - 2\Theta_1) = 9\tau'\Theta_2 \quad (\text{Quadrupole } n = 2) \quad (2.64)$$

$$(2n+1)\Theta'_n + k((n+1)\Theta_{n+1} - n\Theta_{n-1}) = \tau'(2n+1)\Theta_n \quad (\text{Multipoles } n > 2) \quad (2.65)$$

This infinite set of equations are called the multipole hierarchy of photons, once the multipole Θ_n depends on the multipoles Θ_{n+1} and Θ_{n-1} , and so on. Clearly, to solve these equations it is necessary to use some criteria to truncate the series for a certain $n = n_{max}$.

2.3.3 Neutrinos

Neutrinos are particles that interact very weakly with baryons. Because of that, their collision term is null, and this is the main difference between the Boltzmann equations of neutrinos and photons. Then, using the definition $N(\eta, \vec{k}, \hat{p}) \equiv \frac{1}{4\rho_\nu} \int \frac{dpp^3}{2\pi^2} F_\nu$ (with $F_\nu \equiv \delta f_\nu$), equation (2.54) and doing the same calculus as for photons obtain:

$$N' + i\mu k(\Psi + N) + \Phi' = 0 \quad (2.66)$$

note that the above equation is essentially the same that in (2.61) but with τ null or neglected (once the interaction is very weakly, and neutrinos are decoupled from baryons). Following the same steps made for photons, we can deduce the infinite set of equations called hierarchy for the Neutrinos.

$$N'_0 + kN_1 = -\Phi' \quad (\text{Monopole } n = 0) \quad (2.67)$$

$$3N'_1 + k(2N_2 - N_0) = k\Psi \quad (\text{Dipole } n = 1) \quad (2.68)$$

$$(2n + 1)N'_n + k[(n + 1)N_{n+1} - nN_{n-1}] = 0 \quad (\text{Multipoles } n \geq 2) \quad (2.69)$$

2.3.4 Baryons

In cosmology, it is common to call the electrons (which are leptons) and protons as baryons. For they the main interactions is the Thomson scattering between the electrons and photons (2.55) and Coulomb scattering between protons and electrons

$$e^-(\vec{q}) + p(\vec{Q}) \longrightarrow e^-(\vec{q}') + p(\vec{Q}') \quad (2.70)$$

The electrons and protons are coupled such a way that we assume their density contrast perturbations being equal ($\delta_e = \delta_p \equiv \delta_b$), as well as their velocities perturbations ($\vec{v}_e = \vec{v}_p \equiv \vec{v}_b$). The equation for each are

$$\frac{dF_e(\eta, \vec{x}, \vec{q})}{d\eta} = \langle c_{ep} \rangle_{QQq'} + \langle c_{e\gamma} \rangle_{pp'q'} \quad (2.71)$$

$$\frac{dF_p(\eta, \vec{x}, \vec{Q})}{d\eta} = \langle c_{ep} \rangle_{qq'Q'} \quad (2.72)$$

where we neglect the interaction between protons and photons once this term would very small (its cross-sections decay with the mass of proton squared). Here we are using the useful notation of brackets to indicate the integral over the moments on subindex, that is $\langle \dots \rangle_{qq'Q'} = \int \int \int \frac{d^3\vec{q}}{(2\pi)^3} \frac{d^3\vec{q}'}{(2\pi)^3} \frac{d^3\vec{Q}'}{(2\pi)^3} (\dots)$. We can take the zero-moment of these equations (applying the $\langle \dots \rangle_q$ for electrons and $\langle \dots \rangle_Q$ for protons, which means, integrating over free momentum)

$$\delta'_e + kV_e + 3\Phi' = \langle c_{ep} \rangle_{qQQq'} + \langle c_{e\gamma} \rangle_{ppp'q'} \quad (2.73)$$

$$\delta'_p + kV_p + 3\Phi' = \langle c_{ep} \rangle_{Qqq'Q'} \quad (2.74)$$

Where it was used the equation (2.54) besides the $w_e = w_p = 0$ and $\delta P_e = \delta P_p = 0$. As there are no creation or annihilation of particles in these interactions all the collision contributions vanish, then summing the equations

$$\delta'_b + kV_b + 3\Phi' = 0 \quad (2.75)$$

it is the first equation that we can get for baryons. Taking the first moment of Boltzmann equations and summing them, we have

$$V'_b + HV_b - k\Psi = \frac{i\hat{k}_i}{\rho_b} \left(\langle (\vec{q} + \vec{Q})c_{ep} \rangle_{QQ'q'q} + \langle \vec{q}c_{e\gamma} \rangle_{pp'q'q} \right) \quad (2.76)$$

where $\rho_b \equiv \rho_e + \rho_p \approx \rho_p$ (mass of proton is very larger compared with electrons). The first term on the right side vanishes because of 3-momentum conservation, and just the second can contribute. This equation turns out

$$V'_b + HV_b - k\Psi = \frac{4\tau'\rho_\gamma}{3\rho_b}(V_b - 3\Theta_1) \quad (2.77)$$

2.3.5 Cold Dark Matter

As said before, CDM is non-relativistic particle (pressure is null) and with very weakly rate interacting. Because of that, the collision term of the right side of the Boltzmann equation is null. This simplifies so much the equations for CDM. As they have the same equation of state as baryons, the equations for CDM is simply

$$\delta'_c + kV_c + 3\Phi' = 0 \quad (2.78)$$

$$V'_c + HV_c - k\Psi = 0 \quad (2.79)$$

which is the same as (2.75) and (2.77) for $\tau = 0$ (no interaction between DM and other constitutes).

2.4 Baryonic Acoustic Oscillations

In the early universe, photons and baryons are coupled by Thomson and Coulomb scattering. As the baryons are not relativistic, their high rest energy (compared with its kinetic energy) makes them attract themselves and try to form gravitational wells. Despite that, at the same time, the photons create a positive pressure dragging them and destroying

any attempt to form gravitational wells. These dynamics create ripples on the plasma that propagate over it with a certain velocity. These sound waves are called Baryonic Acoustic Oscillations (BAO). In this section, we will see how these oscillations can arise from the equations deduced in the last sections, and show some approximations that allow us to visualize their behaviors and what happens with them after the recombination (when occurs the process of decoupling).

2.4.1 Temperature Fluctuations

As the reader already could have realized, solve analytically all the equations of the perturbations deduced last sections is impossible. Because of this, to obtain analytical results we need to make some approximations. In order to study the effects of coupling, we will work with the equations on the limit where $\tau \gg H$, which is called *Tight Coupling Limit* (TC). In that limit, the effects of multipoles $n \geq 2$ can be ignored, they are erased by the high rate of interaction (being more relevant after the decoupling). The useful parameter is the relation between photons and baryons density energy $R_s \equiv \frac{3\rho_b}{4\rho_\gamma} = \frac{3\Omega_{b0}}{4\Omega_{\gamma0}} a$. As the factor scale in this period is very small (compared with $a_0 = 1$), then the equation (2.77) can be approximated, in the TC limit as

$$V_b = 3\Theta_1 + \frac{R_s}{\tau'} (V_b' + HV_b - k\Psi) \approx 3\Theta_1 + \frac{R_s}{\tau'} (3\Theta_1' + 3H\Theta_1 - k\Psi) \quad (2.80)$$

at first order in R_s . This means that the velocity perturbations of baryons are created by the photon's dipole and vice-versa. Combining this result with the equations of (2.62) and (2.63) we have

$$\Theta_0'' + H \frac{R_s}{1 + R_s} \Theta_0' + \frac{k^2}{3(1 + R_s)} \Theta_0 = -k^2 \frac{\Psi}{3} - \Phi'' - H \frac{R_s}{1 + R_s} \Phi' \quad (2.81)$$

This is a wave equation (in Fourier space), where there is a forcing term on the right side (the gravitational potential acts as a source of sound waves), a damping term driven by the expansion of the universe (term proportional to Θ_0'). Note also that the velocity of the waves is given by $c_s^2 = \frac{1}{3(1+R_s)}$, there is, it depends on the relation between baryons and photons R_s . It's clear that the velocity of the waves decreases with the increasing baryons influence, which makes sense as this increases the effective inertia of fluid.

The above expression means that the monopole perturbations of radiation (temperature fluctuations) behave like ripples forced by attraction gravitational and damping by the expansion and that equation can be written in the form of an effective temperature

$$\left(\frac{d^2}{d\eta^2} + H \frac{R_s}{1 + R_s} + \frac{k^2}{3(1 + R_s)} \right) (\Theta_0 + \Phi) = \frac{k^2}{3} \left(\frac{\Phi}{1 + R_s} - \Psi \right) \quad (2.82)$$

It is possible find a solution for this equation, by WKB method, and the ansatz $(\Theta_0 + \Phi) = A(\eta)e^{iB(\eta,k)}$ [35] [36]. Then, the solution is

$$\Theta_0(\eta, k) + \Phi(\eta, k) = [\Theta_0(0, k) + \Phi(0, k)] \cos(kr_s(\eta)) \quad (2.83)$$

$$+ \frac{k}{\sqrt{3}} \int_0^\eta [\Phi(\eta') - \Psi(\eta')] \sin [k(r_s(\eta) - r_s(\eta'))] \quad (2.84)$$

Where $r_s(\eta) \equiv \int_0^\eta d\eta' c_s(\eta')$ is called *Sound Horizon*, and it means the comoving distance traveled by the sound waves until a time η .

2.4.2 Baryons Tight Coupling

Combining the equations (2.79) and the equation (2.62), we have

$$(3\Theta_0 - \delta_b)' + k(3\Theta_1 - V_b) = 0 \quad (2.85)$$

using the equation (2.80), we have

$$(\delta_b - 3\Theta_0)' = \frac{3R_s}{\tau'} \left(\Phi'' + \Theta_0'' + H(\Theta_0' + \Phi') + \frac{k^2\Psi}{3} \right) \quad (2.86)$$

Then, as R_s is small ($R_s < 1$ before the recombination and limit $\tau' \gg H$) we can approximate this expression, and obtain that δ_b and Θ_0 are apart by a constant. Further, adiabatic perturbations set initial conditions which ensure the proportionality between perturbation of baryons and photons (which is expected once they are in thermal equilibrium, that is, their energy density perturbations are related with the temperature perturbations). Finally, using $\delta_b \approx \Theta_0$ means baryons satisfy the same equation as photons.

$$\delta_b'' + H \frac{R_s}{1 + R_s} \delta_b' + \frac{k^2}{3(1 + R_s)} \delta_b = -k^2 \frac{\Psi}{3} - \Phi'' - H \frac{R_s}{1 + R_s} \Phi' \quad (2.87)$$

Then, the TC regime makes the photons drag the baryons owing to similar behavior. We can see, as a first approach, considering just the homogeneous solution as in (2.84) we have

$$\delta_b(\eta, k) \propto \cos(kr_s(\eta)) \quad (2.88)$$

Although this is an approximated solution, it can be used to give some intuition about the behavior of the baryon's fluctuations on configuration space (spacetime). The

solution above shows the k-mode, then to obtain an intuitive perception of what this means it is necessary to apply the inverse Fourier transformation. As it is a periodic function, we expect that mode has its maximum (excess of energy density) when

$$kr_s(\eta) = 2m\pi \quad (m = 0, 1, 2, \dots) \quad (2.89)$$

each of these k-modes is summed in the Fourier integration (each mode like $\cos(kr_s)e^{i\vec{k}\cdot\vec{x}}$) and they might amplify when spatial region is close to $r_s(\eta)$, this means, we would see a bump around $|\vec{x}| = r_s(\eta)$ (note that $r_s(\eta)$ was increasing with η). Then, if we denote η_* as the conformal time of recombination (when the decoupling started happening) we have that the maximum distance that the sound could be traveled would be $r_s(\eta_*)$. Because of this solution, we can say that the sound waves drag the baryons (forming the Baryonic Acoustic Oscillations) and they stopped (freeze out) in instants after close to recombination (see Fig. 5). Despite the most photons are free, the baryons are coupled with a small part of all photons yet (the ratio between baryon and photon density is about $\eta_B \equiv n_B/n_\gamma \approx 10^{-10}$, then we have so many photons for each electron [37]), thus they are dragged for a bit of time after the recombination. We called the moment when baryons finally are not more dragged by η_{drag} . That make the baryons gathering themselves in a specific scale, the sound horizon scale ($r_{drag} \equiv r_s(\eta_{drag})$).

2.4.3 Baryons After Decoupling

After the decoupling, photons are free to travel and baryons are not pushed anymore by the pressure of radiation. Then, now the Boltzmann equations for baryons are essentially the same as the CDM. Combining the equation (2.75) and (2.77) with $\tau = 0$

$$\delta_b'' + H\delta_b = -k^2\Psi - 3\Phi'' - 3H\Phi' \quad (2.90)$$

and an equivalent equation for CDM is allowed. we can approximate this equations and obtain the system

$$\begin{aligned} \delta_b'' + H\delta_b &= -k^2\Phi \\ \delta_c'' + H\delta_c &= -k^2\Phi \end{aligned} \quad (2.91)$$

Here we have used the equation (2.48). This equation means the gravitational potentials are different if there is spatial anisotropic stress. Since the pressure perturbations contribute to anisotropic stress, matter contributions can be neglected, and then, we

just would need concern about photons and neutrinos anisotropic stress. However, as we are dealing with equation during matter dominated universe we can neglected all the anisotropic stress, right after decoupling. When we do this, we get $\Phi = -\Psi$. Combining the Boltzmann and Einstein's equations it is possible to find out a time evolution equation for each mode of perturbations on metric (gravitational potential). From the solution of that equation, modes which enter during matter domination age suffer a declination over their amplitude about 10%, and after they remain constant along the time ($\Phi \approx \text{constant}$) [35]. As $H \propto \eta^{-1}$ at matter-dominated age, then the solution is

$$\delta_x(k, \eta) = C_x(k) + \frac{k^2 \eta^2}{6} \Phi(k) \quad (2.92)$$

where the index $x = b, c$ and $C_x(k)$ is independent of time. If consider adiabatic perturbation, the initial conditions means that $\delta_c = \delta_b$ and $C_c = C_b$. Then, the fluctuations on baryons, which were coupled with the photons, now grow with the CDM fluctuations, in other words, the baryons are falling in the potentials wells already created by the CDM (while the baryons were stuck with photons CDM could accumulate themselves). A more accurate description of perturbations (without these analytical approximations) can be seen in Fig. 5. That image shows how a single perturbation for each material species of the universe evolves (note it was considered a single perturbation on configuration space, in the real universe there would be various fluctuations like that in superposition). Note that even in the initial of the simulation the neutrinos appear decoupled because of their weak interaction. CDM also appears decoupled, but its small pressure makes them create a gravitational well instead of spreading out like neutrinos (first image of 5). At the same time, the baryons and photons travel together (Tight Coupling) represented by a bump with a certain velocity (similar to what was explained before 2.89). After the decoupling, we see that photons are free and baryon freezeout at a determined scale (this scale was measured by P18, and from Table 1 results about $r_{drag} \approx 147.21 \pm 0.23$ Mpc).

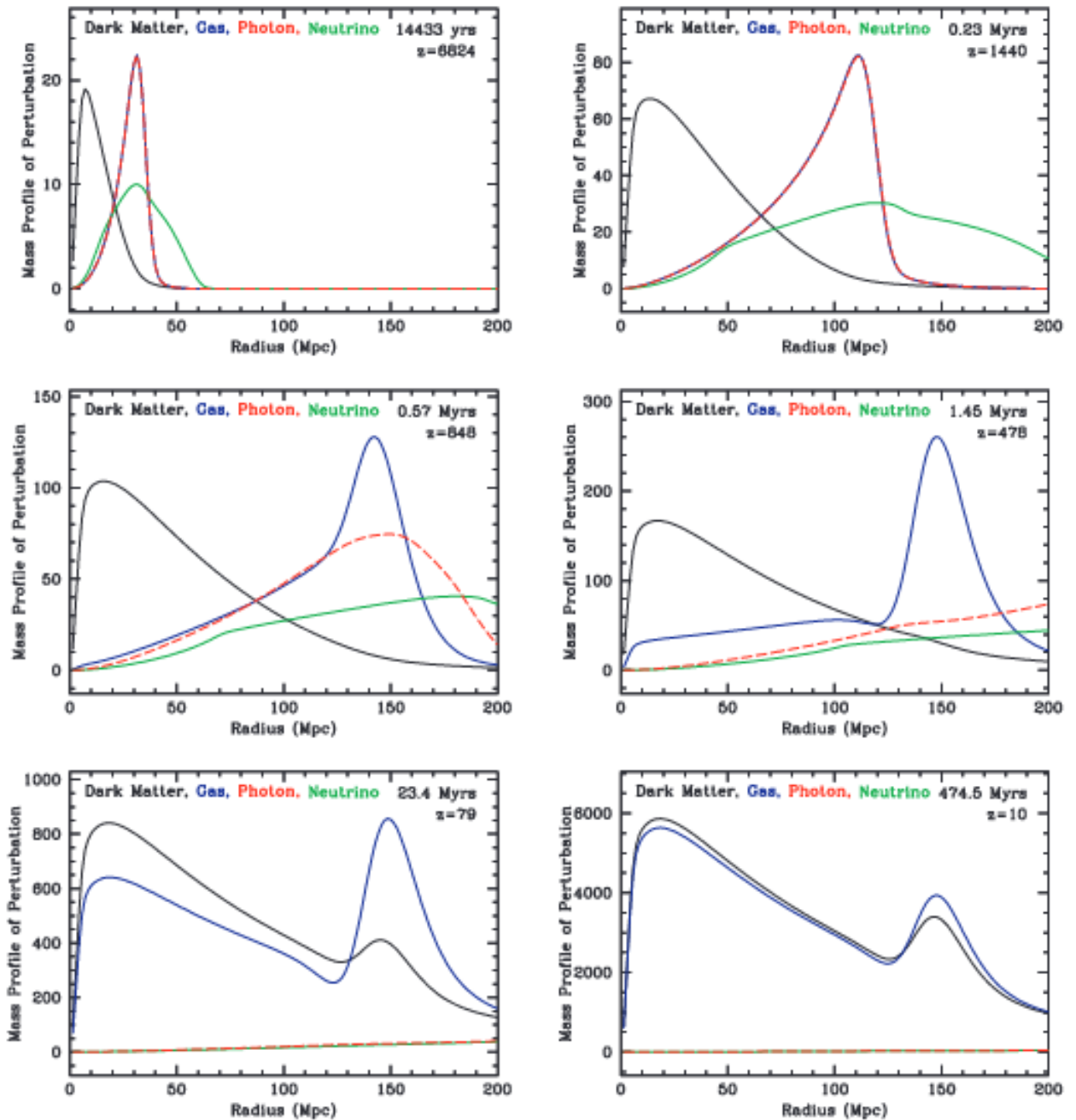


Figure 5 – Evolution of the radial mass profile along the comoving radius of an initially single overdensity located at the origin for CDM, baryons (called gas), photons, and neutrinos. The relativistic species were divided by a constant factor to be the same scale as other species [10]

Sometime after, it is shown that baryons start to adjust their distribution with CDM, because of the gravitational wells already created (baryons fall on it, as mentioned before). Here we see how much is important to consider dark matter non-relativistic, which means cold dark matter. If it was relativistic, then it could spread out as neutrinos did,

and the gravitational wells (essential to formation of large structures) would not be formed. The final picture of Fig. 5 shows that the fluctuation of CDM and baryons are very close, and they have a bump (smaller than that close after decoupling) that persists for a long time. Of course, this bump will affect the distribution of galaxies as we will see in the next chapters.

2.5 Stochastic Aspects on Cosmology

In the last chapter, we have discussed the likely quantum origin of the perturbations that evolve classically after inflation. Instead of determining the perturbations field for each position and time, as a deterministic system, it is more useful and informative to determine their statistical features. For example, if the initial conditions were raised and distributed by a Gaussian Field then they are characterized by their mean and standard deviation, which imprints specific signatures in the perturbations today (at least in large scales where the linear regime is valid yet). With this in mind, the initial conditions of perturbations are considered random variables that satisfy the equations shown in the last sections. In this section, we will see what kind of information we can extract from these stochastic features associated with fluctuations. We can think in the universe as a huge statistical system, and despite there is only one realization of the universe we can do some statistical analysis adopting a strategy based on a powerful theorem. That theorem allows us to exchange the ensemble averages with spatial averages if the volume goes to infinity. In practice, the volumes are finite, and then we need to take different regions of the sky distant enough to themselves and consider each as an independent realization of the universe observed (which means that the confidence of this process decrease as we consider averages with large scales). This theorem is called *Ergodic Theorem* [35]. Then, hereafter we will consider an average, denoted by $\langle \dots \rangle$, as a spatial average:

$$\langle \dots \rangle = \frac{1}{V} \int \dots d^3x \quad (2.93)$$

2.5.1 Power Spectrum and Spatial Correlation

An important piece of information that we can extract from the perturbation is their correlation between different scales. Consider a perturbation mode $\delta(\vec{k})$, then

$$\langle \delta(\eta, \mathbf{k}) \delta^*(\eta, \mathbf{k}') \rangle = \int d^3x \int d^3x' \langle \delta(\eta, \mathbf{x}) \delta(\eta, \mathbf{x}') \rangle e^{-i\mathbf{k}\cdot\mathbf{x}} e^{i\mathbf{k}'\cdot\mathbf{x}'} \quad (2.94)$$

which is just the Fourier transformation of correlation of fluctuations in space. As they are fluctuations, by definition the simple average $\langle \delta(\eta, \mathbf{x}) \rangle = 0$. Then if the

perturbation on different point are independents $\langle \delta(\eta, \mathbf{x})\delta(\eta, \mathbf{x}') \rangle = \langle \delta(\eta, \mathbf{x}) \rangle \langle \delta(\eta, \mathbf{x}') \rangle = 0$, that means no correlation between them exist (This is the idea in considered distant volumes as independent regions, because the correlation between two points goes to zero as the distance tends to infinity). Going back to the above expression, we can denote the *Spatial Correlation Function* (SCF) as a function just of distance between the spatial points ($\langle \delta(\eta, \mathbf{x})\delta(\eta, \mathbf{x}') \rangle = \xi_\delta(\eta, |\mathbf{x} - \mathbf{x}'|)$), once we are considering a universe with random fields homogeneous and isotropic (The universe must shown the same statistical features from wherever it is observed).

$$\langle \delta(\eta, \mathbf{k})\delta^*(\eta, \mathbf{k}') \rangle = (2\pi)^3 \delta^3(\mathbf{k} - \mathbf{k}') P_\delta(\eta, \mathbf{k}) \quad (2.95)$$

Here we have defined the *Power Spectrum*

$$P_{\eta, \delta}(\mathbf{k}) = \int d^3\mathbf{r} \xi_\delta(r) e^{-\mathbf{k}\cdot\mathbf{r}} = 4\pi \int_0^\infty \left(\frac{\sin(kr)}{rk} \right) \xi_\delta(r) r^2 dr \quad (2.96)$$

where $\mathbf{r} = \mathbf{x} - \mathbf{x}'$. As this is just a Fourier Transformation, it allows the inverse relation

$$\xi_\delta(\eta, r) = \int \frac{dk}{k} \Delta_\delta^2(\eta, k) \frac{\sin(kr)}{kr} \quad (2.97)$$

where $\Delta_\delta^2(\eta, k) \equiv \frac{k^3 P_\delta(\eta, k)}{2\pi^2}$ is the dimensionless power spectrum. At the beginning of the universe, as we said, there are initial conditions given by a random process, and as each perturbation mode is entering into the horizon they undergo by modification because of the evolution of the universe. Then, it is useful to separate the spectrum as

$$P_\delta(\eta, k) = T^2(\eta, k) P_\delta(k) \quad (2.98)$$

where $T(\eta, k)$ is called *Transfer Function* and $P_\delta(k)$ is the initial power spectrum (also called primordial power spectrum) for which is allowed the expression like (2.95), just exchanging $\delta(\eta, \mathbf{k}) \rightarrow \delta_p(\mathbf{k})$ (the later is the initial conditions to fluctuations). The transfer function behaves like a propagator of the initial spectrum over time, and so, it is deduced from the solutions of Einstein and Boltzmann's equations shown before [38]. The primordial spectrum is provided by inflationary models, which can relate the matter power spectrum with potential power spectrum [25].

2.5.2 Probabilistic Intuition of Spatial Correlation Function

We can probe gravitational effects (like the preferable scale left by the BAO) over the matter distribution considering initially two volumes V_1 and V_2 and each contains a mean number of the galaxy given by $\bar{\rho}_1$ and $\bar{\rho}_2$, respectively. We are talking about galaxies because they emit light and are more easily observed than all matter. Then, if the gravitation effects between these two volumes can be ignored, the probability of taking one galaxy in each volume is proportional to $\bar{\rho}_1 dV_1$ and $\bar{\rho}_2 dV_2$, respectively (where dV_1 and dV_2 has size enough to contains just one galaxy). Then, the probability of take two galaxies localized in \vec{x}_1 and \vec{x}_2 , into the volumes V_1 and V_2 , respectively, is given by $dP_{12} = \bar{\rho}_1 \bar{\rho}_2 dV_1 dV_2$. When the $\bar{\rho}_1 = \bar{\rho}_2 \equiv \bar{\rho}$ we say that the positions of galaxies were generated by the same random process but independently, then it follows a *Poisson Distribution* (probability of n successes of independent point-like events). As gravity makes the galaxies interact each other their positions are not completely independence anymore. Thus the number density is a function of spacetime and the probability of taking two galaxies, simultaneity, in positions \vec{x}_1 and \vec{x}_2 in theirs respectively volumes are

$$dP_{12} = \rho(\vec{x}_1)\rho(\vec{x}_2)dV_1dV_2 \quad (2.99)$$

Actually, it is necessary to take the average of this value to obtain some reliable estimate, otherwise, we would carry information about just one realization (statistically poor). That can be done by calculating the quantity for a large number of independent samples and take the average between them (sample average) or calculate this quantity for each pair of galaxies separated by this distance and take the average between them (spatial average). As the volume of the sample increase these two methods converge to the same results. Taking the average of expression (2.99) and writing the mean number density as $\rho = \bar{\rho}(1 + \delta(\vec{x}))$, then

$$dP_{12} = \langle \rho(\vec{x}_1)\rho(\vec{x}_2) \rangle dV_1dV_2 = \bar{\rho}^2(1 + \langle \delta(\vec{x}_1)\delta(\vec{x}_2) \rangle)dV_1dV_2 \quad (2.100)$$

The term $\langle \delta(\vec{x}_1)\delta(\vec{x}_2) \rangle = \xi(\vec{x}_1, \vec{x}_2)$ is recognize as the excess of probability of there are two galaxies separated by a vector $\vec{x}_2 - \vec{x}_1 \equiv \vec{r}$ when compared with Possion Distribution, which gives a more clear intuition about the spatial correlation function seen in (2.97). It is important to highlight that the print of the sound horizon is over the matter distribution, but the galaxies (used as an example here) is just a fraction of the matter in the universe (most part is the Dark Matter). This fact inserts a bias when we observe just galaxy distribution, which in general can be written as $\delta_g = b(z)\delta_m$, where $b(z)$ is likely a function of redshift. However, that bias is approximately constant.

3 DATA ANALYSIS

In this chapter, we will focus in explain how we can extract information about Angular Correlation Function (ACF) from a galaxy catalog. In the section 3.1 there is a summarized descriptions of the data used in the analysis. The section 3.2 introduces the concept of ACF. In the section 3.3 is shown how we can calculate the ACF given the data set described at the last sections. The section 3.4 is about how we have estimated the covariance matrix from Mock catalogs and 3.5 shown how was made the detection of BAO signals.

3.1 Data Description

The SDSS (Sloan Digital Sky Survey) is an international scientific collaboration that has created the most detailed three-dimensional maps of the Universe. This project is divided into 4 phases, SDSS-I (2000-2005), SDSS-II (2005-2008), SDSS-III (2008-2014), and SDSS-IV (2014-2020). This work deal with data from SDSS-III [39] and SDSS-IV [40]. In these two last phases, there are data set known as *Baryon Oscillation Spectroscopic Survey* (BOSS) [41] and *extended Baryon Oscillation Spectroscopic Survey* (eBOSS) [42], respectively. This work uses the last *Data Release* (DR) of BOSS and eBOSS called respectively DR12 and DR16.

- **DR12 :**

DR12 maps the spatial distribution of luminous red galaxies (LRGs) and quasars [14]. This data set is divided into two main catalogs (North and South). The north's catalog is denser and covers a redshift until $z \approx 1.0$, totalizing approximately 953 thousand galaxies included. The south's catalog, with the same range of redshift, counts about 373 thousand galaxies.

- **DR16 :**

DR16 maps the spatial distribution of LRGs and emission-line galaxies (ELGs) [43]. Despite the DR12 include galaxies in the redshifts $z > 0.6$ the density of catalogs in this region is very smaller when compared to density in the region of $0.45 \lesssim z \lesssim 0.6$ (region with a higher density of galaxies). the DR16 increases the number of galaxies observed in the range $0.6 < z < 1.0$. Including a sub-sample of DR12 in their LRG's catalogs, it counts about 256 thousand (North) and 122 thousand (South) galaxies. The ELG's catalogs count about 84 thousand (North) and 90 thousand (South) targets.

As can be seen in the Fig. 6, the catalogs from the South appear a density very lower compared to the North. Because of that, in our analysis, we consider just the North Catalogs.

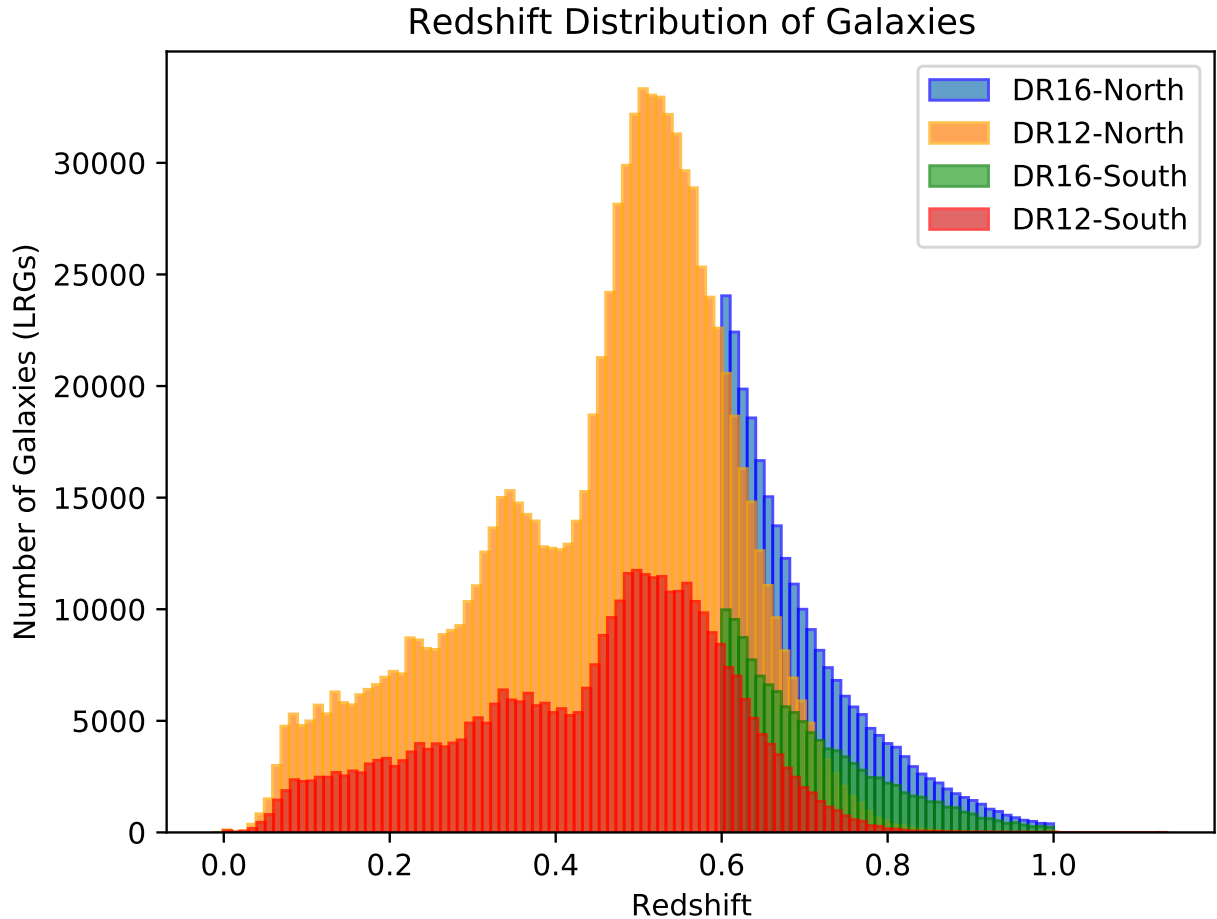


Figure 6 – LRG's redshift distribution of DR12 and DR16 for two regions (North and South) of the sky (the bin used to built this histogram is $\delta z = 0.01$).

Important to highlight here, the ACF was measured up to redshift $z = 0.6$ using North from DR12 and from this point and forward was used only DR16 (we do not combine the observed galaxies of these two data set because DR16 already own galaxies observed on DR12). Further, we just use LRGs in analysis which were more extensively observed, offering more data.

3.2 Angular Correlation Function

A straightforward way to measure the $\xi(r)$ (2.100) is to count all galaxy pairs in the catalog that are separated by distance r , but to do this it is necessary to assume some

cosmological model to calculate the distances between galaxy's pairs. To avoid that, we can use the *Angular Correlation Function* (ACF). The idea is the same as the spatial correlation function, but we fix some effective redshift and count the pairs separated by some angular difference (Fig. 3.1). The angular correlation function $w(\theta)$ indicates the excess of the probability that galaxies to be separated by a certain angle θ compared to what they would be if they are randomly distributed.

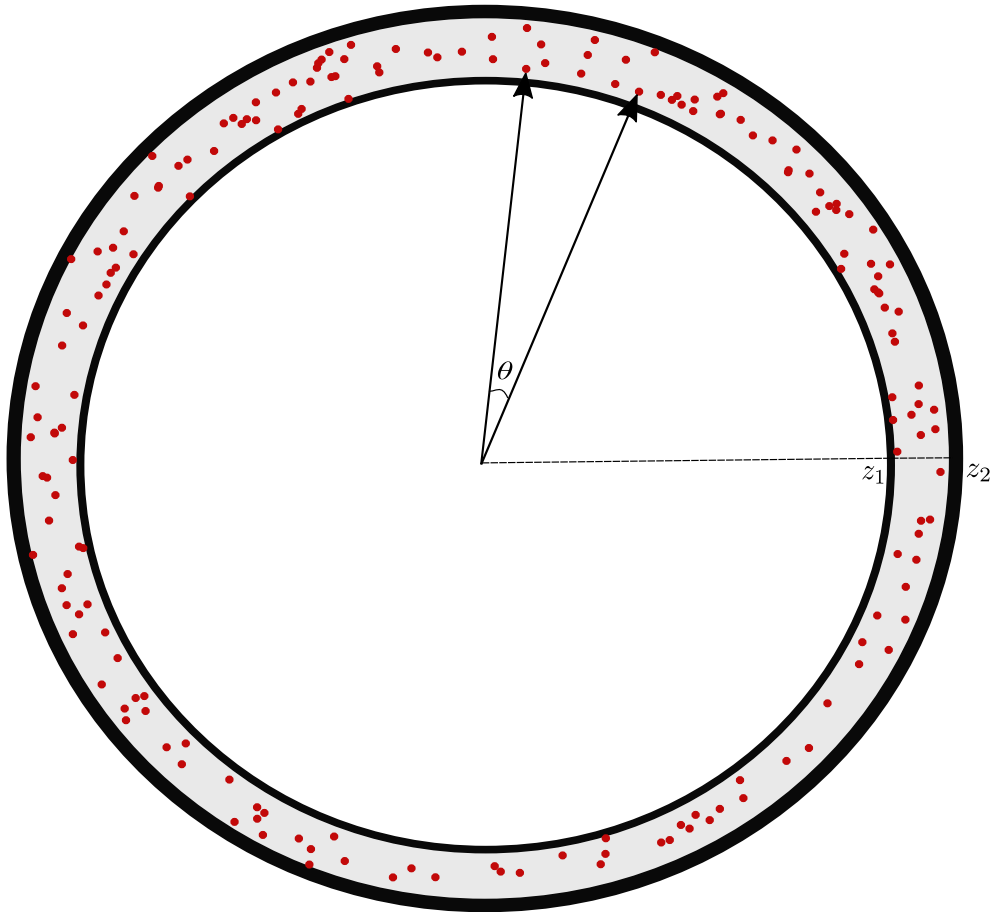


Figure 7 – Representation of angular separation between galaxies into the shell

Illustration of a general redshift shell that contain several galaxies (red dots). The shell own internal and external radius z_1 and z_2 , respectively. We also denote $z_{eff} = \frac{z_1+z_2}{2}$, and $\delta z = z_2 - z_1$.

To calculate the angular distances, we use the equatorial coordinate system with origin at the center of the Earth. The angular positions are defined by the angles called *Declination* (latitude) that vary from -90° to 90° (degrees of arc) and *Right Ascension* (Longitude) that vary from 0° to 360° , see Fig. 8. Therefore, assuming the galaxies into the shell has the same redshift (what is an approximation), the distance between two galaxies is just proportional to their angular distance calculated as [44]

$$\gamma(\theta_1, \theta_2) = \arccos \left(\sin(D_1) \sin(D_2) + \cos(D_1) \cos(D_2) \cos(R_1 - R_2) \right) \quad (3.1)$$

where D_i and R_i indicates the angular coordinates (declination and right ascension, that is $\theta_1 = (R_1, D_1)$ and $\theta_2 = (R_2, D_2)$) for i -th galaxy. Then, using just spherical trigonometry we can calculate the angular distance between the galaxies and count the number of pairs for each angular separation.

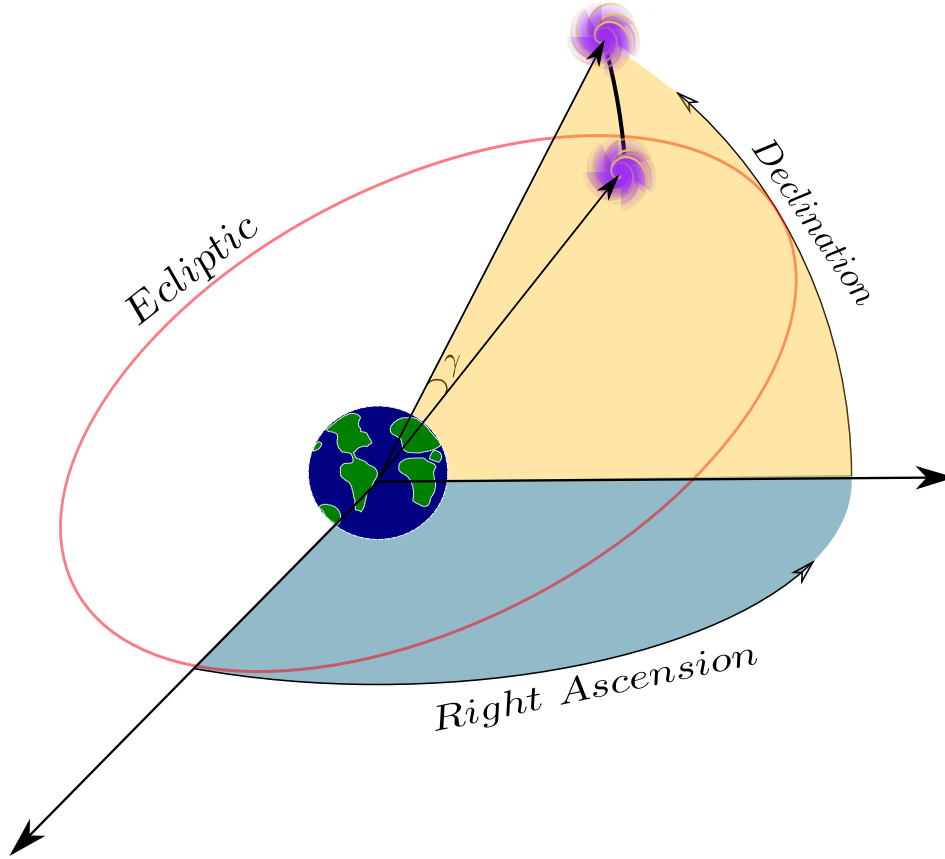


Figure 8 – Equatorial coordinate system and representation of angular position of two objects over celestial sphere.

3.2.1 Estimator for Angular Correlation Function

To extract the angular scale of BAO directly from the data (without using a cosmological model) we need to define an estimator to the ACF and how to calculate it. Once chosen a shell and its width, we count, for each possible value of angle θ , the number of pair of galaxies using the function below

$$P(\theta) = \sum_{\theta_1} \sum_{\theta_2} \phi_{\theta}(\theta_1, \theta_2) \quad (3.2)$$

$$\phi_{\theta} = \begin{cases} 1, & \theta < \gamma(\theta_1, \theta_2) < \theta + \delta\theta \\ 0, & \text{whatever else} \end{cases} \quad (3.3)$$

where γ is the angular separation calculated by the formula (3.1). The idea is to compare the count of pairs from a real catalog and a catalog created by the random process. The catalogs can have different sizes (number of galaxies), then a fair comparison just could be made if we normalize the counts. Further, we use the notation D (data) and R (random) to the count from the real and random catalogs, respectively. The count of pairs normalized is shown below.

$$DD(\theta) = \frac{P_D(\theta)}{N_D(N_D - 1)} \quad (3.4)$$

$$RR(\theta) = \frac{P_R(\theta)}{N_R(N_R - 1)} \quad (3.5)$$

Where N_D and N_R mean the total number of galaxies in the catalogs real (data) and random, respectively. The most natural estimator for the angular function is the fractional difference between the real and random distribution

$$W_N(\theta) = \frac{DD - RR}{RR} = \frac{DD}{RR} - 1 \quad (3.6)$$

This is known as a natural estimator and was proposed by Peebles [45]. Actually, there are many other estimators proposed and the most used estimator is

$$W_{LS}(\theta) = \frac{DD - 2DR + RR}{RR} \quad (3.7)$$

That estimator, proposed by Landy and Szalay, provides a smaller variance in comparison to the others [46]. Here the DR is the normalization count of cross-pairs between real and random catalogs (cross-relation between the catalogs) .

$$P_{DR}(\theta) = \sum_{\theta_1 \in D} \sum_{\theta_2 \in R} \phi_\theta(\theta_1, \theta_2) \quad (3.8)$$

Once the estimator is defined, it would be enough to estimate the BAO angular scale from catalogs, but there are some details about how to do this that need to be discussed yet.

3.3 Counting Pairs of Galaxies

It is important to understand some issues about released catalogs by BOSS and eBOSS. Each galaxy has the angular positions (RA and DEC), radial position (redshift) and statistical weights (and some other features that are not important for our analysis) available on the catalogs.

3.3.1 Weights

The experiments do not observe the galaxies perfectly. Besides systematic effects, some other effects can change the counting of galaxies in some regions of the sky. For example, the sensors of telescopes can not detect some galaxies in the sky (the signal is probably missed) or can offer a not reliable redshift measure (redshift failure). Another effect that could occur is called "fiber collision", which means that galaxies with angular separation less than some value (62 arcsec [47]) can not be measured separately as two different targets. To deal with these effects are defined some statistical weights for each galaxy. Then, instead of count the galaxies as one (there is one galaxy) or zero (there is no galaxy) the count associate for each galaxy the combination of these weights [48]

$$w = w_{FKP} w_{sys} (w_{rf} + w_{cp} - 1) \quad (3.9)$$

where w_{rf} and w_{cp} are weights to correct *Redshift Failure* and *Close-Pairs* (also called fiber collision), respectively. The $w_{sys} = w_{star} w_{see}$ is the weight associated with systematic effects, divided in two w_{star} to correct the correlation between stellar density and galaxy counting (stars can change the counting of the real number of galaxies seen, mainly where stellar density is relatively greater), and in w_{see} which is responsible to correct the impact of poor seeing conditions on the observed galaxy number density [47]. Another important weight insert in this expression is the w_{FKP} . This weight is responsible to deal with shot-noise and cosmic variance optimizing the clustering measurement defined as shown in [49]. The next subsection concerns to explain, in details, how all these weights enter the pairs counting necessary to estimate the ACF. Considering it, below is shown an example of it with and without w_{FKP} weight. It can be observed (figure 9) that even the effect of using this weight being subtle, the variance is less sensitive to noise of the data.

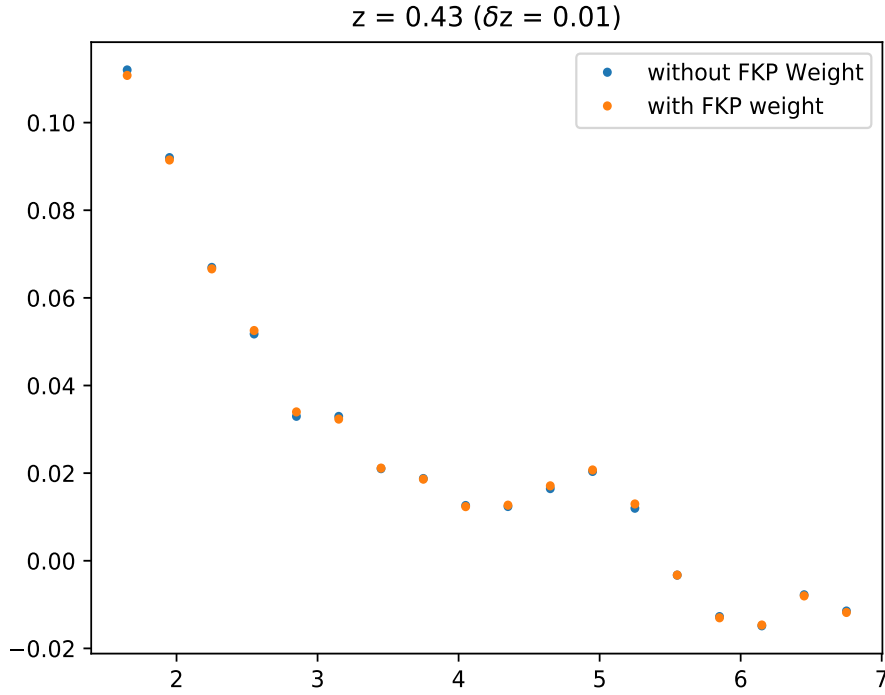


Figure 9 – Example of estimating ACF with and without w_{FKP} .

3.3.2 DD, RR and DR

Considering now the corrections given by the statistical weights shown before, The counting function (3.3) for DD , RR and DR needs to be modified. Then, it is now defined as

$$\phi_{\theta}(\theta_i, \theta_j) = \begin{cases} w_i w_j & \theta < \gamma(\theta_i, \theta_j) < \theta + \delta\theta \\ 0, & \text{whatever else} \end{cases} \quad (3.10)$$

Where w_i and w_j are the total weights associated with the i -th and j -th galaxies, respectively. Note, when w_i and w_j are equal to 1 we obtain the special case of (3.3).

To rewrite DD and RR considering the statistical weights we define the matrix Wp , such that, the Wp_{ik} element contain the number of pairs between the i -th galaxy and other galaxies whose angular separation is between the θ_k and $\theta_k + \delta\theta$ (for some $\delta\theta$ that will define the resolution of the count 3.5), that means

$$Wp_{ik} = \sum_{j>i} \phi_{\theta_k}(\theta_i, \theta_j) = w_i \left(\sum_{j>i} w_j \right) \text{ for } \gamma_{ij} \in I_k \quad (3.11)$$

where in the last equality, the sum over j runs just for galaxies that form pairs with i -th galaxy within the angular interval $[\theta_k, \theta_k + \delta\theta] \equiv I_k$ ($j > i$ to avoid repeating terms). Since the $DD(\theta)$ and $RR(\theta)$ means the normalized total counting of pairs separated by each value of θ . Then, to obtain this quantity just sum each line of Wp and normalize. The DD without normalization is

$$DD(\theta_k) = \sum_i Wp_{ik} = \sum_i w_i \left(\sum_{j>i} w_j \right) \text{ for } \gamma_{ij} \in I_k \quad (3.12)$$

The normalization is not difficult to calculate. It can be calculated summing the pair of catalog in all angular scales, which result in the normalization constant $N = \sum_l w_l \sum_{m>l} w_m = \frac{(\sum_l w_l)^2 - \sum_l w_l^2}{2}$, where l index runs over all galaxies of the catalog. Then, the DD counting with normalization gives

$$DD(\theta_k) \equiv 2 \frac{\sum_i w_i \left(\sum_{j>i} w_j \right)}{(\sum_l w_l)^2 - \sum_l w_l^2} \text{ for } \gamma_{ij} \in I_k \quad (3.13)$$

Again, the calculus for RR is the same, considering just galaxies from the random catalog.

$$RR(\theta_k) \equiv 2 \frac{\sum_i w_i \left(\sum_{j>i} w_j \right)}{(\sum_l w_l)^2 - \sum_l w_l^2} \text{ for } \gamma_{ij} \in I_k \quad (3.14)$$

Although ifromis not the same, the DR calculus has many similarities with DD and RR . For the cross-count, it is not necessary to worry about repeat pairs, because we count pairs formed by galaxies from real data with those from random catalogs, then the index of equation (3.11) runs over different sets of galaxies. For DR that equation change as

$$Wp_{ik} = w_i \left(\sum_j w_j \right) \text{ for } \gamma_{ij} \in I_k \quad (3.15)$$

where w_i is the weight of i -th galaxy from the real catalog and w_j is the j -th weight of the random catalog. The angular separation is $\gamma_{ij} = \gamma(\theta_i, \theta_j)$ such that θ_i and θ_j are the angular positions of i -th and j -th galaxies from different catalogs, respectively. With the same idea as before, the non-normalization count gives

$$DR(\theta_k) = \sum_i w_i \left(\sum_j w_j \right) \text{ for } \gamma_{ij} \in I_k \quad (3.16)$$

The normalization is simply $N = \sum_l w_l \sum_m w_m$ (note that l and m runs over all catalog), and the normalization counting of DR gives

$$DR(\theta_k) = \frac{\sum_{i,j} w_i w_j}{\sum_{l,m} w_l w_m} \text{ for } \gamma_{ij} \in I_k \quad (3.17)$$

Once calculated DD , RR and DR for the shell we can estimate the ACF for each θ_k of interest

$$W(\theta_k) = \frac{DD(\theta_k) - 2DR(\theta_k) + RR(\theta_k)}{RR(\theta_k)} \quad (3.18)$$

3.4 Mocks and Covariance Estimation

To know the error bars of ACF we need to estimate the covariance matrix. It would be necessary to measure the ACF many times to estimate the covariance from data, but to obtain a more statistical robust estimation we use *Mock Catalogs*. These catalogs are simulations of real catalogs and consider not just the theoretical physics to simulate the distribution of galaxies on large scale but also consider the simulation of features from the process of measuring to make it more realistic. The process to estimate the covariance from Mock is straightforward, we calculate the ACF (as described in the section 3.3) for many different mock catalogs and take the covariance between them like

$$COV(\theta_i, \theta_j) = \frac{1}{N-1} \sum_k (W_k(\theta_i) - \bar{W}(\theta_i))(W_k(\theta_j) - \bar{W}(\theta_j)) \quad (3.19)$$

Where W_k is the ACF of k -th Mock Catalog and \bar{W} is the average of ACF over all of them. For our analysis, we use 1000 Mock Catalogs ($N = 1000$) that simulate real catalogs and just one random catalog (which is about 50 or 20 times larger than the Mock-real simulation). For example, to compare with the distribution of Fig. 6 we show the distribution for one Mock:

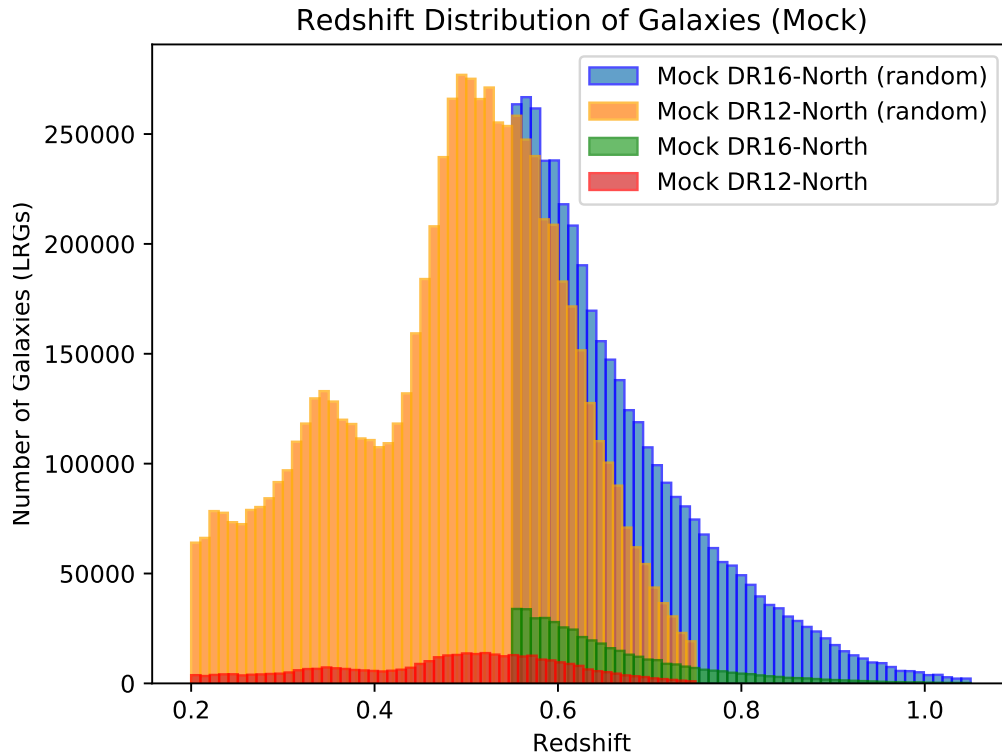


Figure 10 – Here is shown the redshift distribution of a general Mock Catalog. The Mock-random catalog in the figure is 20 times larger than Mock-real. Note that the shape of Mocks catalog is preserved in the simulation.

In order to produce the Mock catalogs, it is necessary to assume a cosmological model. This creates a bias over the covariance matrix. However, the covariance enters in the analysis as the errors and correlations between the measurements, in other words, this bias inserts an uncertainty over the covariances, second order of relevance, being irrelevant in the face to other sources of uncertainties that come from the data itself.

3.5 The BAO Signal

As already mentioned, the count of pairs runs over the galaxies contained by the redshift shell, in other words, we need to slice the catalog in several spherical shells. As the measurement of angular correlation comes from these counts, the estimates should improve if increase the number of galaxies, which suggests we to take thicker shells and collect more galaxies. Although, to take thicker of the shells creates a bias over the BAO signal as we will see.

3.5.1 Radial Projection and Angular Bins

The BAO scale indicates the distance in which the distribution of galaxies has an excess probability when compared with the Poisson distribution. The angular correlation function depends just on the difference of angle positions (calculated by 3.1) because assumes that the radial difference is zero, and then it just measures the transversal (about our line of sight) signal of BAO. However, in the catalog data, the redshift of galaxies is never the same, as shown in the figure 11.

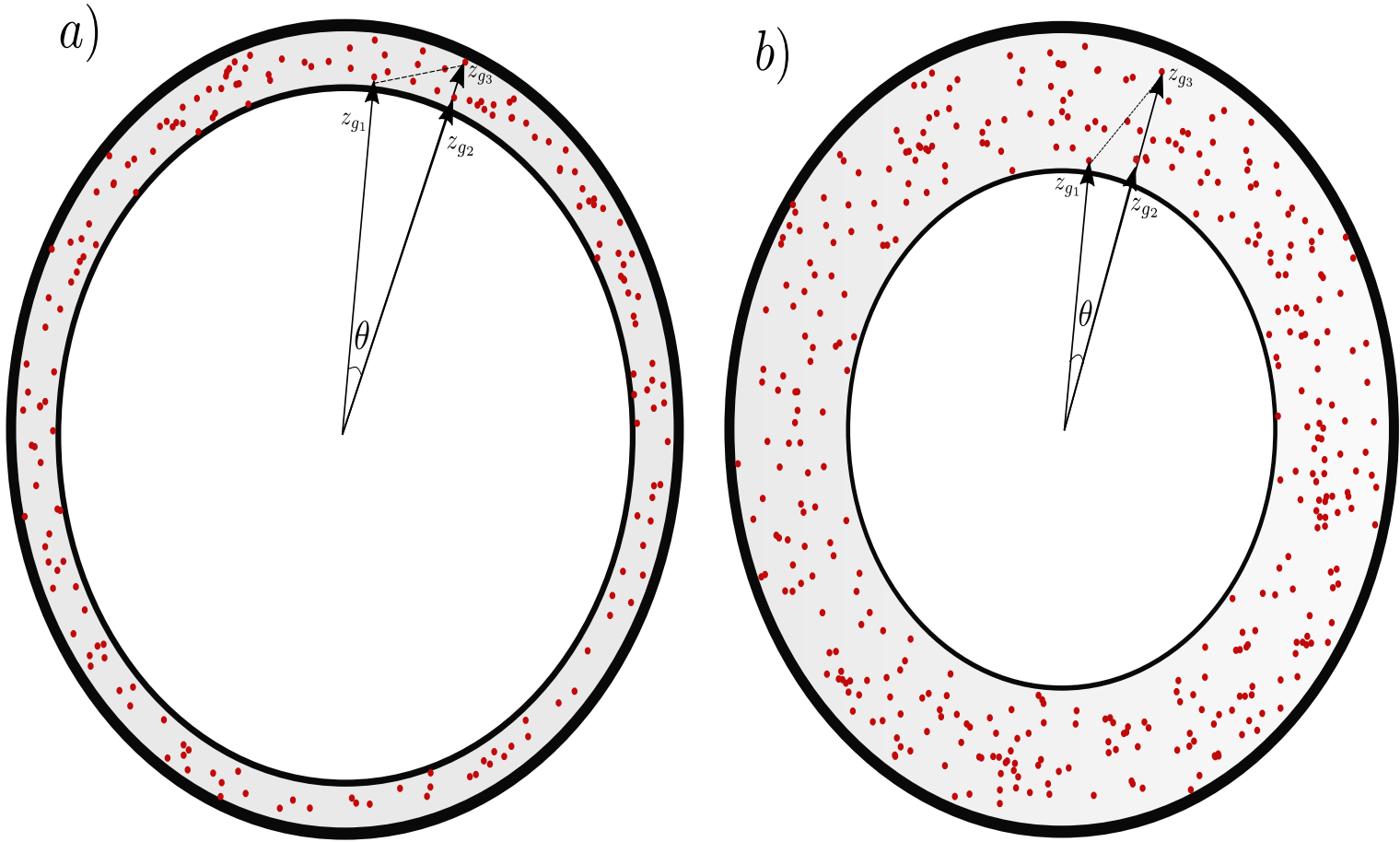


Figure 11 – Representation of shells with different width of redshift

The images show a schematic illustration of the radial difference between any pairs of galaxies (red dots) for two shells with the same effective redshift (they have the same density mean) but with different widths. Image (a): the shell is tiny, then the average redshift difference between the galaxy is small. Image (b): the width shell is thicker, then it can contain galaxies with a large difference in the redshift. We see that angular separation between the g_1 and g_2 is almost the same as g_1 and g_3 , but the physical distance is not the same, and the average of this difference is larger as increase the width.

When is used the formula (3.1) we are projecting the position of all galaxies contained by the thickness of the shell in the same effective radius (redshift), and so the radial distribution causes some interference in the detection of angular BAO signal. Because of that, the transversal BAO signal is diluted (mixed) with the radial signal, that

can decrease and displace the peak to smaller angles when calculating the ACF with (3.18). Concerning that, we could choose a width smaller (avoiding the radial signal) but this means decreasing the number of galaxies, and the statistical robustness. So, it is necessary to find a balance between minimizing the radial effects and obtaining a relevant bump (signal) in the ACF (see Fig. 12).

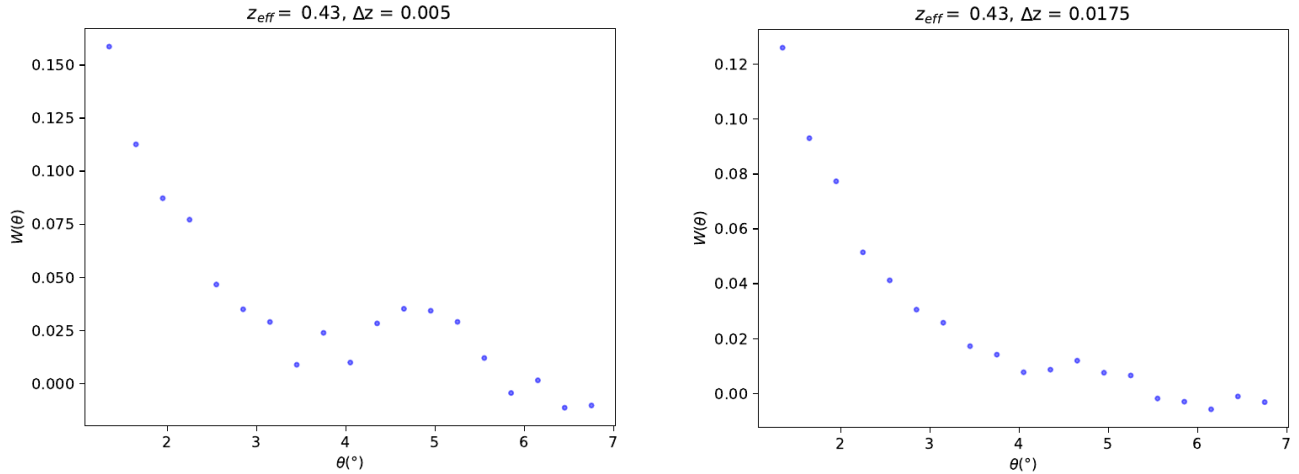


Figure 12 – The angular correlation function measured for two shells with the same radius ($z_{eff} = 0.43$) but with different width (δz). Even with more galaxies, it is evident the attenuation of the peak for the thicker shell because of the radial projections.

Another issue necessary to deal with is the angular bins $\Delta\theta$ that we need to choose to estimate the ACF. This choice is relevant because if the angular bin is very large it can lose information and not detect the peak of BAO. On the other hand, if the angular bin is very small, the measurement would be sensible to any count fluctuations (much noise) and more galaxies are necessary to detect a relevant signal of BAO. The redshift of the galaxies does not cross the $z = 1.0$, then the angular scale for BAO that we hope to measure is about $\theta = [1.5^{\circ}, 7^{\circ}]$ (angular scales larger than 7° are expected for redshift smaller than 0.3, where the density of BOSS's catalogs is very low). As shown in the paper [5], the best results (which shown relevant peak compared to the noise) come from the choices for angular separation about $\Delta\theta \approx 0.38, 0.32, 0.3$. It shows that the bins larger appear the peak of BAO more diluted compared. Our work use $\Delta\theta = 0.3$ as the standard value for the angular bins (the value $\Delta\theta = 0.2$ was also tested but appears a lot of noise).

3.5.2 Detecting the Signal

If the galaxies were distributed randomly, we expect a Poisson Distribution [35], and then the numbers of pairs separated by angle θ would decrease as their separation increase, following a power law [11]. Because the matter shows a preferable scale where it accumulates (sound horizon) we expect to see that as a bump in the ACF. We can estimate the transverse angular distance of the specific scale with the parametrization for ACF given by [11]

$$W(\theta) = A + B\theta^\nu + Ce^{-\frac{(\theta-\theta_{FIT})^2}{2\sigma^2}} \quad (3.20)$$

where the power law captures the Poisson distribution behavior and the Gaussian bump that appears disturbing the first. The physical relevant parameter here is the θ_{FIT} that marks the angular scale of the sound horizon. To obtain a robust result about constraints of the measurement, we explore the parameter space with EMCEE [12], an open-source sampler for Markov chain Monte Carlo (MCMC), and use GETDIST [13] in the analysis of the chains, obtaining the confidence intervals. During in the in the test stage of this work others phenomenological models were compared. All of them are variations of (3.20), for example adding exponential terms, that increase the numbers of parameters. Although they own more parameters the efficiency of the fit was, in general, not better than the model above (looking to Chi-squared reduced χ_r^2). Then, we use in the real analysis just the phenomenological model (3.20) which result equivalent fit precision with less parameters when compared with its variants.

Important to note that this is not the final result for the angular peak of BAO. Since we infer the peak from ACF measured from a shell with finite width, it suffers an apparent displacement because of the radial effects explained before. To deal with this bias is necessary to deduce a way to correct that displacement.

3.5.3 Correction of the θ_{FIT}

As the redshift width is increased, the transverse signal of the BAO (the target in this work) is mixed with the radial signal. This effect decrease for thinner shells. Then, we can hope that the θ_{FIT} would be equal to the real peak of BAO, denoted as θ_{BAO} , if the thickness is approximate to zero. In this work, a method to estimate a correction for the θ_{FIT} and estimate the real θ_{BAO} was developed. Assuming it is known the functional form of $\theta(\delta z)$ (just for very small values of δz), we can define the relative difference between the peak measured from a shell with width $\delta z \neq 0$ and the $\delta z = 0$.

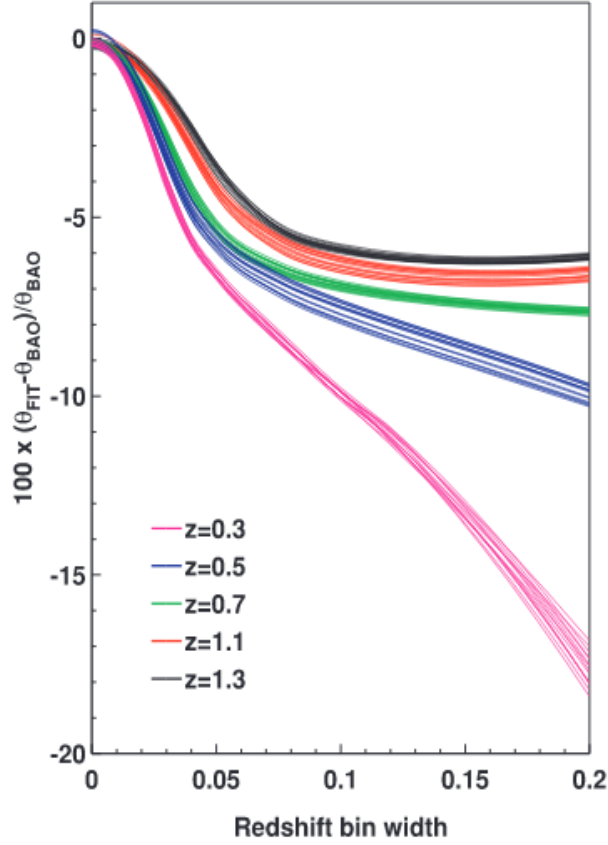
$$\alpha(\delta z) = \frac{\theta_0 - \theta(\delta z)}{\theta_0} \quad (3.21)$$

Where $\theta_0 = \theta(\delta z)|_{z=0}$. We are denoting the functional form just by $\theta(\delta z)$, while the measurement from the shells are by $\theta_{FIT}(\delta z)$. Then, the goal is to estimate the behavior of θ to fit the correction α (which will be used to correct the best θ_{FIT} for each effective redshift later).

As shown in the paper [11], this correction factor (which was calculated by simulating many different cosmological models) increases with the width of the shell (Figure 13) and there are two features about the behavior of this factor. The first one, it appears does not depend so much of the cosmological model for tiny shells. The second feature is about the shape of the curve, which does not depend on the redshift. The apparent displacement increase with δz (as it was expected) from a minimum local (as see in 13), then we can expand the function α , as well as the model for $\theta(\delta z)$, in a Taylor series until second order of δz . We work in the region close to a stationary point of the function (the regime we are using in the analysis $\delta z \leq 0.02$). Therefore we model it as

$$\theta(\delta z) = \theta_0 + B\delta z^2 \quad (3.22)$$

with the free parameters $\{\theta_0, B\}$. Therefore, the idea is calculate the ACF to many shells with the same effective redshift ($z_{eff} = \frac{z_2+z_1}{2}$) but with different thickness (for example, $\{\delta z\} = \{0.005, 0.0075, 0.010, 0.0125, 0.015, 0.0175, 0.02\}$), use them to fit (3.22) and from that find out the correction factor (3.21).

Figure 13 – Simulations of α correction [11]

This shows the evolution of the shift of the θ_{FIT} with the redshift bin for the 14 cosmological models. Each color represents a shell with a certain radius and the horizontal axis represents its thickness. Each line of the same color represents one cosmological model simulation.

Finally, we use the $\alpha(\delta z)$ to correct the values of the θ_{FIT} already measured (in the same redshift z). The correction definition must be the same for the measurement, then as in (3.21)

$$\frac{\theta_0 - \theta(\delta z)}{\theta_0} = \alpha(\delta z) = \frac{\theta_{BAO} - \theta_{FIT}(\delta z)}{\theta_{BAO}} \quad (3.23)$$

Then, we expect that θ_{FIT} be corrected like

$$\theta_{BAO} = \frac{\theta_{FIT}(\delta z)}{1 - \alpha(\delta z)} \quad (3.24)$$

Note that although the measurement θ_{FIT} and the model of α depend on δz , the θ_{BAO} is not a function of it, because θ_{BAO} is the real value of BAO peak, which would be calculated in an ideal scenario where all the galaxies have the same redshift radius from

the observer. The value of θ_{BAO} needs to converge to the same, for whatever the δz , for example see Fig. 18.

4 RESULTS

In this chapter, we show the features of ACF measured (using DR12 and DR16 Galaxies North's Catalogs) and preliminary results for the localization of its peak as a function of redshift. Moreover a preliminary analysis using the angular scale measured in this work to constraint some cosmological parameters.

4.1 Detecting the θ_{FIT}

It was necessary to slice the catalogs into many shells. The regions $z < 0.3$ and beyond $z > 0.67$ own few galaxies to obtain a reliable analysis (see Fig. 6). The shells of different effective redshifts were selected without superposition, so they are independent measurements. As explained in the section 3.5, to the same effective redshift, shells with different thicknesses were used to measure the ACF, and we took the one with the best constraints over the BAO peak θ_{FIT} . In Fig. 14, we have some examples of best fits found out. In the Fig. 15 we can see the constraints over the parameters for the same examples.

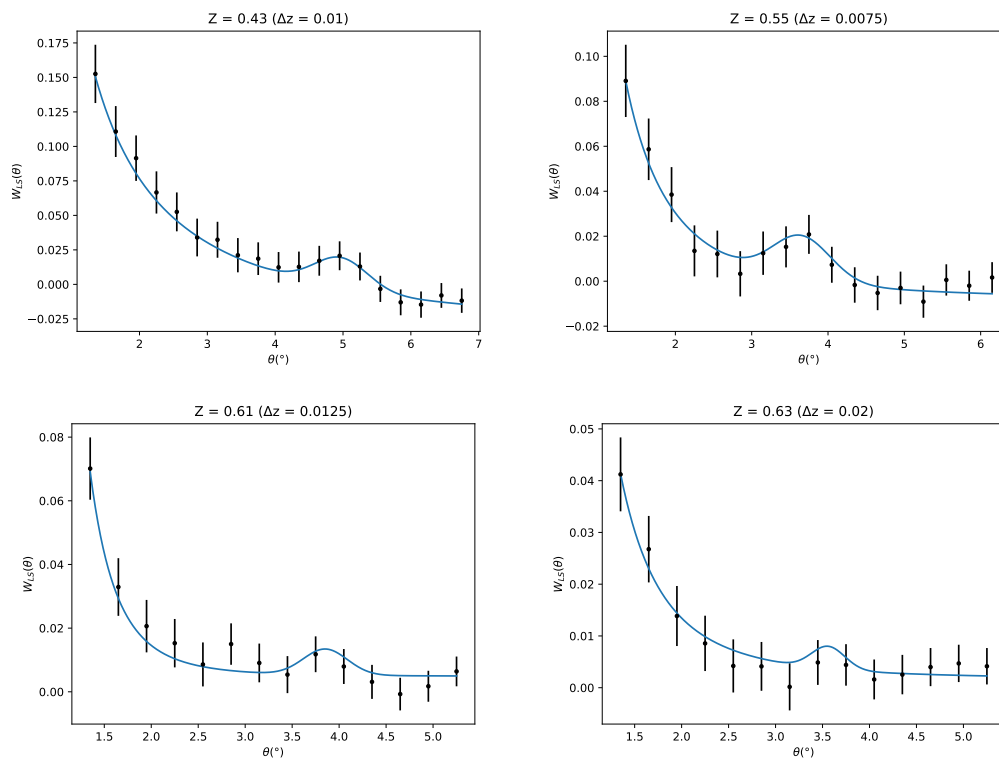


Figure 14 – Some examples of ACF (black dots) plots with their respectively best fit (blue line) found out by a global optimization method. As said before, the error bars shown here comes from diagonal of covariance matrix . The graphics of complete analysis are in the appendix B

The plots above show the distribution of the parameters that try to minimize the expression

$$\chi^2 = \sum_{ij} [W_i - W(\theta_i)] C_{ij}^{-1} [W_j - W(\theta_j)] \quad (4.1)$$

Where W_i are the ACF measured from the data, $W(\theta_i)$ is the parametrization calculated at $\theta = \theta_i$ and C_{ij} is the Covariance Matrix deduced from Mock Catalogs (For instance, see Fig. 16). Below, we explore the parametric space (starting from the point found out by global optimization) with a MCMC algorithm.

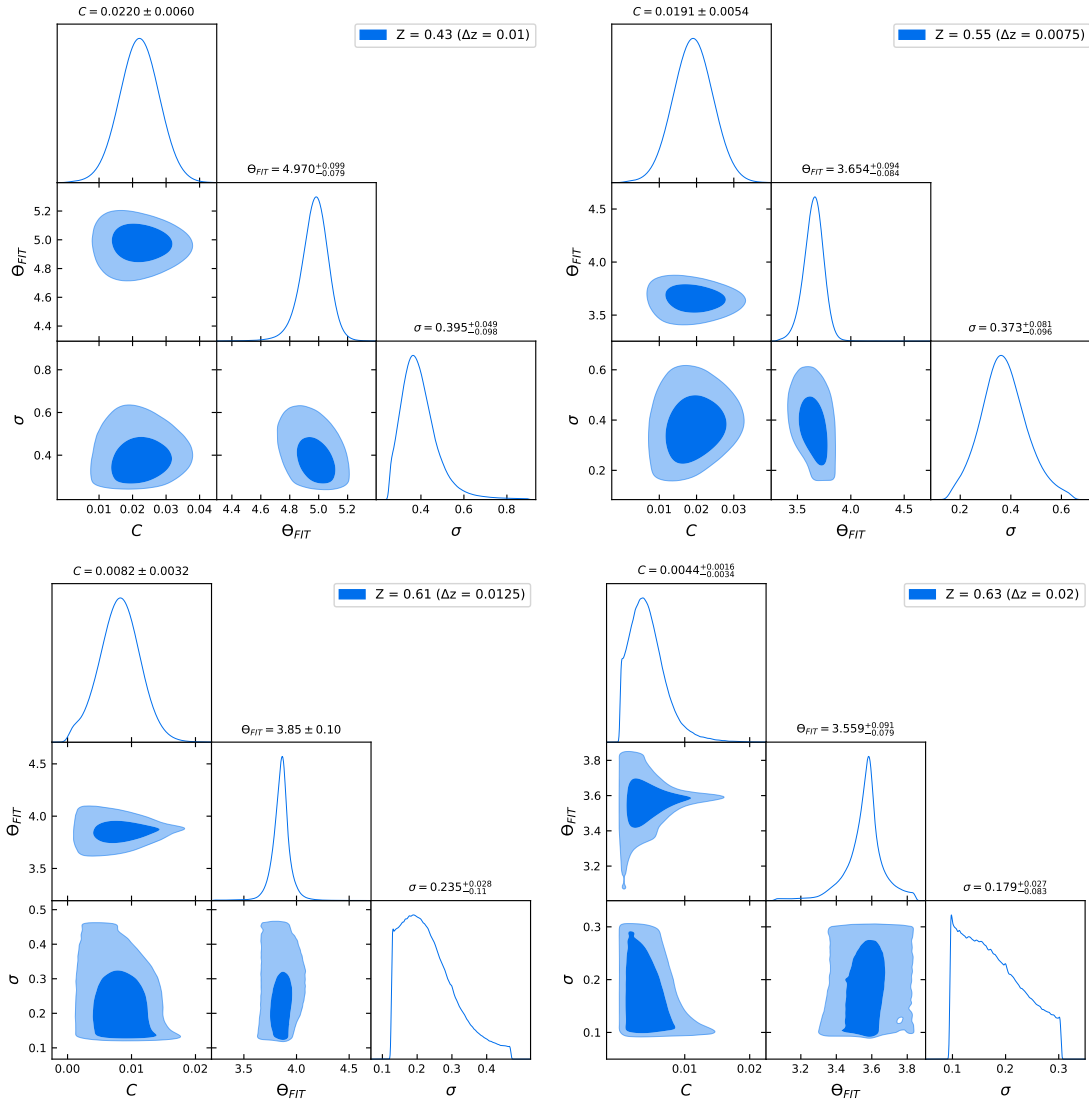


Figure 15 – The values are constrained over the regions (marginalized posterior distribution) with 68% and 95% confidence levels. It was used the open-source code EMCEE [12] to explore the parametric space (MCMC) and the codes available by GetDist to plot the distributions above [13]. See the appendix B for all analysis.

The image 15 shows some examples of constraints over the parameters that fit the peak. Although the localization of the peaks are well constrained (θ_{FIT} is the relevant parameter here), we can not always constraint the amplitude C and the width of the peak. This can be consequences from the random fluctuations (produced by nonlinear scales) and radial projection of BAO that produces perturbations of the ACF (see the shell $z_{eff} = 0.63$ on 15, the σ tends to achieve small values, scale characteristic of random fluctuations, that is, noise). For instance, the general appearance of the covariance and correlation matrices are shown below:

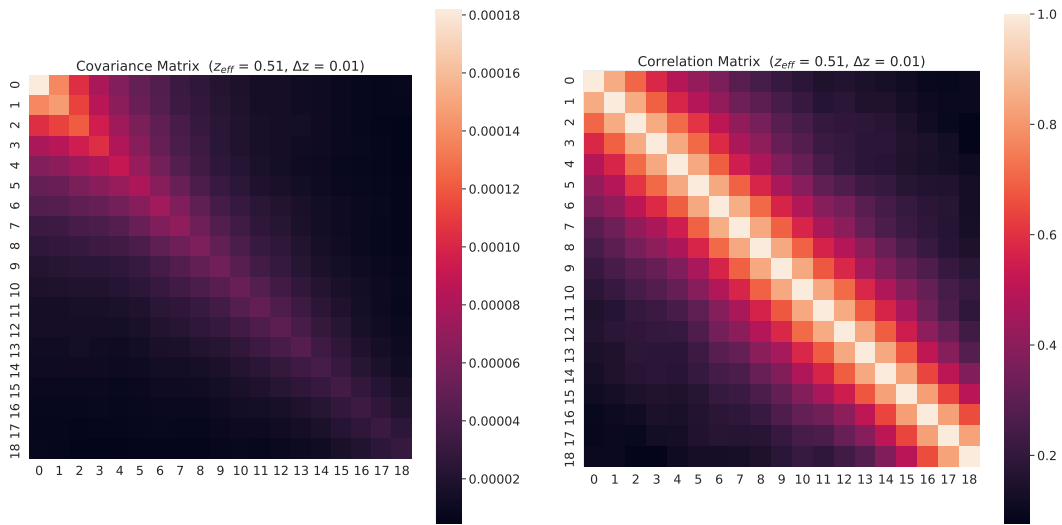


Figure 16 – A typical Covariance (left) and Correlation (right) Matrices deduced from 1000 Mocks Catalogs (This in particular refers to shell $z_{eff} = 0.51$ and $\delta z = 0.01$).

An important test about the statistical relevance of the MCMC analysis is its level of convergence. MCMC is a stochastic method, and we do not have any theorem that ensures the convergence of the chain to some point in the parametric space. Although we can estimate the statistic relevance of the point for what the chain apparently converges with the *Autocorrelation Time*. At the beginning of the chain, the samples are not independent of the initial positions, and so a small chain would not give us a good estimate of the posterior that we are looking for. In other words, the autocorrelation time gives us the estimation of how many steps (how much time since the beginning of sampling process) it is necessary to the chain forgets where it starts, see the appendix A. As all MCMC analyses, we have tested our chains and all of them show good estimation about the autocorrelation time, fortifying our confidence about the convergence of the chains. Below we show some examples of autocorrelation time estimation (all the cases followed the same pattern).

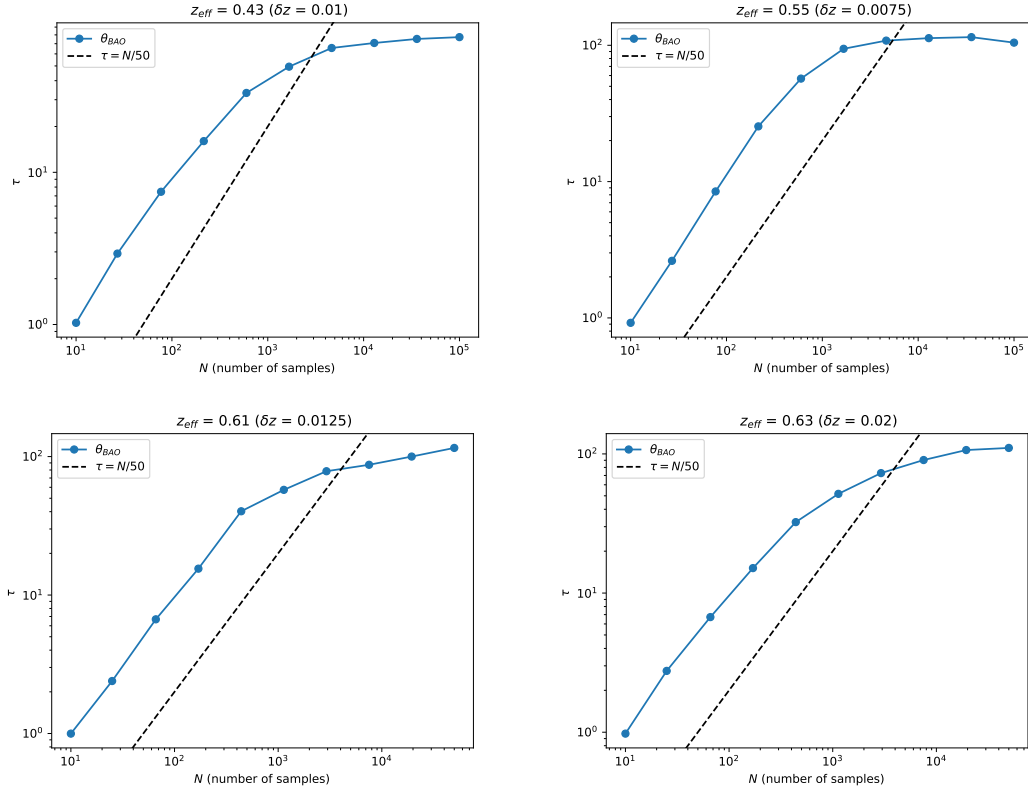


Figure 17 – The image shows the estimation of correlation time of parameter r_{dh} for the best fits with redshift $z = 0.43, 0.55, 0.61, 0.63$. The dashed line defines the limit (when crossed it) from what a reasonable estimate of autocorrelation time is obtained. See the appendix B.

The figure 17 shows the estimation of autocorrelation time in function of samples (number of steps). The true autocorrelation time is the value for what the curve would reach in an infinity number of steps. We see that, once the number of samples increases in the calculus of autocorrelation time the curve is closer to the horizontal line that defines the true value of the autocorrelation time. As said in the appendix A, the estimation of autocorrelation time starts to be reasonable for the chains longer than 50τ , that means when the estimates cross the line defined by $\tau = \frac{N}{50}$. A complete result for all the best shells analyzed are organized on the table 2.

4.2 Best θ_{BAO}

In the section 3.5, was explained why the finite width inserts a bias over the measured of θ_{FIT} . We proposed a method to extract a correction factor directly from the data using shells with various thicknesses, and from that to infer their displacement by what the peak undergoes. Some examples of how the peak is displaced are shown in the Fig. 18.

z_{eff}	δz	Number of Galaxies	θ_{FIT}	68% CL	95% CL
0.37	0.020	28113	6.01	+0.14 -0.17	+0.39 -0.34
0.43	0.010	14329	4.97	+0.1 -0.08	+0.19 -0.2
0.45	0.010	20247	4.36	+0.16 -0.15	+0.69 -0.7
0.51	0.0075	24871	4.79	+0.14 -0.14	+0.43 -0.41
0.53	0.010	32433	4.15	+0.13 -0.1	+0.24 -0.32
0.55	0.0075	22359	3.65	+0.1 -0.08	+0.18 -0.2
0.57	0.0075	20169	4.49	+0.14 -0.13	+0.33 -0.33
0.59	0.005	11635	4.23	+0.21 -0.19	+0.65 -0.47
0.61	0.0125	28385	3.85	+0.07 -0.07	+0.19 -0.19
0.63	0.020	37630	3.56	+0.09 -0.08	+0.23 -0.27

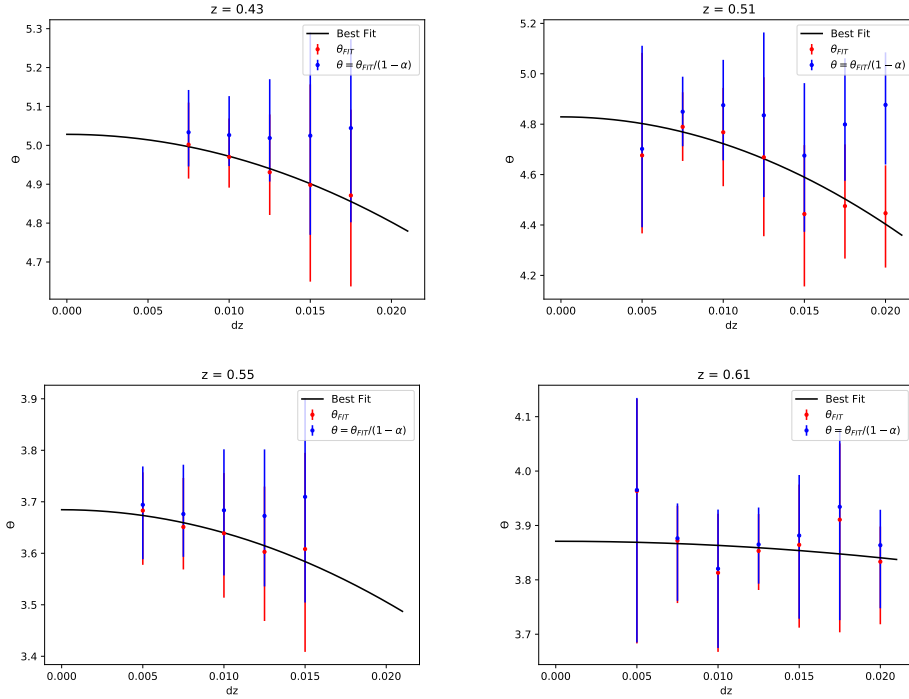
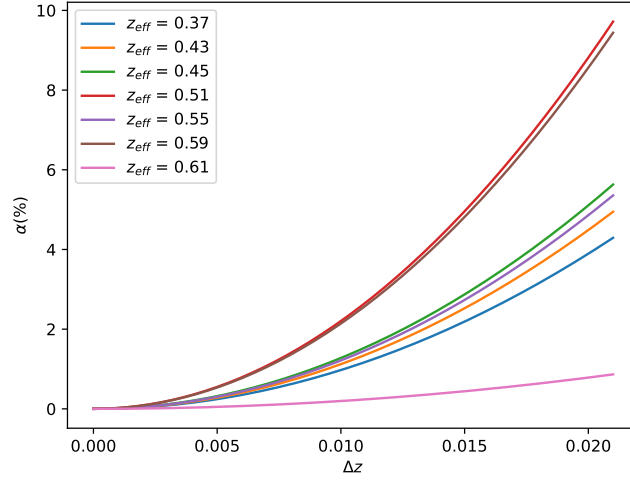
Table 2 – The result of θ_{FIT} for the best width.

Figure 18 – These examples show the typical displacement by what the peak undergoes. The red dots are the θ_{FIT} and the blue dots are the peaks corrected by the factor α (deduced from the fit represented by the black line), that is θ_{BAO} . We see that the peak goes to smaller angle values as increase the width (δz) of the shell. Note also after the correction the peaks tend to form a straight line, around the θ_{BAO} value (as we expect, because the final value can not depend of the width of the shell).

Figure 19 – α correction deduced directly from the data

Note that some shells were not used, for instance the $\delta z = 0.02$ (for $z_{eff} = 0.43$) and $\delta z = 0.0175, 0.02$ (for $z_{eff} = 0.55$). They are neglected because their transverse BAO signals already were stifled by the radial BAO projections (as can be seen in the example 12), then the localization of the peak is not reliable in these shells. Thinner shells also can be neglected, if they do not have galaxies enough to obtain a robust statistical measurement and have a lot of noise. Note that the factor correction remains of order 1% within the region that our analysis is ($\delta z \leq 0.02$) as can be seen in the table 3, the complete result of this analysis.

z_{eff}	θ_{FIT}	θ_{BAO}	68% CL	α (%)
0.37	6.01	6.26	$+0.15$ -0.17	3.9
0.43	4.97	5.03	$+0.1$ -0.08	1.1
0.45	4.36	4.42	$+0.17$ -0.15	1.3
0.51	4.79	4.85	$+0.14$ -0.14	1.20
0.53	4.15	4.15	$+0.13$ -0.1	0.0
0.55	3.65	3.68	$+0.1$ -0.08	0.7
0.57	4.49	4.49	$+0.14$ -0.13	0.0
0.59	4.23	4.25	$+0.22$ -0.19	0.5
0.61	3.85	3.87	$+0.07$ -0.07	0.3
0.63	3.56	3.56	$+0.09$ -0.08	0.0

Table 3 – Table that includes the θ_{BAO} results. Note the uncertainties increase by the factor α as well.

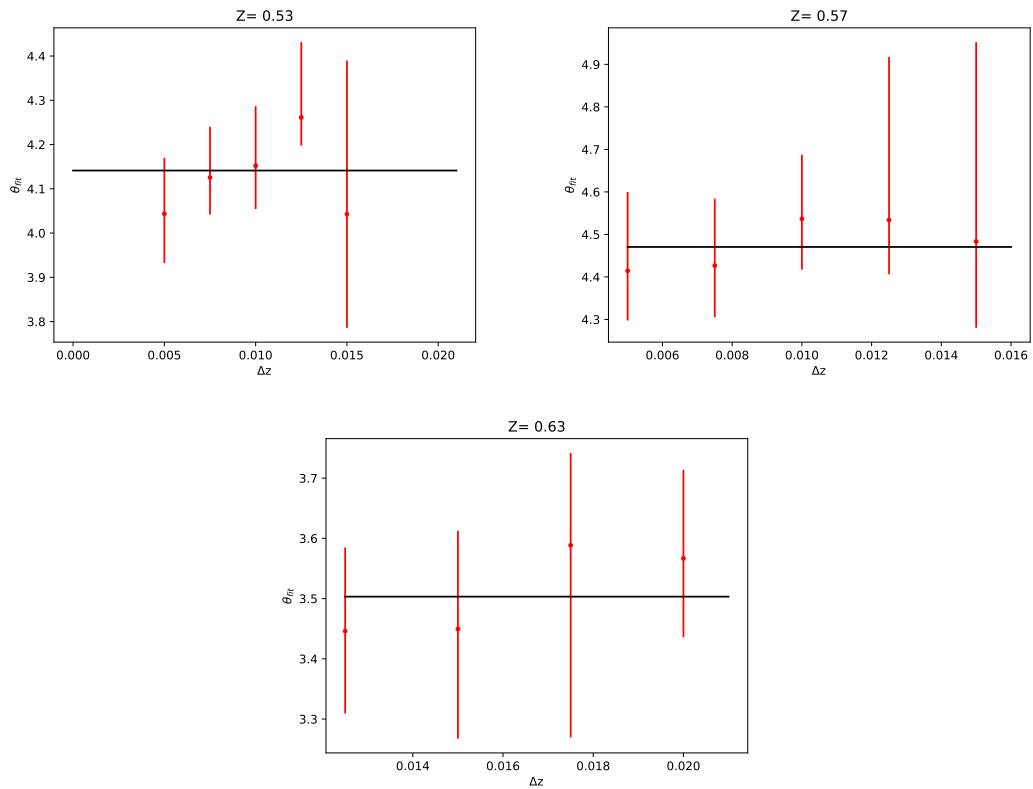


Figure 20 – Peaks displacements of the effective redshift $z_{eff} = 0.53, 0.57, 0.63$ measured.

Even the determination of the α factor working for most cases, there are three cases where it did not work, that is when $z_{eff} = 0.53, 0.57, 0.63$ (Fig. 20). The peaks fluctuate around a straight line along δz , so the fit of the points to find that the correction factor was not possible. Below is shown a visual difference between the angular scale of BAO measured in this work and those predicted by parameters of the best fit from [1].

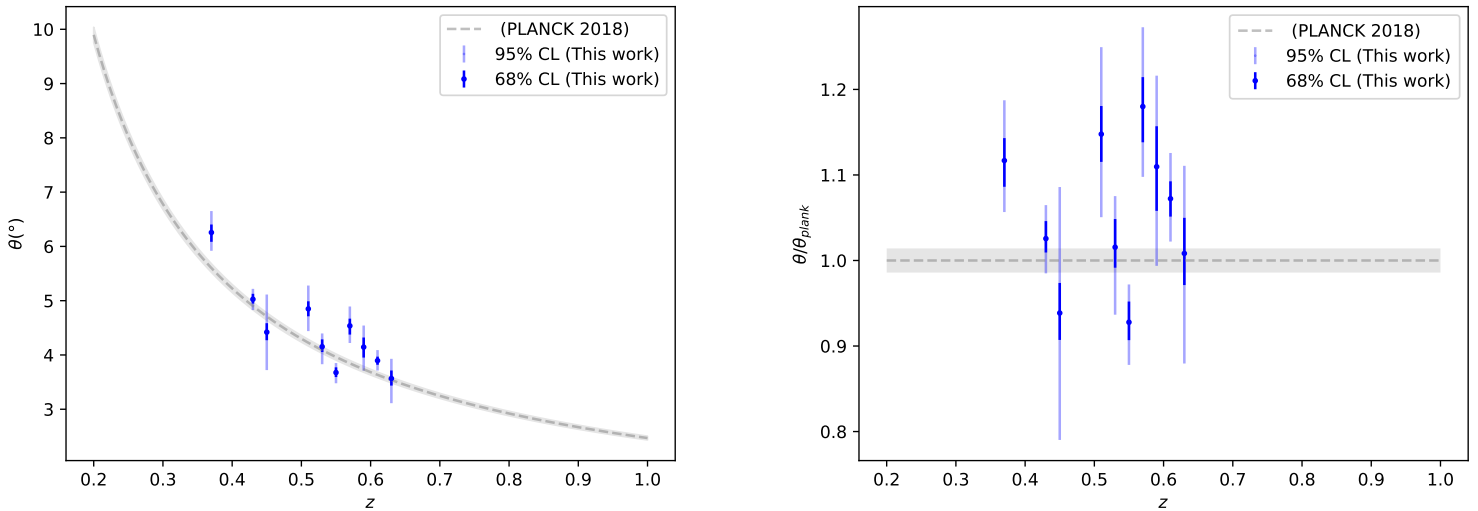


Figure 21 – On the left image it is shown the angular scale predicted by the parameters of the best fit Planck 2018 [1] together with the measurements of this work. On the right, we normalize the same graphic with the predicted curve.

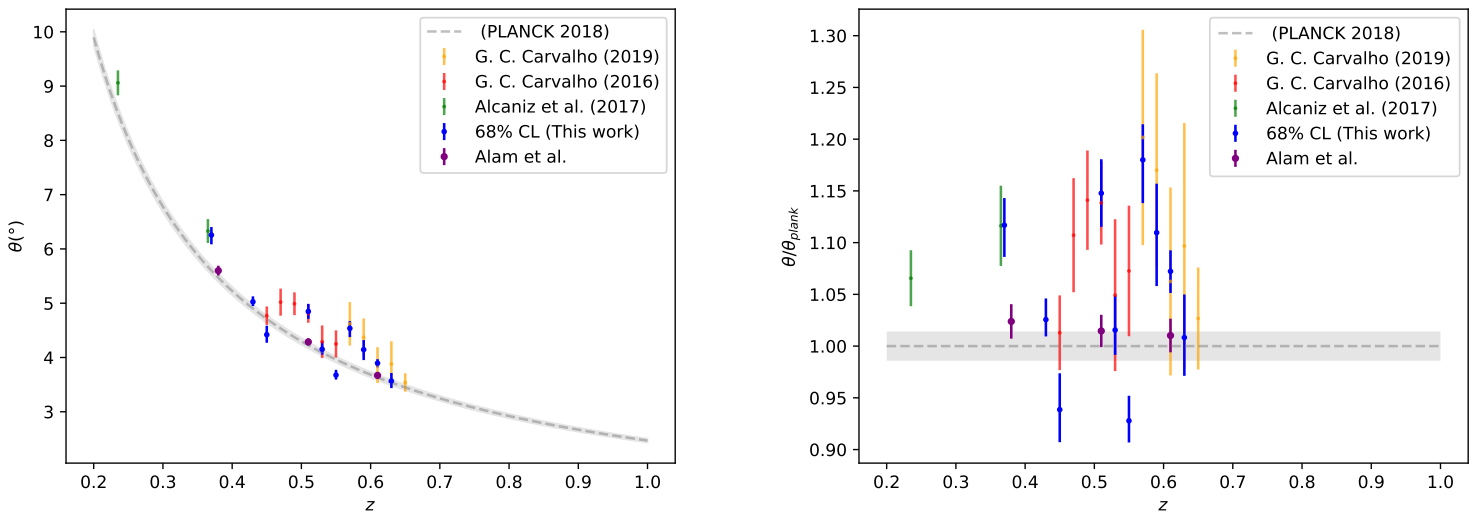


Figure 22 – Here was added the measurements of angular BAO scale from previous works [4], [14], [5], [6].

4.3 Constraints on Cosmological Parameters

Once measured the angular BAO scale, we can use that information to infer the best values of parameters from some cosmological model. As we know, the angular scale

can be related to some cosmological model through the expression below

$$\theta(z) = \frac{r_d}{(1+z)D_a(z)} \quad (4.2)$$

where $r_d \equiv r_s(z_{drag})$, that means the sound horizon calculated in z_{drag} , which is the redshift when the baryons are no more dragged by the photons. The diameter angular distance (D_a) is given by the expression (1.34) and it inserts the proportionality of H_0 in the expression. The logarithm of likelihood used for BAO data (how we call the data set measured by this work) is proportional to the expression below

$$\chi_{BAO}^2 = \sum \left(\frac{\theta(z) - \theta_{BAO}(z)}{\sigma_{BAO}} \right)^2 \quad (4.3)$$

where $\theta(z)$ is the theoretical expression given by (4.2), $\theta_{BAO}(z)$ are the angular scale measured in this work and σ_{BAO} is the standard deviation (68% of confidence level) of the data. Considering the Λ CDM model we use the MCMC method to explore the parametric space formed by the set $\{r_d h, \Omega_m\}$, where we have used the definition ($H_0 = 100h \frac{km}{sMpc}$). Note that there is a degeneracy in the determination of r_d and H_0 parameters from the above expression, which means that we can not determine the values r_d and H_0 independently.

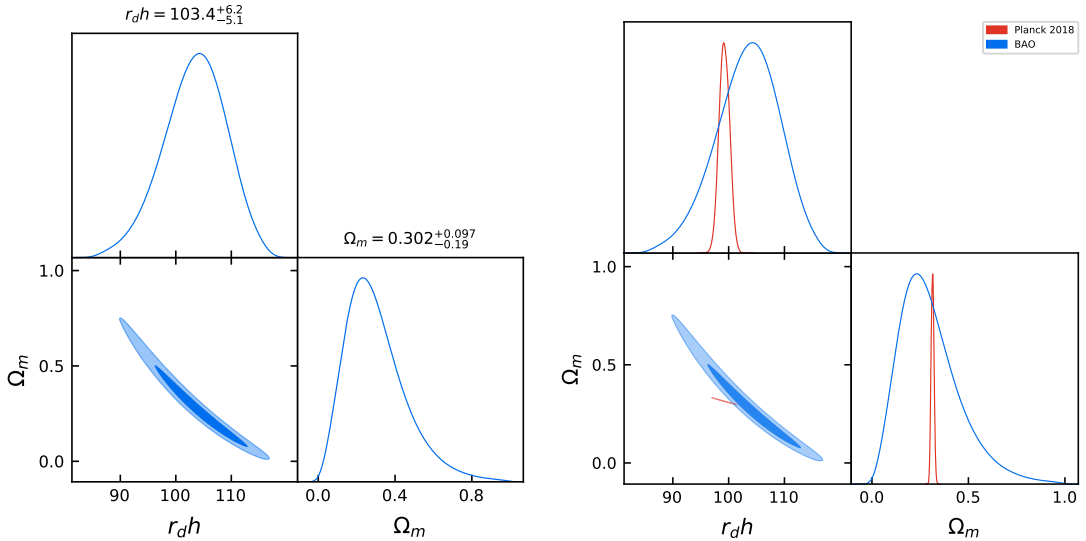


Figure 23 – The first image (left) shows the distribution proportional to the posterior that we have obtained from MCMC analysis to the parameters $r_d h$ and Ω_m , and their respective expected values. The second image (right) is shown the same distribution together with the distributions from Planck 2018.

We see, in the image above, that despite there is a difference of sound horizon ($r_d h$) values resulted from the Planck and Angular BAO-only analysis the tension between them

is smaller than one sigma (see the table 4) because of the large error bars (confidence level) of the parameter. Using additional independent data could set tighter constraints to the parameter. Another data set used in the analysis is the apparent magnitude of supernovas available by the Pantheon catalog [50], which gives us 1048 measures. It helps us to constraint the quantity of matter in the universe. The apparent magnitude of supernovae can be considered a function of redshift given by

$$\mu(z) = m_b - M_b = 5 \log\{D_L(z)\} + 25 = 5 \log \left\{ \frac{(1+z)c}{H_0} \int_0^z E(z')^{-1} dz' \right\} + 25 \quad (4.4)$$

Where m_b is the apparent magnitude, M_b is the absolute magnitude and $D_L(z)$ is the luminosity distance given by the expression (1.32), with the velocity of light in $\frac{km}{s}$ units and considering the a flat universe. Considering the Λ CDM model we use the MCMC method to explore the parametric space formed by the set $\{r_d, H_0, \Omega_m, M_b\}$. To break down that degeneracy between r_d and H_0 , we need to insert some additional information on the analysis, like informative prior distribution. Then, we use flat priors for all parameters except in M_b , for which we have used a Gaussian as prior with mean and standard deviation -19.2435 ± 0.0373 (that prior is the value that can be inferred from analysis of SH0ES collaboration as explained here [51]).

To the supernovae data set, we have the

$$\chi_{Sn}^2 = (m_b - m_b(z)) \cdot \Sigma^{-1} \cdot (m_b - m_b(z)) \quad (4.5)$$

$$\chi_{Sn}^2 = (y(z) - M_b) \cdot \Sigma^{-1} \cdot (y(z) - M_b) \quad (4.6)$$

where we have defined the function $y(z) = m_b - \mu(z)$ (m_b is the apparent magnitude measured and $m_b(z)$ the function of apparent magnitude). The covariance matrix is represented by the Σ , and it is calculated as $\Sigma = \Sigma_{error} + \Sigma_{sys}$ (Σ_{error} is the diagonal matrix with uncertainties of m_b measure and Σ_{sys} the matrix with systematic effects). Finally, the total χ^2 function is given by

$$\chi^2 = \chi_{BAO}^2 + \chi_{Sn}^2 \quad (4.7)$$

With this χ^2 function we have the posterior distributions shown in the figures below

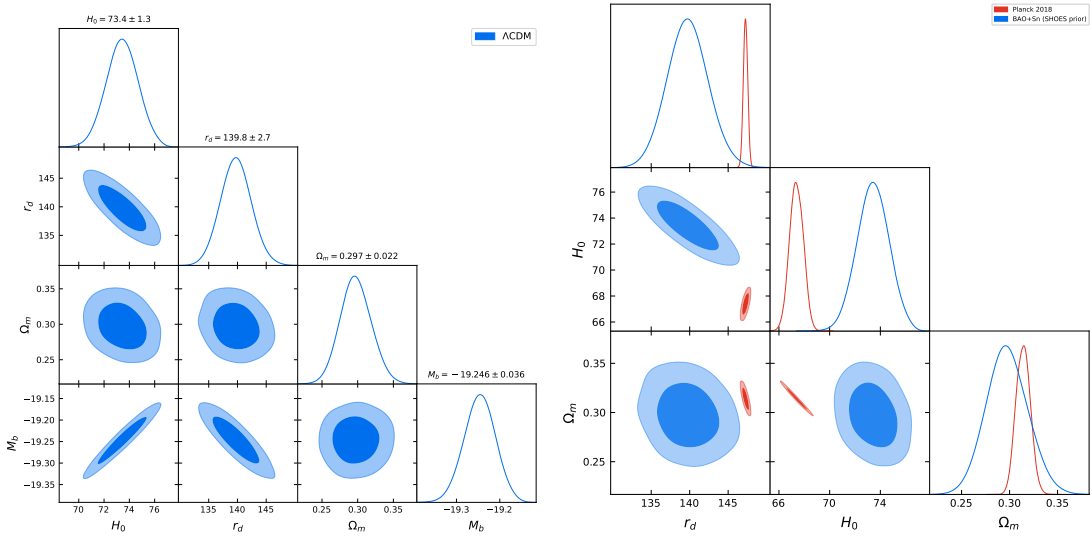


Figure 24 – Both images above show the distribution in parametric using SH0ES prior on M_b . In the right side the image compare it with the distribution from Planck 2018 results.

In order to avoid some bias that could come from the prior on M_b used before, we can redefine our set of parameters and look for a value of $r_d h$ (where $H_0 = 100h \frac{km}{sMpc}$). To do that, we rewrite the equation (4.4) such that

$$m_b = 5 \log \left\{ \frac{(1+z)c}{100} \int_0^z E(z')^{-1} dz' \right\} + 25 + \hat{M}_b \quad (4.8)$$

where we define a new parameter $\hat{M}_b \equiv M_b - 5 \log\{h\}$. Then, using the set of parameters $\{r_d h, \Omega_m, \hat{M}_b\}$ we can to constraint them without using some informative prior, avoiding bias. We just use flat priors, and the result is shown below

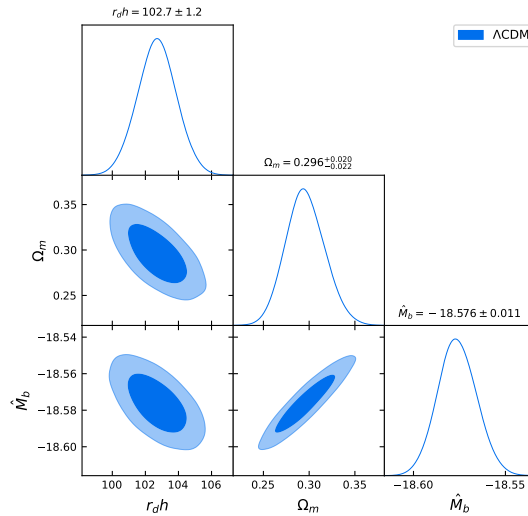


Figure 25 – This image shows the distribution in parametric using flat prior on \hat{M}_b .

Again, testing the robustness of the analysis we can calculate the estimation of autocorrelation time to each analysis, shown below in the figure 26

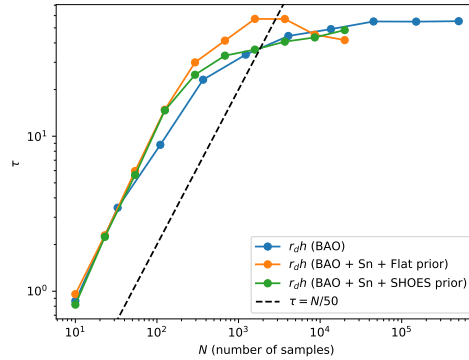


Figure 26 – Convergence test for each MCMC analysis, following the algorithm available by EMCEE [A](#)

We can compare our results (with and without SHOES priors) with those from the Planck 2018 as shown in the figure 27

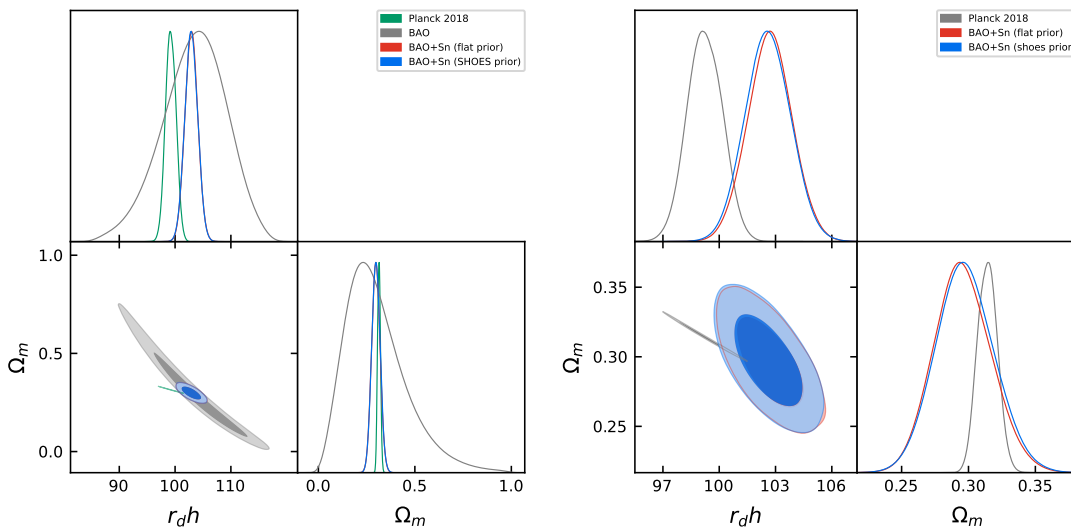


Figure 27 – In the left image it is shown the distribution in parametric as a result of analysis in Planck 2018 and this work using just BAO data (grey distribution), BAO plus supernovae data with flat priors (red distribution) and with SHOES prior (blue distribution). In the right image it is shown the same distributions except that comes from BAO data only (it is like a zoom to see better the small difference between the distribution that comes from flat and SHOES prior).

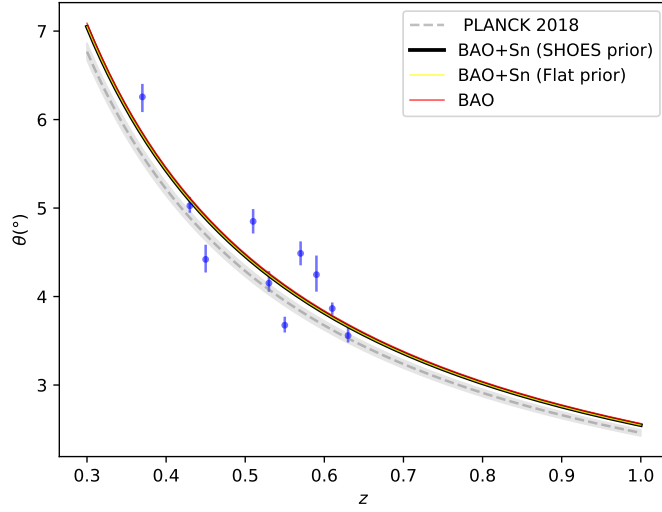


Figure 28 – This image shows the curve of angular scales given by 4.2 and using the best fit of the above analysis.

We can see in the figure 27 that, even using the flat prior to avoid some bias, the posterior distribution tends to agree with the analysis that has used the SHOES prior. We can estimate the tension between the results from Planck 2018 and our analysis over the parameter $r_d h$ using the formula

$$\text{Tension} = \frac{|r_d h - r_d h_{\text{planck}}|}{\sqrt{\sigma^2 + \sigma_{\text{planck}}^2}} \quad (4.9)$$

So, the tension find out in this analysis using flat prior and SHOES prior on the absolute magnitude of supernovae is about 2.3σ and 2.2σ , respectively (as can be seen in the table 4).

Analysis	Data set	$r_d h$	68% CL	Tension with PL18
PL18	CMB	99.23	± 0.94	-
Flat Prior	BAO	103.4	± 5.7	0.72σ
SHOES Prior	BAO+Sn	102.6	± 1.17	2.2σ
Flat Prior	BAO+Sn	102.7	± 1.21	2.3σ

Table 4 – Table that summarize the results of analysis.

5 CONCLUSIONS

In this work, we have used the last catalogs of galaxies released by the SDSS (DR12 and DR16) until now, to estimate the Angular BAO scale. The method used here consists in to count the pairs of galaxies, weighted by statistical factors (3.3), with approximated same redshift. Using the estimator for ACF proposed by Landy and Szalay [46], we can fit it with a phenomenological model that mixes a power law and a gaussian function (3.20). Due to the finite thickness of the redshift shells, a bias over the localization of the bump of ACF is inserted. In order to correct this displacement in the bump, we try to find out the behavior of peaks as we change the thickness of the redshift shells. Then, we calculate the peak of ACF for different redshift widths (δz), at each effective redshift (z_{eff}). Then, we use an almost cosmology model-independent method to make these measurements (the only dependence of some cosmological model inserted in this method comes from the calculation of covariance matrix which uses Mocks produced by some fiducial cosmology, even though, this cosmology model dependence is weak).

Until now, we have obtained ten measurements of the angular BAO scale using independent bins of redshift. They show considerably smaller uncertainties compared with previous estimates (that also comes from an almost model-independent methodology as [5], [6] and [4]), which can be consequence that we use currently data with density of galaxies increased. Besides, it was verified a clearly displacement of angular bump in ACF, as we change the width of redshift shells, for almost effective redshift in the analysis, except by the $z_{eff} = 0.53, 0.57, 0.63$. After the corrections in the localization of the bump in ACF, deduced from this phenomenology, the final result of the peaks (θ_{BAO}) changed about 1% of the value fitted initially (θ_{FIT}), which agree with what was suggested by simulations of cosmological models [11].

The result of our preliminary analysis suggests a disagreement between the values predicted by the best fit of CMB data (Planck 2018 [1]) and the angular BAO scale measured by an almost independent cosmological method within a redshift interval $0.37 \leq z \leq 0.63$ (see figures 27 and 28). Using just the BAO angular data, measured in this work, we can not set strong constraints on the parameter Ω_m , neither $r_d h$ as consequence (larger error bars provide the small tension of 0.72σ to the Planck result). Using additional data set of supernovae these constraints become tighter over the Ω_m (the data set of supernovae does not carry relevant information about sound horizon in this analysis), and then the $r_d h$ is more constrained as well. From the analysis including supernovae data the tension was calculated in this work reaching about 2.3σ . This work is in progress yet, and after obtaining all data points (we intend to increase the number of independent measurements of angular BAO scale for redshift between $0.33 \leq z \leq 0.65$) we can make a more complete analysis about this tension, including more convergence tests of analysis already done.

BIBLIOGRAPHY

- 1 AGHANIM, N. et al. Planck 2018 results-vi. cosmological parameters. *Astronomy & Astrophysics*, EDP sciences, v. 641, p. A6, 2020. 12 citations on pages [5](#), [6](#), [8](#), [10](#), [14](#), [21](#), [30](#), [31](#), [35](#), [80](#), [81](#), and [87](#).
- 2 RIESS, A. G. et al. Cosmic distances calibrated to 1% precision with gaiaedr3 parallaxes and hubble space telescope photometry of 75 milky way cepheids confirm tension with Λ cdm. *The Astrophysical Journal*, American Astronomical Society, v. 908, n. 1, p. L6, Feb 2021. ISSN 2041-8213. Disponível em: <http://dx.doi.org/10.3847/2041-8213/abdbaf>. 4 citations on pages [5](#), [6](#), [21](#), and [35](#).
- 3 VALENTINO, E. D. et al. In the realm of the hubble tension – a review of solutions. *arXiv preprint arXiv:2103.01183*, 2021. 6 citations on pages [5](#), [6](#), [7](#), [14](#), [35](#), and [36](#).
- 4 ALCANIZ, J. S. et al. Measuring baryon acoustic oscillations with angular two-point correlation function. In: *Gravity and the Quantum*. [S.l.]: Springer, 2017. p. 11–19. 6 citations on pages [5](#), [6](#), [8](#), [14](#), [81](#), and [87](#).
- 5 CARVALHO, G. et al. Baryon acoustic oscillations from the sdss dr10 galaxies angular correlation function. *Physical Review D*, APS, v. 93, n. 2, p. 023530, 2016. 7 citations on pages [5](#), [6](#), [8](#), [14](#), [69](#), [81](#), and [87](#).
- 6 CARVALHO, G. C. et al. *Measuring the transverse baryonic acoustic scale from the SDSS DR11 galaxies*. 2019. 6 citations on pages [5](#), [6](#), [8](#), [14](#), [81](#), and [87](#).
- 7 FREEDMAN, W. L. et al. Final results from the hubble space telescope key project to measure the hubble constant. *The Astrophysical Journal*, IOP Publishing, v. 553, n. 1, p. 47, 2001. 2 citations on pages [7](#) and [22](#).
- 8 FIXSEN, D. et al. The cosmic microwave background spectrum from the full coBE* firas data set. *The Astrophysical Journal*, IOP Publishing, v. 473, n. 2, p. 576, 1996. 2 citations on pages [7](#) and [29](#).
- 9 HEYMANS, C. et al. Kids-1000 cosmology: Multi-probe weak gravitational lensing and spectroscopic galaxy clustering constraints. *Astronomy & Astrophysics*, EDP Sciences, v. 646, p. A140, Feb 2021. ISSN 1432-0746. Disponível em: <http://dx.doi.org/10.1051/0004-6361/202039063>. 2 citations on pages [7](#) and [37](#).
- 10 EISENSTEIN, D. J.; SEO, H.-J.; WHITE, M. On the robustness of the acoustic scale in the low-redshift clustering of matter. *The Astrophysical Journal*, IOP Publishing, v. 664, n. 2, p. 660, 2007. 2 citations on pages [7](#) and [54](#).
- 11 SANCHEZ, E. et al. Tracing the sound horizon scale with photometric redshift surveys. *Monthly Notices of the Royal Astronomical Society*, Blackwell Publishing Ltd Oxford, UK, v. 411, n. 1, p. 277–288, 2011. 6 citations on pages [7](#), [14](#), [70](#), [71](#), [72](#), and [87](#).
- 12 Foreman-Mackey, D. et al. emcee: The MCMC Hammer. , v. 125, n. 925, p. 306, mar. 2013. 3 citations on pages [8](#), [70](#), and [75](#).

- 13 LEWIS, A. GetDist: a Python package for analysing Monte Carlo samples. 2019. Disponível em: <<https://getdist.readthedocs.io>>. 3 citations on pages 8, 70, and 75.
- 14 ALAM, S. et al. The eleventh and twelfth data releases of the sloan digital sky survey: Final data from sdss-iii. *The Astrophysical Journal Supplement Series*, American Astronomical Society, v. 219, n. 1, p. 12, Jul 2015. ISSN 1538-4365. Disponível em: <<http://dx.doi.org/10.1088/0067-0049/219/1/12>>. 3 citations on pages 8, 58, and 81.
- 15 DYSON, F. W.; EDDINGTON, A. S.; DAVIDSON, C. IX. a determination of the deflection of light by the sun's gravitational field, from observations made at the total eclipse of may 29, 1919. *Philosophical Transactions of the Royal Society of London. Series A, Containing Papers of a Mathematical or Physical Character*, The Royal Society London, v. 220, n. 571-581, p. 291-333, 1920. One citation on page 14.
- 16 CLEMENCE, G. M. The relativity effect in planetary motions. *Reviews of Modern Physics*, APS, v. 19, n. 4, p. 361, 1947. One citation on page 14.
- 17 CAMARENA, D.; MARRA, V. A new method to build the (inverse) distance ladder. *Monthly Notices of the Royal Astronomical Society*, Oxford University Press, v. 495, n. 3, p. 2630-2644, 2020. One citation on page 14.
- 18 NUNES, R. C. et al. Cosmological parameter analyses using transversal bao data. *Monthly Notices of the Royal Astronomical Society*, Oxford University Press, v. 497, n. 2, p. 2133-2141, 2020. One citation on page 14.
- 19 CARROLL, S. M. *Spacetime and geometry*. [S.l.]: Cambridge University Press, 2019. 3 citations on pages 17, 19, and 23.
- 20 AVILA, F. et al. The scale of homogeneity in the local universe with the alfalfa catalogue. *Journal of Cosmology and Astroparticle Physics*, IOP Publishing, v. 2018, n. 12, p. 041-041, Dec 2018. ISSN 1475-7516. Disponível em: <<http://dx.doi.org/10.1088/1475-7516/2018/12/041>>. One citation on page 20.
- 21 BENGALY, C. A. P. et al. Probing cosmological isotropy with planck sunyaev-zeldovich galaxy clusters. *Monthly Notices of the Royal Astronomical Society*, Oxford University Press (OUP), v. 466, n. 3, p. 2799-2804, Dec 2016. ISSN 1365-2966. Disponível em: <<http://dx.doi.org/10.1093/mnras/stw3233>>. One citation on page 20.
- 22 HAMILTON, J.-C. What have we learned from observational cosmology? *Studies in History and Philosophy of Science Part B: Studies in History and Philosophy of Modern Physics*, Elsevier, v. 46, p. 70-85, 2014. One citation on page 20.
- 23 HUBBLE, E. A relation between distance and radial velocity among extra-galactic nebulae. *Proceedings of the National Academy of Sciences*, National Acad Sciences, v. 15, n. 3, p. 168-173, 1929. One citation on page 21.
- 24 MARTIN, J. Everything you always wanted to know about the cosmological constant problem (but were afraid to ask). *Comptes Rendus Physique*, Elsevier, v. 13, n. 6-7, p. 566-665, 2012. One citation on page 21.
- 25 BAUMANN, D. Tasi lectures on inflation. *arXiv preprint arXiv:0907.5424*, 2009. 2 citations on pages 34 and 56.

- 26 VÁZQUEZ, J. A.; PADILLA, L. E.; MATOS, T. Inflationary cosmology: from theory to observations. *arXiv preprint arXiv:1810.09934*, 2018. One citation on page 34.
- 27 AMENDOLA, L. Coupled quintessence. *Physical Review D*, American Physical Society (APS), v. 62, n. 4, Jul 2000. ISSN 1089-4918. Disponível em: <<http://dx.doi.org/10.1103/PhysRevD.62.043511>>. One citation on page 35.
- 28 YANG, W. et al. Interacting dark energy with time varying equation of state and the h_0 tension. *Physical Review D*, American Physical Society (APS), v. 98, n. 12, Dec 2018. ISSN 2470-0029. Disponível em: <<http://dx.doi.org/10.1103/PhysRevD.98.123527>>. One citation on page 35.
- 29 HU, W.; SAWICKI, I. Models of cosmic acceleration that evade solar system tests. *Physical Review D*, American Physical Society (APS), v. 76, n. 6, Sep 2007. ISSN 1550-2368. Disponível em: <<http://dx.doi.org/10.1103/PhysRevD.76.064004>>. One citation on page 35.
- 30 MALUF, J. W. The teleparallel equivalent of general relativity. *Annalen der Physik*, Wiley, v. 525, n. 5, p. 339–357, Mar 2013. ISSN 0003-3804. Disponível em: <<http://dx.doi.org/10.1002/andp.201200272>>. One citation on page 35.
- 31 BAHAMONDE, S.; BÖHMER, C. G.; WRIGHT, M. Modified teleparallel theories of gravity. *Physical Review D*, American Physical Society (APS), v. 92, n. 10, Nov 2015. ISSN 1550-2368. Disponível em: <<http://dx.doi.org/10.1103/PhysRevD.92.104042>>. One citation on page 35.
- 32 TRÖSTER, T. et al. Cosmology from large-scale structure. *Astronomy Astrophysics*, EDP Sciences, v. 633, p. L10, Jan 2020. ISSN 1432-0746. Disponível em: <<http://dx.doi.org/10.1051/0004-6361/201936772>>. One citation on page 37.
- 33 ICHIKI, K.; OGURI, M.; TAKAHASHI, K. Constraints from the wilkinson microwave anisotropy probe on decaying cold dark matter. *Physical Review Letters*, American Physical Society (APS), v. 93, n. 7, Aug 2004. ISSN 1079-7114. Disponível em: <<http://dx.doi.org/10.1103/PhysRevLett.93.071302>>. One citation on page 37.
- 34 CHUDAYKIN, A.; GORBUNOV, D.; TKACHEV, I. Dark matter component decaying after recombination: Sensitivity to baryon acoustic oscillation and redshift space distortion probes. *Physical Review D*, American Physical Society (APS), v. 97, n. 8, Apr 2018. ISSN 2470-0029. Disponível em: <<http://dx.doi.org/10.1103/PhysRevD.97.083508>>. One citation on page 37.
- 35 PIATTELLA, O. *Lecture notes in cosmology*. [S.l.]: Springer, 2018. 6 citations on pages 39, 47, 51, 53, 55, and 70.
- 36 DODELSON, S. *Modern cosmology*. [S.l.]: Elsevier, 2003. One citation on page 51.
- 37 DURRER, R. *The cosmic microwave background*. [S.l.]: Cambridge University Press, 2020. One citation on page 52.
- 38 MUKHANOV, V. *Physical foundations of cosmology*. [S.l.]: Cambridge university press, 2005. One citation on page 56.

- 39 Eisenstein, D. J. et al. SDSS-III: Massive Spectroscopic Surveys of the Distant Universe, the Milky Way, and Extra-Solar Planetary Systems. , v. 142, n. 3, p. 72, set. 2011. One citation on page 58.
- 40 Blanton, M. R. et al. Sloan Digital Sky Survey IV: Mapping the Milky Way, Nearby Galaxies, and the Distant Universe. , v. 154, n. 1, p. 28, jul. 2017. One citation on page 58.
- 41 Dawson, K. S. et al. The Baryon Oscillation Spectroscopic Survey of SDSS-III. , v. 145, n. 1, p. 10, jan. 2013. One citation on page 58.
- 42 Dawson, K. S. et al. The SDSS-IV Extended Baryon Oscillation Spectroscopic Survey: Overview and Early Data. , v. 151, n. 2, p. 44, fev. 2016. One citation on page 58.
- 43 AHUMADA, R. et al. The 16th data release of the sloan digital sky surveys: first release from the apogee-2 southern survey and full release of eboss spectra. *The Astrophysical Journal Supplement Series*, IOP Publishing, v. 249, n. 1, p. 3, 2020. One citation on page 58.
- 44 COORDINATE Transformations. <http://www.castor2.ca/07_News/headline_062515.html>. (Accessed on 02/12/2021). One citation on page 60.
- 45 HAUSER, M.; PEEBLES, P. Statistical analysis of catalogs of extragalactic objects. ii. the abell catalog of rich clusters. *The Astrophysical Journal*, v. 185, p. 757–786, 1973. One citation on page 62.
- 46 LANDY, S. D.; SZALAY, A. S. Bias and variance of angular correlation functions. *The Astrophysical Journal*, v. 412, p. 64–71, 1993. 2 citations on pages 62 and 87.
- 47 ANDERSON, L. et al. The clustering of galaxies in the sdss-iii baryon oscillation spectroscopic survey: baryon acoustic oscillations in the data releases 10 and 11 galaxy samples. *Monthly Notices of the Royal Astronomical Society*, Oxford University Press, v. 441, n. 1, p. 24–62, 2014. One citation on page 63.
- 48 ANDERSON, L. et al. The clustering of galaxies in the sdss-iii baryon oscillation spectroscopic survey: baryon acoustic oscillations in the data release 9 spectroscopic galaxy sample. *Monthly Notices of the Royal Astronomical Society*, Blackwell Science Ltd Oxford, UK, v. 427, n. 4, p. 3435–3467, 2012. One citation on page 63.
- 49 FELDMAN, H. A.; KAISER, N.; PEACOCK, J. A. Power spectrum analysis of three-dimensional redshift surveys. *arXiv preprint astro-ph/9304022*, 1993. One citation on page 63.
- 50 PS1COSMO: Supernovae from PanSTARRS. Disponível em: <<https://archive.stsci.edu/prepds/ps1cosmo/index.html>>. One citation on page 83.
- 51 CAMARENA, D.; MARRA, V. Local determination of the hubble constant and the deceleration parameter. *Physical Review Research*, American Physical Society (APS), v. 2, n. 1, Jan 2020. ISSN 2643-1564. Disponível em: <<http://dx.doi.org/10.1103/PhysRevResearch.2.013028>>. One citation on page 83.

APPENDIX A – STATISTICAL TOOLS

The advance of observational cosmology, collecting more data for each day, has required the use of methods to deal with much data, extracting from them relevant information to guide us in the understanding of the universe. Then, statistical tools are fundamental to data analysis in different areas of knowledge, including cosmology.

A.1 Fundamental Concepts

When we are describing a deterministic theory, in classical mechanics, for example, we can have functions of space that indicate a certain value to each position of space. When we go to the reality of some experiments we need to deal with uncertainties over the measurements, considering our example here, that means we can obtain different values of that function for the same position of space. To be able to investigate and compare the measurements with theory we need to define some concepts.

A.1.1 Random Variables

There are more general definitions of random variables (RV) but here we can use them as functions that map a sample space (the space of outcomes) to some real space. For example, in an experiment of tossing a coin the sample space is $\{head, tail\}$, and we can define some random variable that gives us 0 when we get head and 1 for tail, in other words, the values of that function is not predictable, because the tossing coin event is not deterministic, it just have probabilities to outcome head or tail. That definition is important because all that we can measure is, essentially, a random variable. Because of that, to obtain a robust measure about any observable we need a huge sample to have reliable estimates. In the limit where the RV can assume continuous values, we can define a probability distribution function (PDF)

$$f(x)dx = P(x) \tag{A.1}$$

where $\int f(x)dx = 1$ and $f(x) \geq 0$. Here x represent all possible real values that some RV can assume, and $P(x)$ the probability that RV can assume a value between x and $x+dx$. That definition is straightforward extended to n random variables, as $f(x_1, x_2, \dots, x_n)$. When we are dealing with more than one RV it could exist another aspect important. If the RV are independent, that means, their outcomes do not affect the probabilities of RV outcomes, then we can write the total PDF as $f(x_1, x_2, \dots, x_n) = f_1(x_1)f_2(x_2)\dots f_n(x_n) = \prod_i^n f_i(x_i)$.

Once collected the data, it is needed to use some rules to calculate the observable directly from the data. That rule to estimate some observable is called *Estimator*. there may be several different rules to estimate the same observable from the data, and each of them has properties that can be used as criteria of choice. Then, consider that θ is a parameter (observable) that can be inferred from data (that is from pdf $f(x)$) by the estimator denoted as $\hat{\theta}$. The estimator can have the following properties

- **Consistency:** If the estimated value $\hat{\theta}$ approximate to the parameter θ arbitrarily as the number of data (n) tends to infinity, then we say that $\hat{\theta}$ is a consistent estimator. That means, the probability of obtaining an estimative different from the parameter of distribution is

$$\lim_{n \rightarrow \infty} P(|\theta - \hat{\theta}| > \epsilon) = 0 \quad (\text{A.2})$$

for every $\epsilon > 0$.

- **Bias:** The expected value of any RV $g(x)$ (note that functions of RV, in that case, x, are also RV) is defined as

$$E[g(x)] = \int g(x)f(x)dx \quad (\text{A.3})$$

where the $f(x)$ is the pdf of x. That definition is the same for estimators as they are functions (rules) of the data (RV). Then, we can define the *Bias* of the estimator as

$$b = E[\hat{\theta}] - \theta \quad (\text{A.4})$$

We said that estimator $\hat{\theta}$ is unbiased if $b = 0$, which means, its expected value is equal to the value parameter of the distribution.

- **Efficiency:** The definition of variance of some RV $g(x)$ is:

$$V[g(x)] = \int (g(x) - E[g(x)])^2 f(x)dx \quad (\text{A.5})$$

Once we have many experiments, and many estimates of the expected value of $\hat{\theta}$, then we can calculate the variance of it. Then, we define the Mean Square Error (MSE) as an estimator of how much we expect that the estimator $\hat{\theta}$ spread out from the parameter value θ

$$MSE = E[(\hat{\theta} - \theta)^2] = V[\hat{\theta}] + b^2 \quad (\text{A.6})$$

Then, we have the statistical and systematic effects in the total error. In general, the bias comes from some previous concepts in the definition of estimator rule, which can be reduced considering a rule more complex (more general with more freedom degrees). Although that, the variance increases with the complexity of the estimator, if the number of data keeps the same quantity (there is a more complex estimator with the same data, the statistical error increases). In other words, there is some trade-off between variance and bias. Then, it is common to choose an estimator that minimizes the MSE, which means, that relation between bias and variance (look for a balance between them). The property of how much the estimator minimizes the MSE can be seen as efficiency.

A.2 Bayes' Theorem

Consider the notation $P(A|B)$ as the probability of obtaining outcome from A after already have got B. If the $P(A \cap B)$ is the probability of outcome be from A and B subsets, then we have

$$P(A \cap B) = P(A|B)P(B) = P(B|A)P(A) \quad (\text{A.7})$$

Then, the Bayes' Theorem says that

$$P(A|B) = \frac{P(B|A)P(A)}{P(B)} \quad (\text{A.8})$$

We can use that theorem to infer from the data important issues about the theory that we are using to describe the observable phenomenon. Previous section we have denoted a pdf of x as $f(x)$. Despite we have used this notation the pdf is a function of data and parametrized by some collection of parameters $\vec{\theta}$, and we can write that like $f(x_i; \vec{\theta})$. For example, if $f(x)$ is a Gaussian distribution of x , it have two fundamental parameters that are the mean μ and the standard error σ , that means, in this case $\vec{\theta} = \{\mu, \sigma\}$. With that notation, we can rewrite the Bayes' theorem as

$$P(\vec{\theta}|x) = \frac{P(x|\vec{\theta})P(\vec{\theta})}{P(x)} \quad (\text{A.9})$$

Where $x = \{x_i\}$ is the data set collected in an experiment. Usually, we do not analyze the probability itself, what is informative and more accessible for us is their distributions functions, then

$$f_p(\vec{\theta}|x) = \frac{f_L(x|\vec{\theta})f_{pr}(\vec{\theta})}{f_e(x)} \quad (\text{A.10})$$

On the right side of the equation, we have $f_L(x|\vec{\theta})$ which means the probability distribution of obtaining the data given some value of $\vec{\theta}$ (that in general defines some theoretical model), called *Likelihood*. The term $f_e(x)$ means the probability of obtaining that data set, called *Evidence*. The $f_{pr}(\vec{\theta})$ is the probability distribution of obtaining the value $\vec{\theta}$ for the parameters, which is information that comes from previous experiments and because of that we call that as *Prior*. In general given some data set $x = \{x_i\}$, the interest concern in the values of parameters that define the model that it is being tested. This information is contained in the left side of the above equation, $f_p(\vec{\theta}|x)$, in other words, the left side gives us the probability distribution of the parameters have given a data set x . This is called *Posterior* distribution and gives the final distribution of the parameters of any theoretical model using the information of likelihood, priors and evidence.

The prior distribution can insert some bias in the analysis, which means, it can influence the analysis with previous information, for example, we know that gravity on earth surface is about $g = 9.8m/s^2$ thus we could use $f_{pr}(g)$ as a Gaussian centered on that value. Although, usually the prior is chosen as a constant, over some region where we believe that the best value of $\vec{\theta}$ remains, that is, the prior says that we do not know any previous information about the parameters, except they are limited by some region on the parametric space. We call this as flat prior. Assuming this kind of posterior, we used to define the best value of $\vec{\theta}$ that satisfies the equation below

$$\frac{\partial L(x_i; \vec{\theta})}{\partial \vec{\theta}} = 0 \quad (\text{A.11})$$

where we have rewrite the likelihood function $L(x_i; \vec{\theta}) \equiv f_L(x|\vec{\theta})$. This condition is what we need to maximize the probability distribution of parameters that give us the data set observed, in other words, the values of parameters that explain the data set collected better.

A.3 MCMC

The above method is very useful to find out the better set of parameters for a given data set. Although, that does not give us so much information about the posterior distribution of the parameters, and their correlations. Wondering about that, we can use a stochastic method called Markov Chain Monte Carlo (MCMC). The MCMC method

proposes to build the distribution on the parametric space that is proportional to the posterior distribution, but to it be clear we need to introduce some concepts.

Markov Chain is a sequence of random variables (X_1, X_2, \dots, X_n) , such that the probability of include on the sequence the element X_{t+1} depends just from element X_t , here X_t denote a general point on the parametric space. Then, given some initial point on the parametric space, we denote the probability of the sequence goes from X_t to X_{t+1} by the *Transition Function* $T(X_t, X_{t+1})$. Then, this transition function is what builds the parameter's distribution. Roughly speaking, can be thought that this is related to the target posterior function, and then the Markov Chain should sample the distribution proportional to the posterior distribution that we want to know. That means, for a Markov Chain we have

$$\frac{T(\vec{\theta}_t, \vec{\theta}_{t+1})}{T(\vec{\theta}_{t+1}, \vec{\theta}_t)} = \frac{P(\vec{\theta}_{t+1}|x)}{P(\vec{\theta}_t|x)} \quad (\text{A.12})$$

where $P(\vec{\theta}, \{x\})$ is the posterior distribution. That relation suggests the proportionally between the sample and the target posterior distribution. We say that the chain converges when the successive elements of the chain are sampled by the target distribution (we will discuss the convergence of the chain later). Once we have a complete chain, we can estimate the expected value of any function that depends of the parameters as

$$E[f(\vec{\theta})] = \int f(\vec{\theta})P(\vec{\theta}|x)d\vec{\theta} \approx \frac{1}{n} \sum_{t=1}^n f(\vec{\theta}_t) \quad (\text{A.13})$$

It is also useful to know the marginalized distribution of each parameter, that means, how is the distribution of the parameter $\theta^{(i)}$ only. For example, this can be calculated as

$$P(\theta^{(1)}) = \int P(\vec{\theta}, x)d\theta^{(2)} \dots d\theta^{(m)} \quad (\text{A.14})$$

where m is the number of free parameters (the length of vector $\vec{\theta}$).

A.3.1 The Metropolis-Hastings algorithm

There are several algorithms to implement this method, and here we are going to talk about the most simple of them, the *Metropolis-Hasting Algorithm* (MHA). Then, to sample the target posterior distribution we can divide the algorithm into four steps

- (I) Start the chain with a random point θ_0 in the parametric space. To optimize the convergence we can choose a point that represents the best fit or any close to it.

- (II) Now it is necessary to propose a candidate for a possible next value of the sequence. In order to do that, we define the *Proposal Distribution* that will be responsible to draw the candidate. We denote it as $q(\theta_0, \theta_t)$.
- (III) Once the candidate was sampled by proposal function we need to calculate its probability to be accepted, and inserted on the chain, or rejected. We expected that the total probability is proportional to $q(\vec{\theta}_0, \vec{\theta}_t)$ (probability of $\vec{\theta}_t$ to be proposed) times posterior distribution calculated in that value $P_t \equiv P(\vec{\theta}_t, x)$ (works as a weight). Then, we accept the candidate as part of the chain with the probability given by

$$\alpha = \min \left(\frac{P_t q(\vec{\theta}_t, \vec{\theta}_0)}{P_0 q(\vec{\theta}_0, \vec{\theta}_t)}, 1 \right) \quad (\text{A.15})$$

That is, if $\frac{P_t q(\vec{\theta}_t, \vec{\theta}_0)}{P_0 q(\vec{\theta}_0, \vec{\theta}_t)} > 1$ then the candidate is accept with a probability of $\alpha = 1$, otherwise the candidate is accept with the probability given by $\alpha = \frac{P_t q(\vec{\theta}_t, \vec{\theta}_0)}{P_0 q(\vec{\theta}_0, \vec{\theta}_t)}$. To the MHA the proposal is symmetric, $q(x, y) = q(y, x)$ (usually used a gaussian function for that), then

$$\alpha = \min \left(\frac{P_t}{P_0}, 1 \right) \quad (\text{A.16})$$

This means that the chain will, more frequently, point to directions where posterior distribution increases.

- (IV) If the new candidate is accepted it needs to be inserted in the chain, otherwise the old point is inserted again into the chain. After that, it goes back to step (II) and repeats the process.

In this work, we use a similar algorithm to explore the parametric space of the models used. That algorithm is available by the open-source codes EMCEE [] which is based on a work done by Goodman and Weare in 2010 (GW10) []. That algorithm has shown better results concerning the convergence time, that is, the number of steps necessary to the sample converges is less than the traditional algorithm of MCMC.

A.3.2 Convergence Test

Once we obtain the Markov Chain, we need to test its convergence. It is important to be clear, there is no theorem ensuring the convergence of some general chain. The method that will be shown here just tries to estimate a possible convergence.

The autocorrelation time is a direct measure of how many steps are necessary until the chain produces independent samples. The autocovariance function of a time series $X(t)$ is defined as

$$C_f(T) = \lim_{t \rightarrow \infty} \text{cov}[f(X_{t+T}), f(X_t)] \quad (\text{A.17})$$

that means, the covariance between the samples separated by T steps. Then, the value of T for what $C_f(T) = 0$ is the number of steps needed to the chain be independent of where it started. In the context of Markov Chains, this covariance can be calculated by

$$C_f(T) = \frac{1}{N-T} \sum_{n=0}^{N-T} [f(X_{T+n}) - \langle f \rangle][f(X_n) - \langle f \rangle] \quad (\text{A.18})$$

The autocorrelation time (also called integrated autocorrelation time) can be estimated from the samples as

$$\tau_f \equiv \sum_{\tau=-N}^N \frac{C_f(\tau)}{C_f(0)} = 1 + 2 \sum_{\tau=1}^N \frac{C_f(\tau)}{C_f(0)} \quad (\text{A.19})$$

Although, the implementations on the EMCEE try to deal with the noise that comes from terms with long τ in the sum above. Then, it is used an estimator like

$$\tau_f(M) = 1 + 2 \sum_{\tau=1}^M \frac{C_f(\tau)}{C_f(0)} \quad (\text{A.20})$$

where $M \leq N$. This estimator decreases the variance of τ_f at the cost of some added bias. Although, this estimator works very well using chains longer than $50\tau_f$, when it is sampled using the algorithm GW10 which provides a convergence faster.

APPENDIX B – GRAPHICS

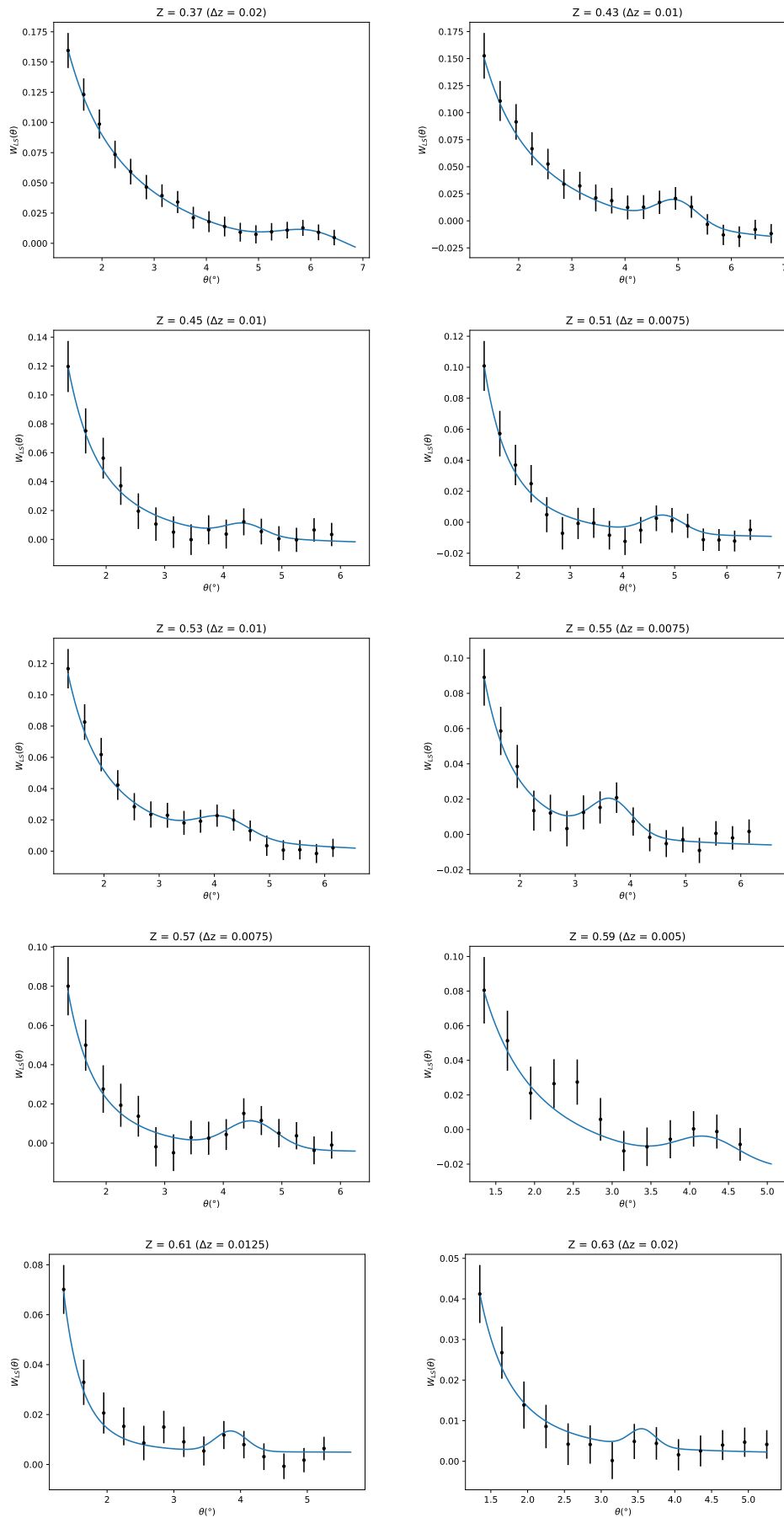
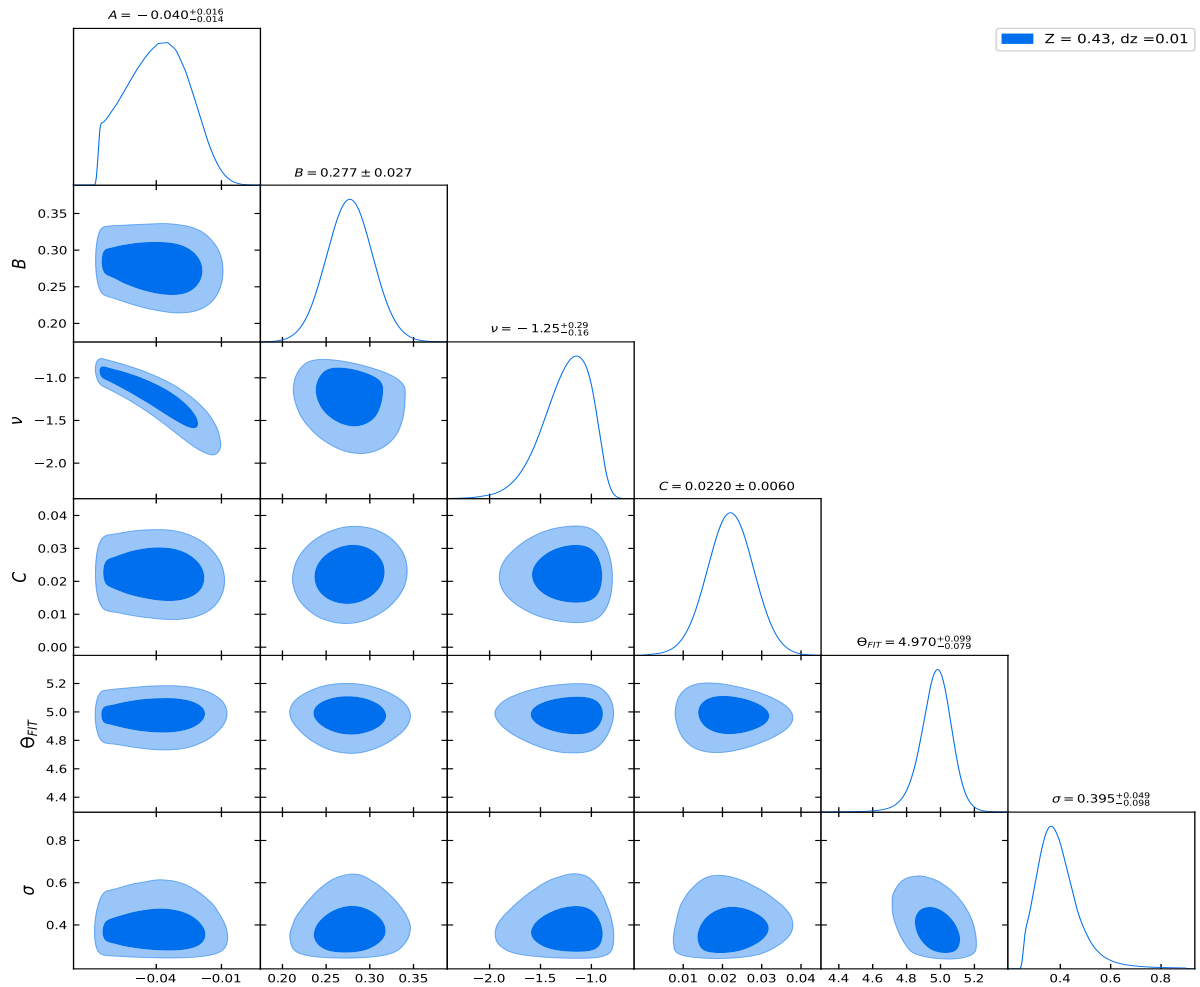
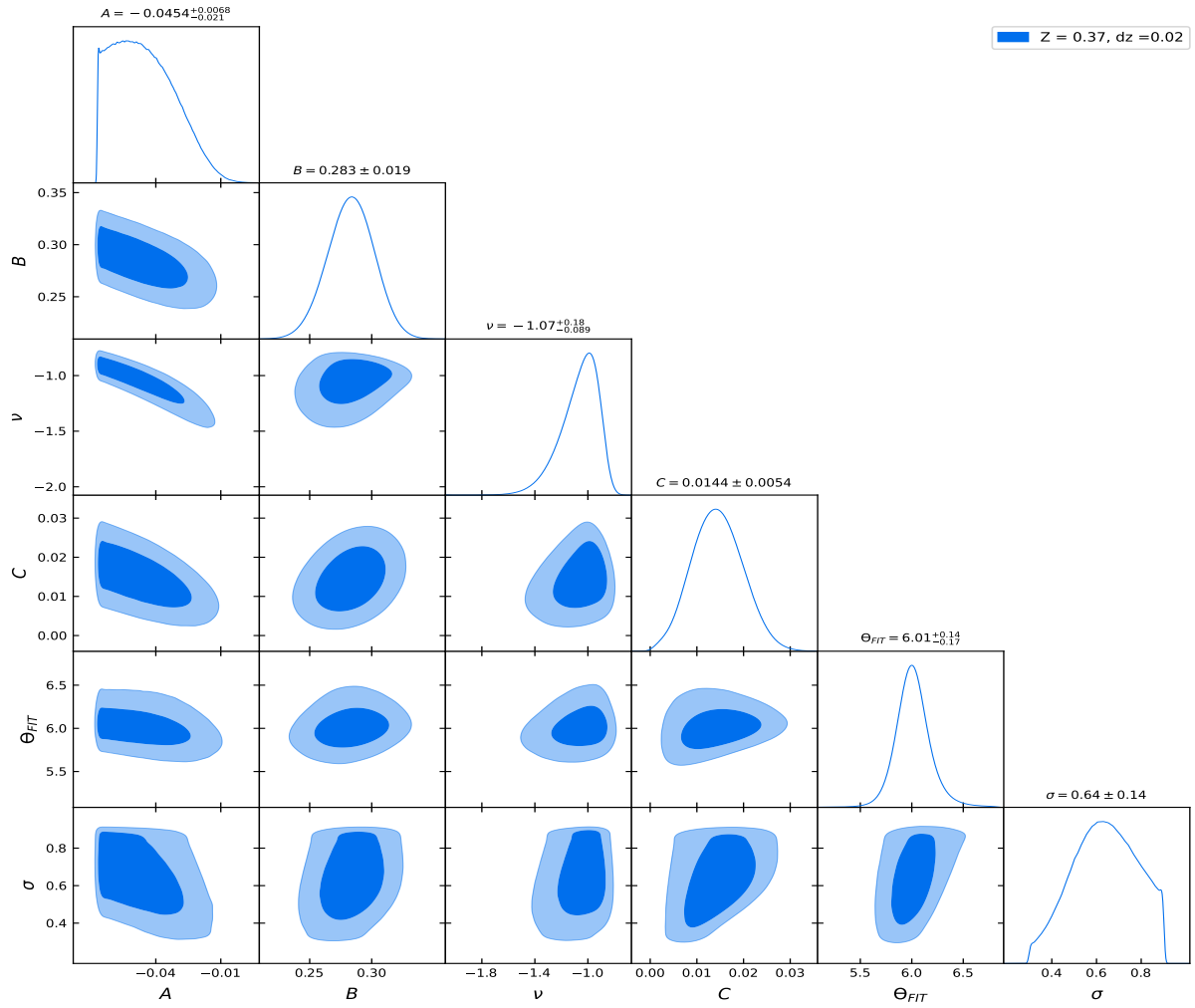
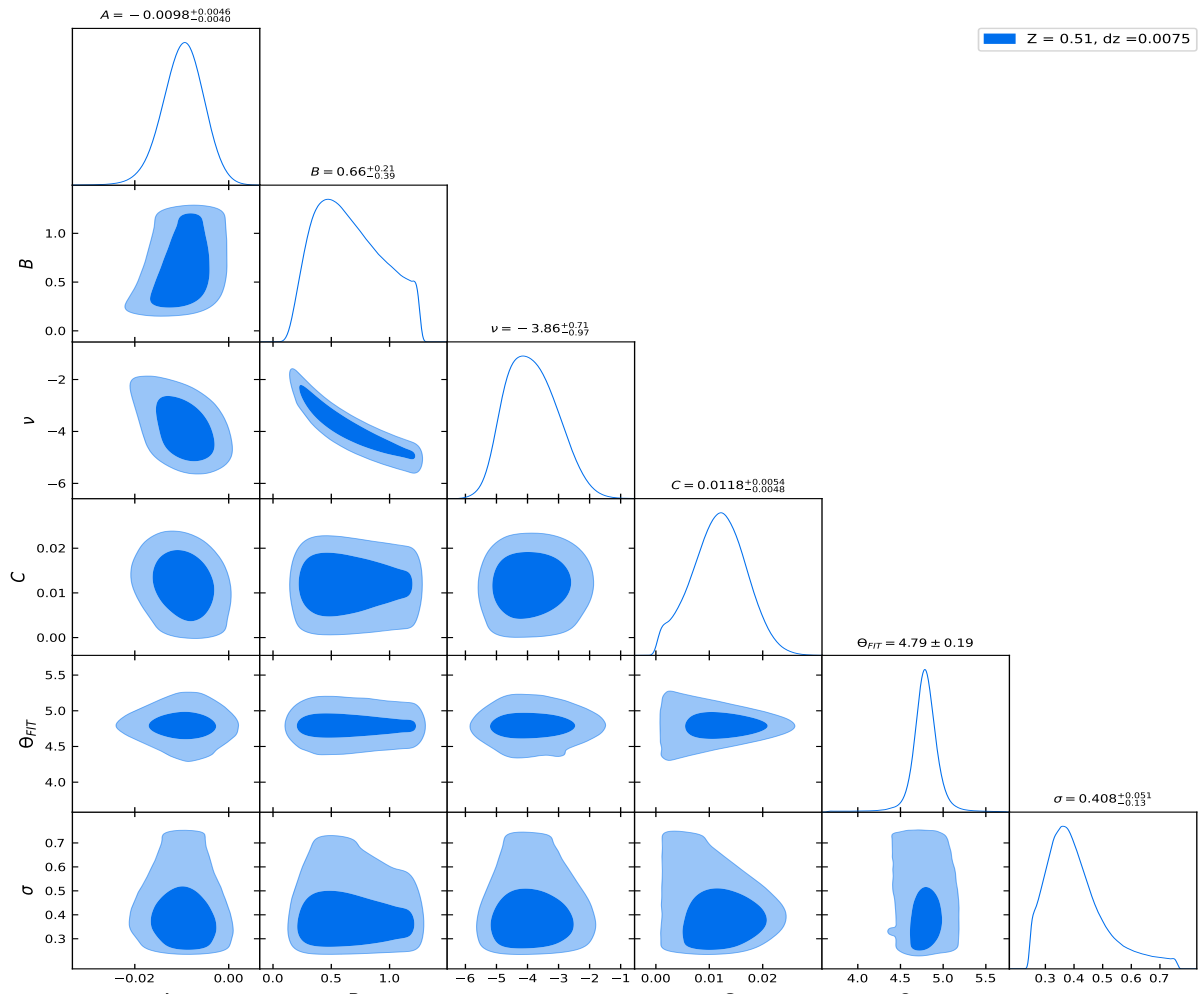
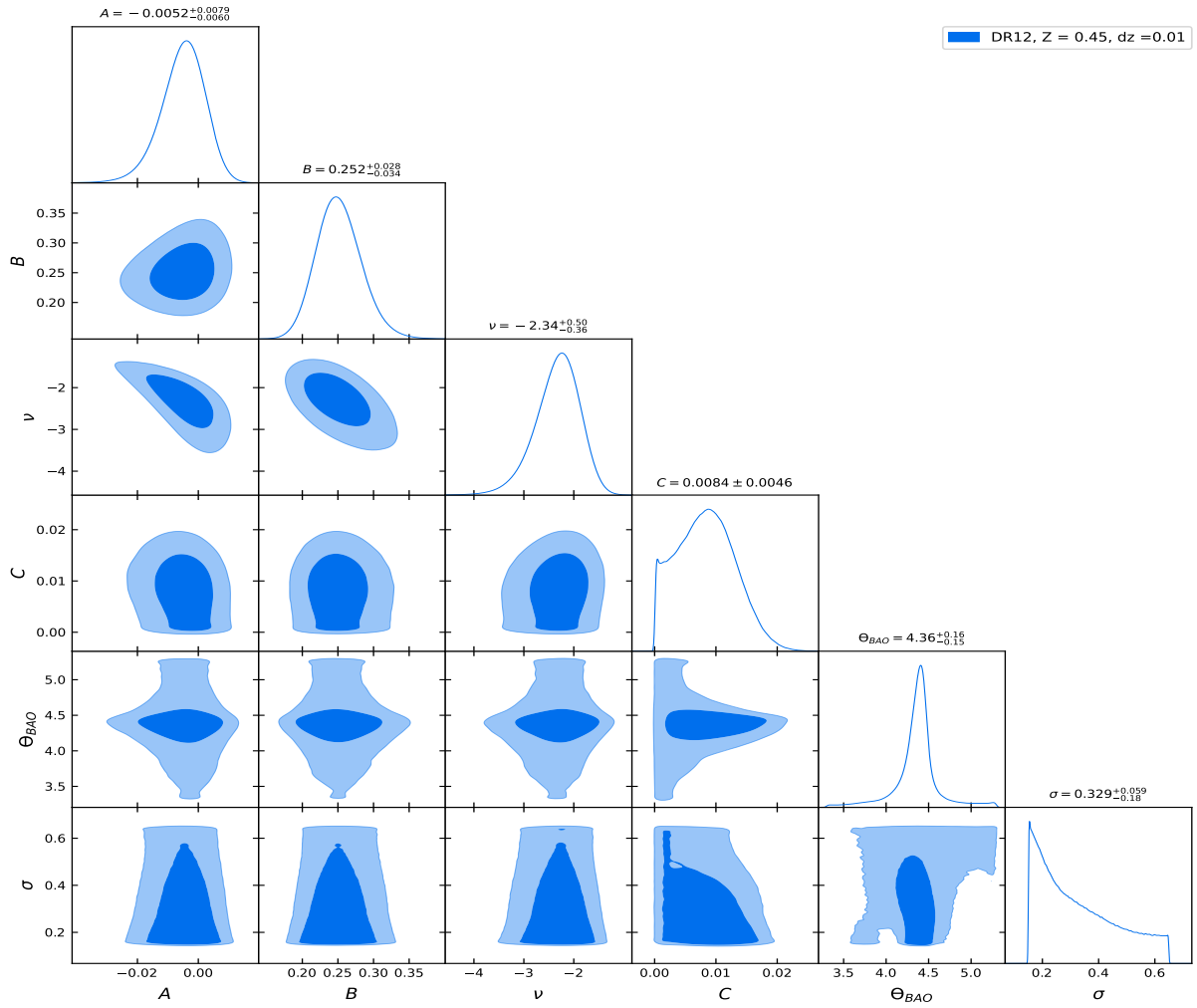
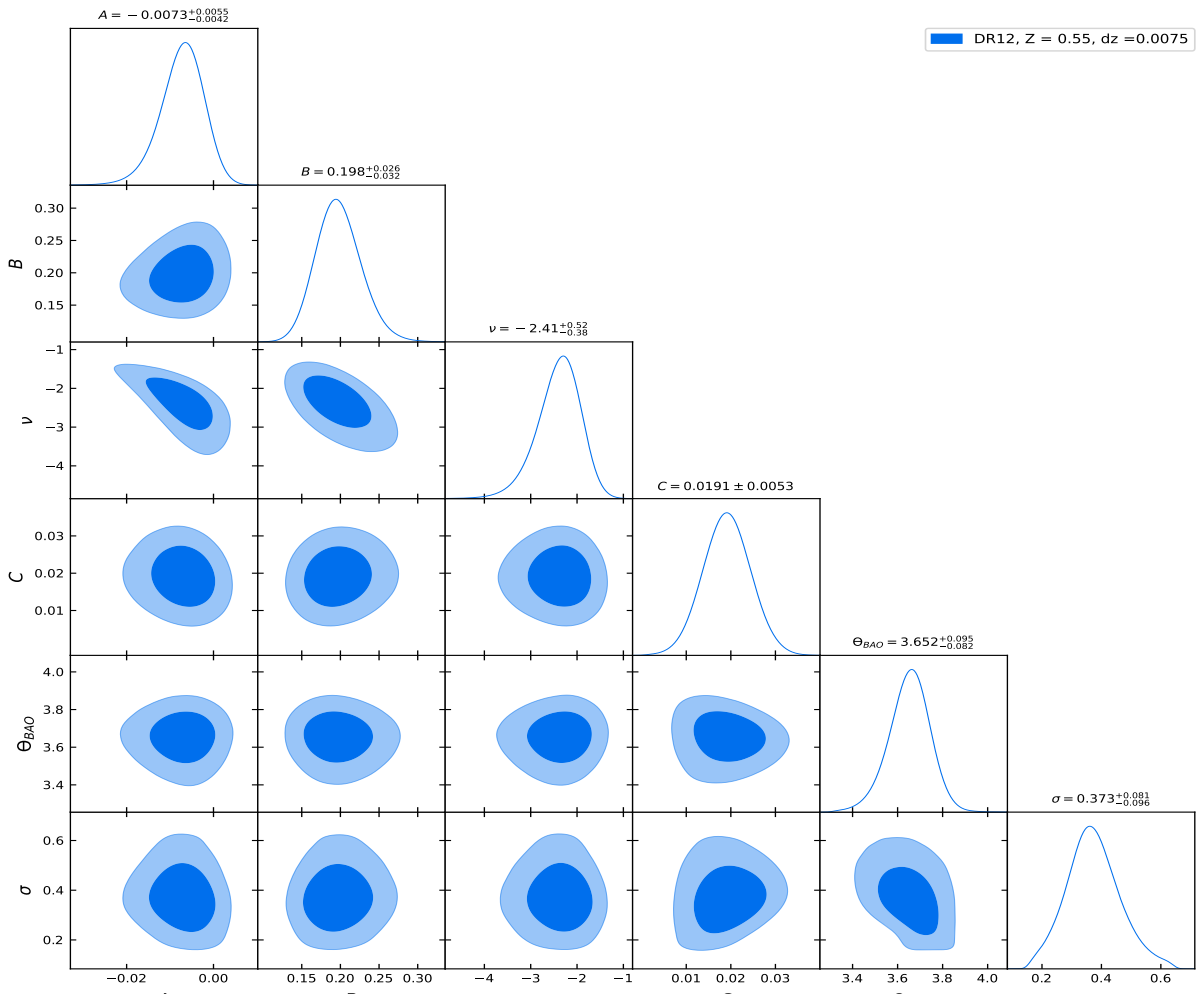
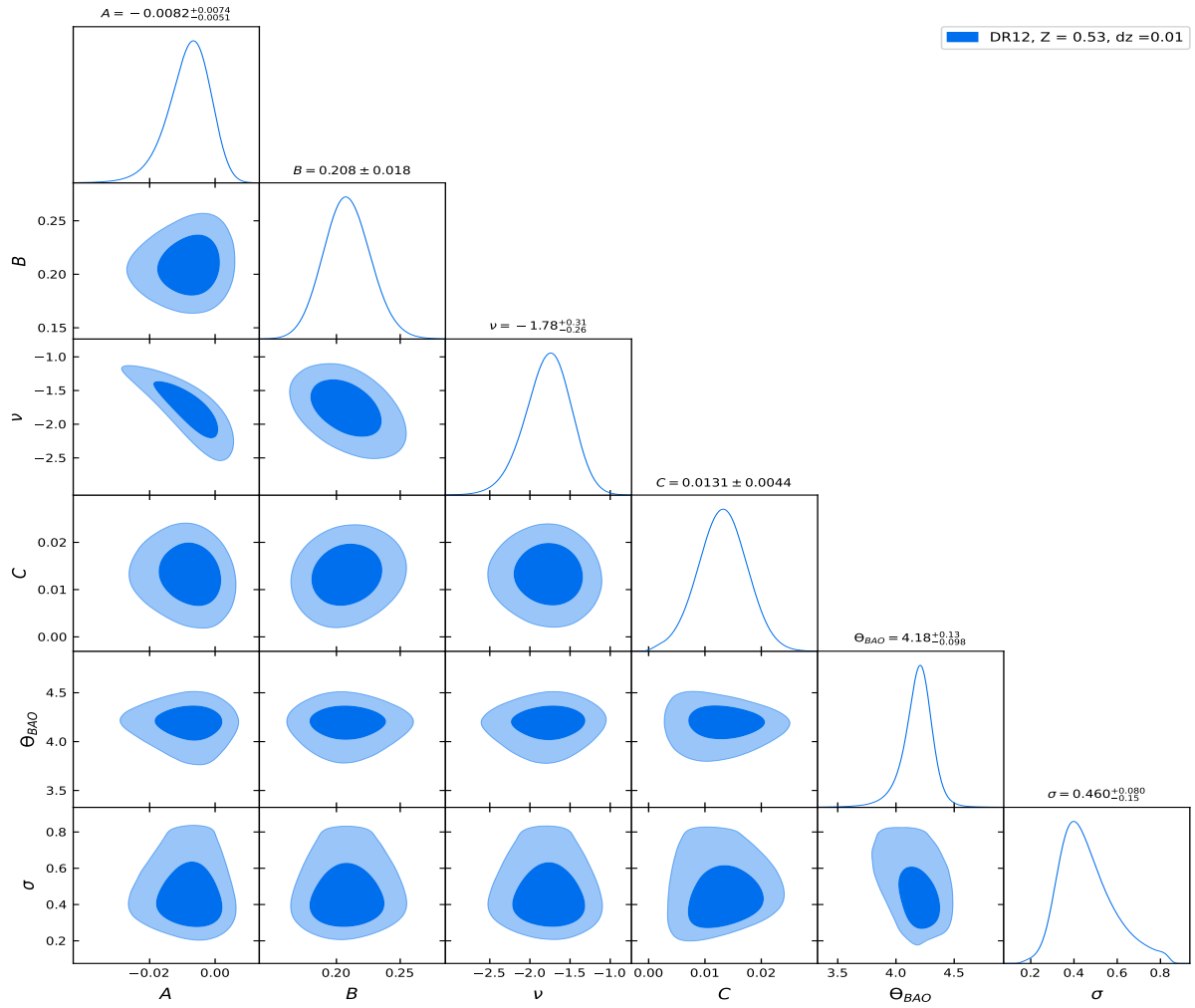
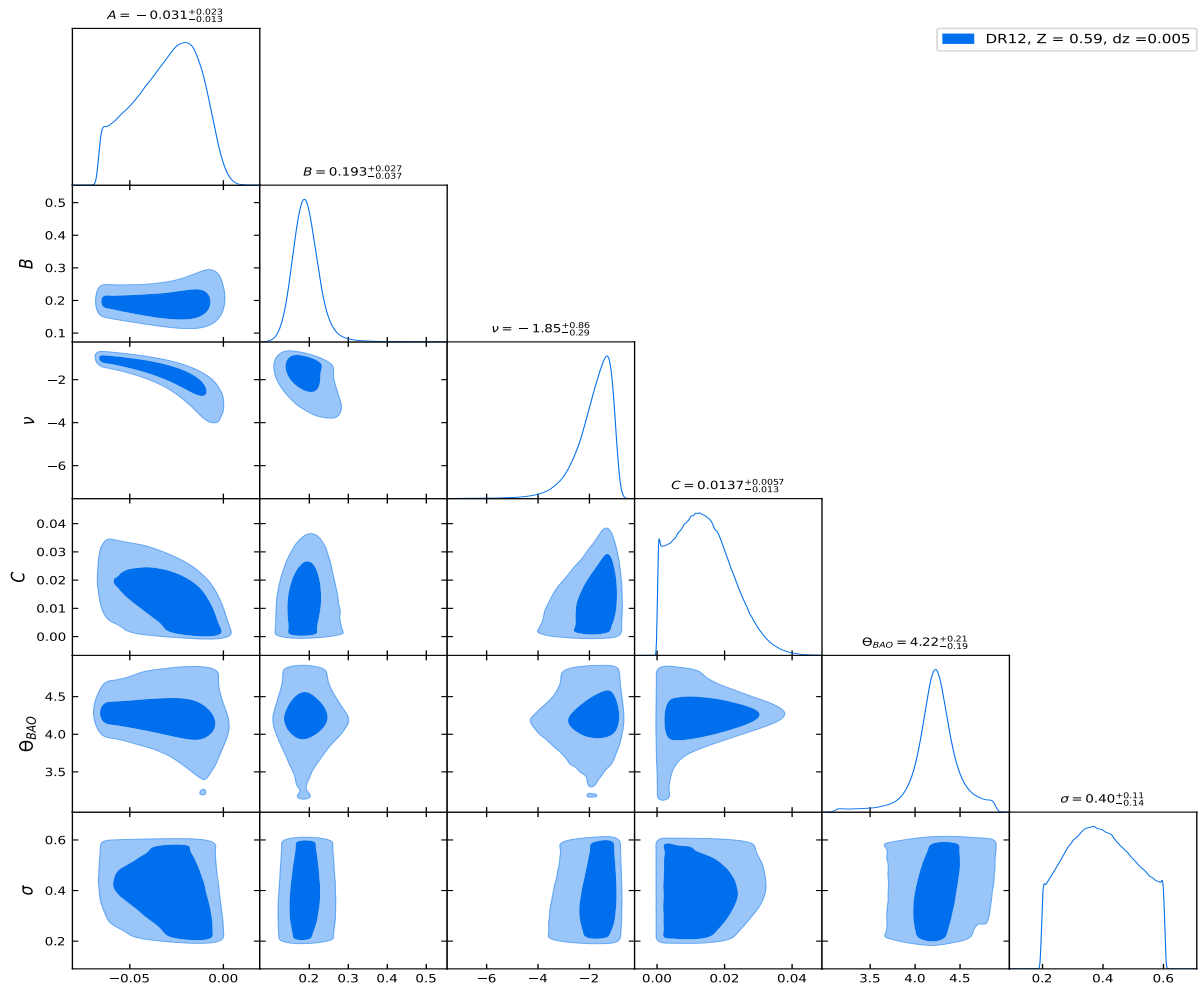
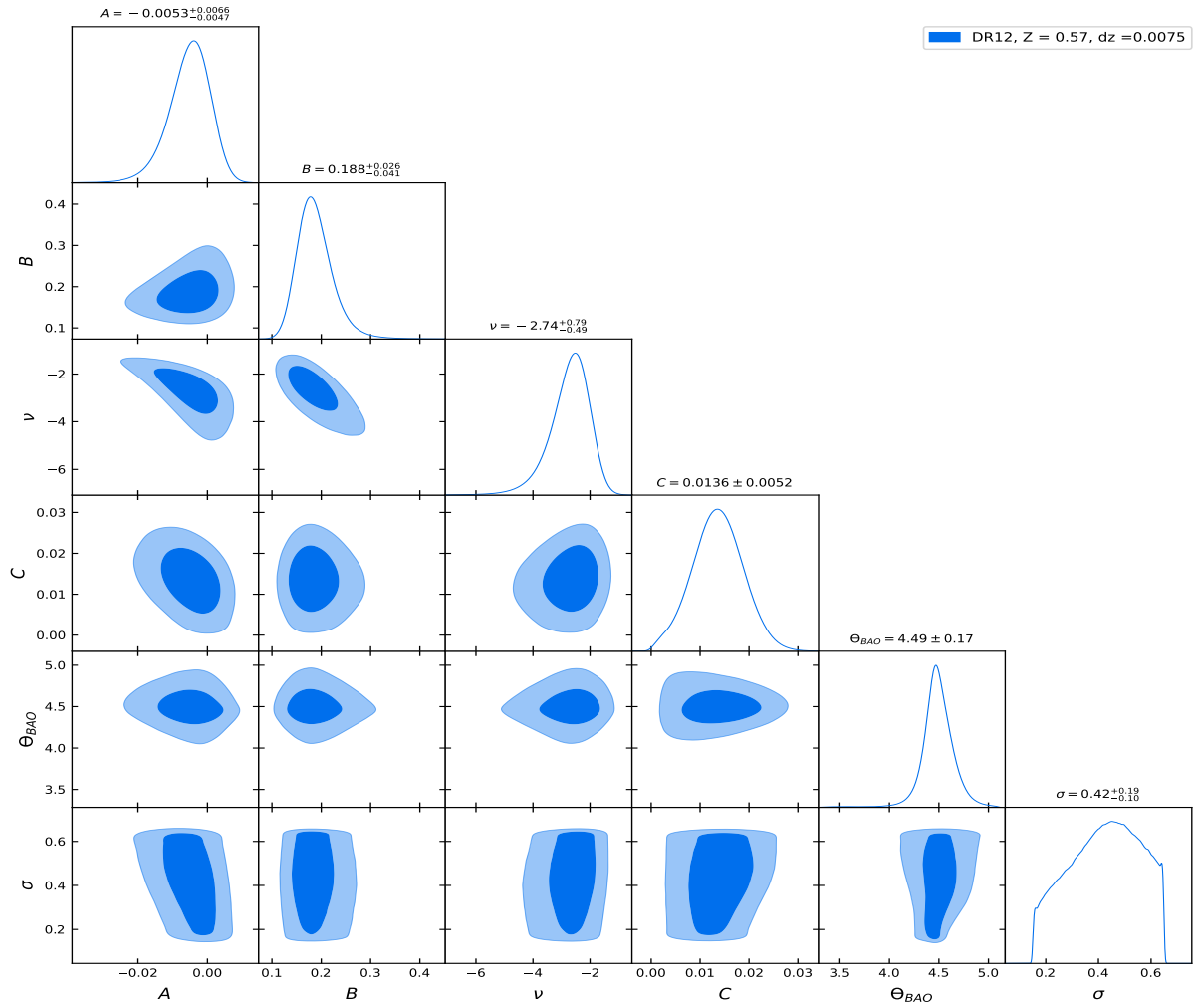


Figure 29 – Best fits from global optimization used as initial point on MCMC.









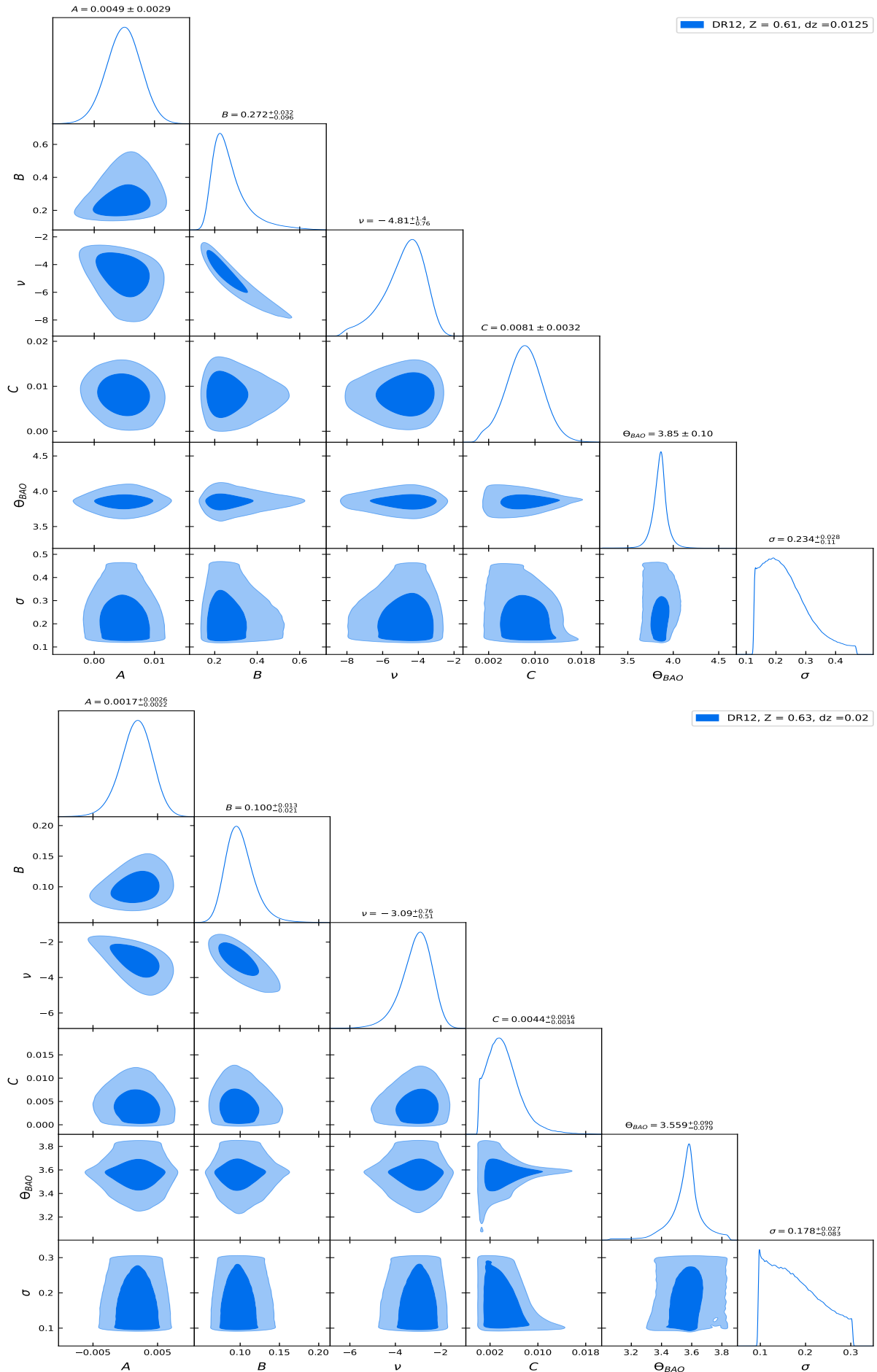


Figure 30 – Distribution on parametric space built with MCMC to all best redshift shells.

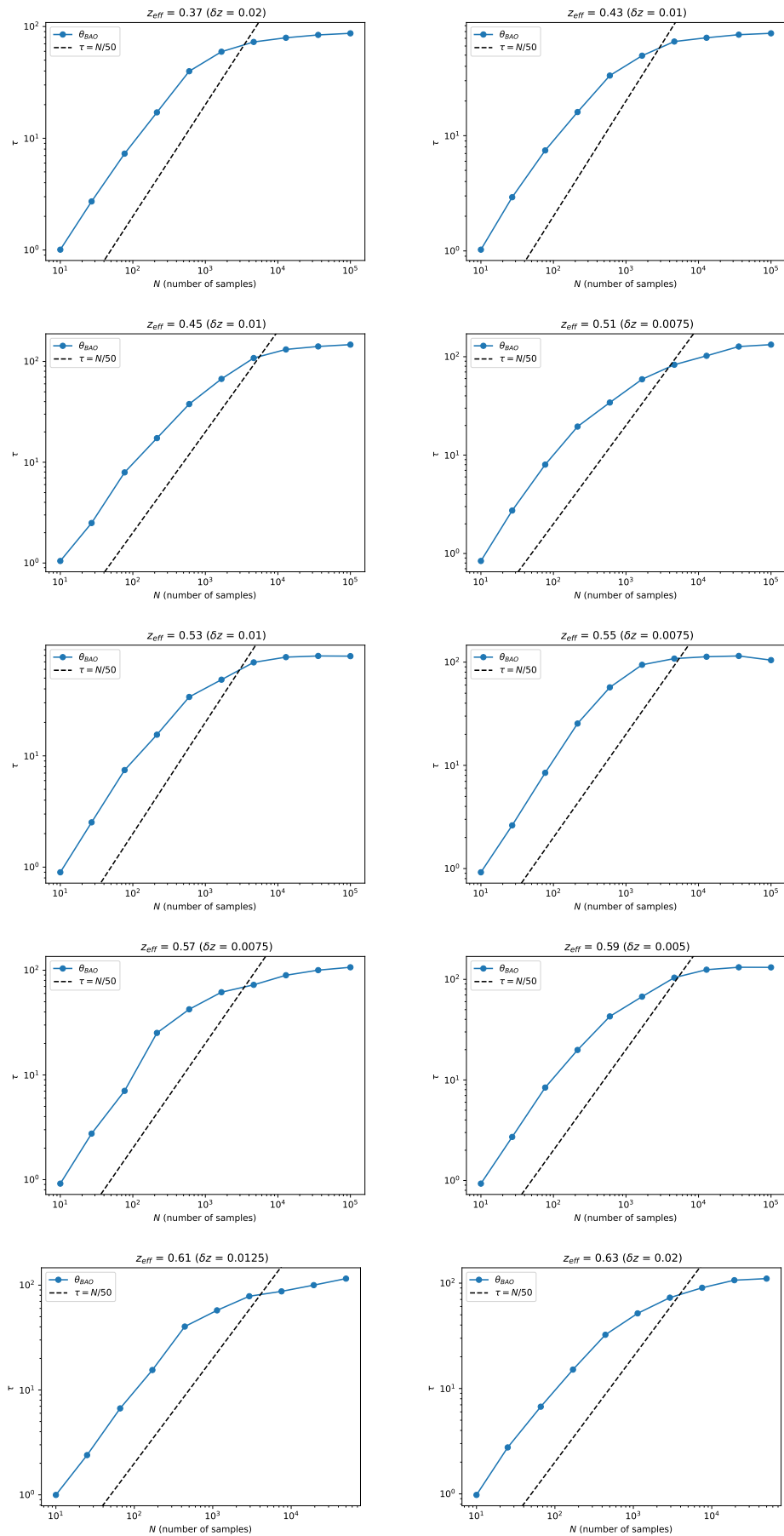


Figure 31 – Plot of autocorrelation time to all best MCMC (shown in the figure 30).

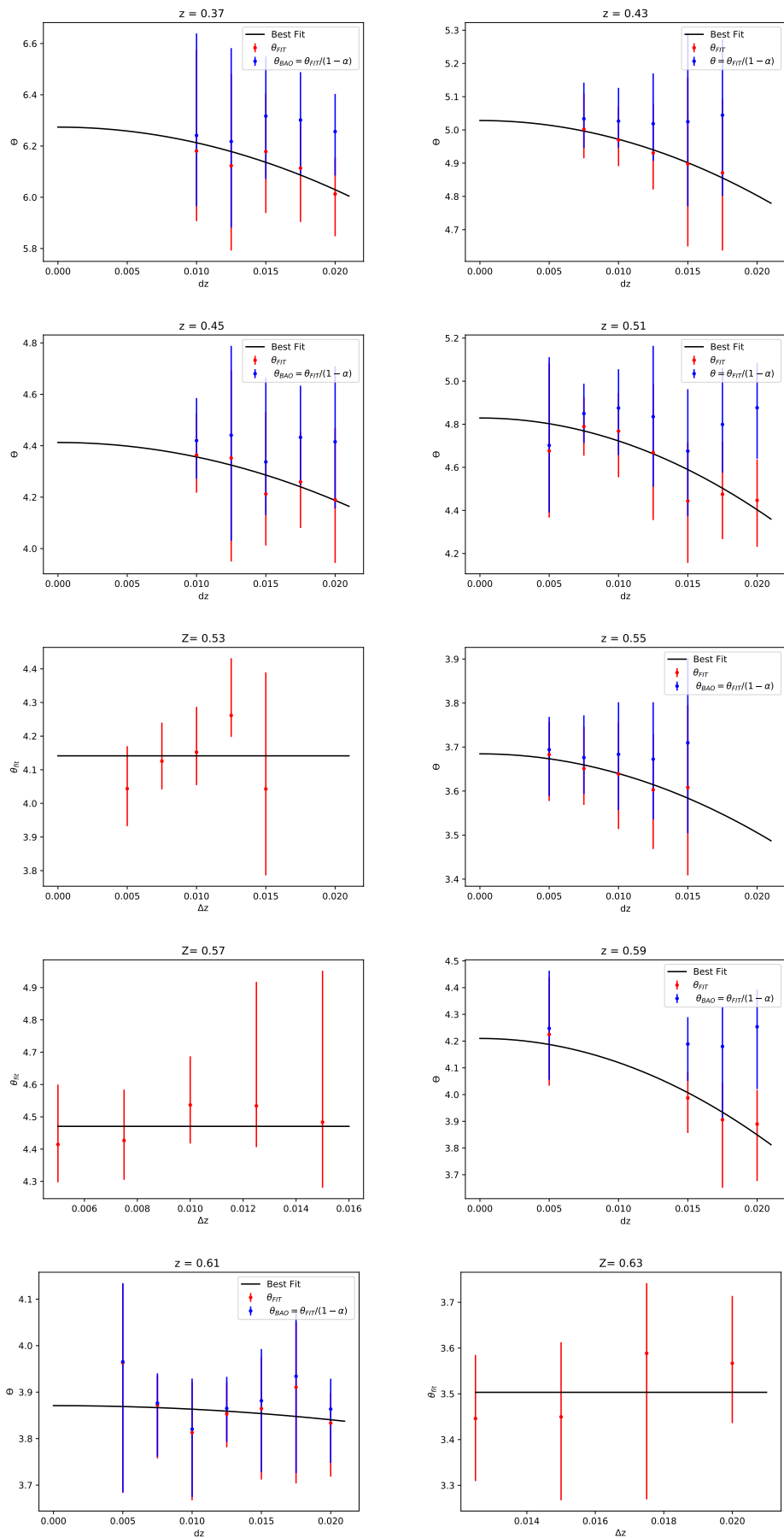


Figure 32 – Displacement of apparent angular BAO scale by radial projections.